博士論文

Band structures and spin polarizations in strongly spin-orbit coupled materials

(強いスピン軌道相互作用を有する物質におけるバンド構造とスピン分極)

坂野　昌人

Contents

Chapter 1

Introduction

The electronic structure of solids governs almost all physical phenomena. An electron possess three degrees of freedom: charge, spin, and orbital. These degrees of freedom result in various electronic structures and physical phenomena through competition and/or cooperation among the degrees of freedom in the solid. Among the three degrees of freedom, the spin and orbital degrees of freedom interplay with each other even in a single-electron problem such as a hydrogen-like atom [1]. This is because spin-orbit interaction, which is derived from Dirac equation in the relativistic quantum mechanics [2–5], universally works around a nucleus. Since the energy of spin-orbit interaction on a peripheral electron can be ~ 1 eV in a heavy atom, the electronic structure and physical phenomena of a lot of materials are mainly governed by spin-orbit interaction; other interactions play a minor role in comparison. In particular, one of the characteristic effects of spin-orbit interaction is that it enables the electronic structure to host a spontaneous spin polarization in momentum space, even in nonmagnetic materials [6, 7]. Recently, such spin-momentum-locked electronic structures were energetically investigated in the context of the rapidly growing field of spintronics, because they can give rise to novel involving electric and magnetic cooperation phenomena.

It superficially seems a competing problem that the spin-orbit interaction mainly working around nuclei can modify band dispersions formed by electrons spreading over the crystal structure. In order to deal with this problem, we should pay attention to the symmetries of wave functions by taking account of the crystal symmetry without prejudice. Looking back into

history, the effect of spin-orbit interaction on band dispersions has been investigated in semiconductors since the 1950s. At that time, researchers used group theoretical analyses [6–11] combined with band calculations during development [12–15] and several state-of-the-art experimental techniques (e.g. electron paramagnetic resonance [16], cyclotron resonance [17] etc.) as research methods. However, it is not appropriate to apply these methods comprehensively for materials with strong spin-orbit interaction, because spin-orbit interaction had been treated as perturbations in early times.

In this thesis, to investigate the electronic structure of strongly spin-orbit coupled materials, we have carried out angle-resolved photoemission spectroscopy (ARPES) measurement and spin-resolved ARPES measurement, which are modern state-of-the-art experimental techniques for directly observing band dispersions and its spin polarization in solids [18–21]. Experimentally observed electronic structures have been compared with the band dispersions obtained through a first-principles calculation based on the density functional theory [22, 23] to discuss the effects of spin-orbit interaction. Thus, in this thesis, we investigate the electronic structure in novel strongly spin-orbit coupled materials by using state-of-the-art experimental and computational techniques combined with the knowledge on the symmetries of wave functions accumulated since the 1950s.

1.1 Spin-orbit interaction

Maxwell's equations suggest that the electric field transforms the magnetic field, and vice versa, in a moving frame. An electron in an atom feels an effective magnetic field because of its own orbital motion, consequently giving rise to the spin-orbit interaction between the spin magnetic moment and the effective magnetic field. Figure 1.1 shows schematics of the semiclassical picture of the spin-orbit interaction in an atom. An electron feels the effective magnetic field generated by the electron's orbital motion around the nucleus in Fig. 1.1(a). In the co-moving frame of the electron in Fig. 1.1(b), the origin of the effective magnetic field is comprehended as a ring current of the orbital motion of the nucleus with positive charges.

In quantum mechanics, the relativistic formalization of the spin-orbit interaction operator

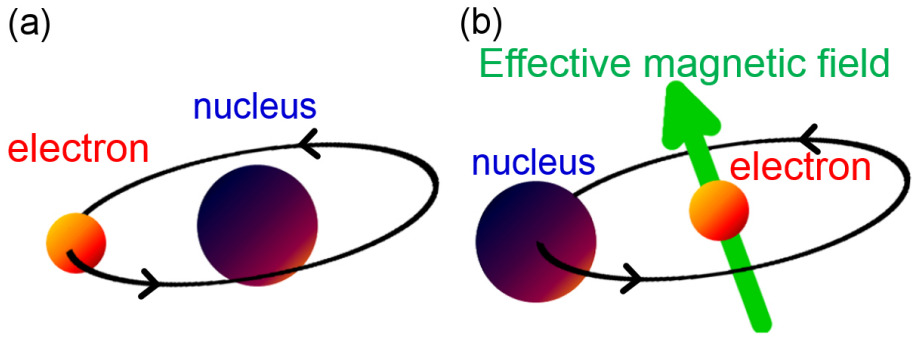

Figure 1.1: Schematics of the semiclassical picture of spin-orbit interaction in an atom. An electron rotating around a nucleus in the rest frame (a) and in the moving electron frame (b). The electron sees the effective magnetic field as represented in (b).

as a correction term for the Schrödinger equation is obtained from the Dirac equation [2] in a static electromagnetic field by using the Foldy-Wouthuysen-Tani transformation [3, 4],

$$H_{\rm SOI} = -\frac{e\hbar}{4m^2c^2}\boldsymbol{\sigma}\cdot[\mathbf{E}\times(\mathbf{p}-\frac{e}{c}\mathbf{A})], \tag{1.1}$$

where e is the elementary charge, $\hbar$ is the Planck constant divided by 2π, m is the mass of an electron, c is the velocity of light, $\boldsymbol{\sigma}$ denotes the Pauli matrices, $\mathbf{E}$ is the static electric field, $\mathbf{p}$ is the momentum of an electron, and $\mathbf{A}$ is the magnetic vector potential. The magnetic vector potential and electric field in the nonmagnetic and central-force-field system are given by

$$\mathbf{A} = 0,\ \mathbf{E} = -\frac{\boldsymbol{r}}{r}\frac{d\phi}{dr}, \tag{1.2}$$

where ϕ is the scalar potential. Then, the spin-orbit interaction operator is represented by

$$H_{\rm SOI} = \frac{e\hbar}{4m^2c^2}\frac{1}{r}\frac{d\phi}{dr}\boldsymbol{\sigma}\cdot\boldsymbol{l}. \tag{1.3}$$

This formulation differs by a factor of 1/2 from that obtained by considering the ring current of the nuclear charge in classical mechanics. By applying a correction for the accelerated frame, the same formulation is obtained even in classical mechanics [1, 5].

We should note that eq. (1.3) represents an operator: hence, the energy of spin-orbit interaction depends not only on the potential but also on the wave functions [24–27]. For example, even

in a heavy atom with a large atomic number, the s-electron does not show spin-orbit coupling, because of the $l = 0$ orbital angular momentum. We also note that the spin-orbit interaction works near the nucleus. Since the non-relativistic wave function near the nucleus behaves $\propto r^l$, the spin-orbit interaction of the p-electron should be stronger than that of the d-electron, if both have same atomic number.

1.2 Band structure with spin-orbit interaction

The spin-orbit interaction modifies valence band dispersions as well as the energies of core levels in solids. The electrons forming valence bands spread over the crystal structure; this behavior seems to contradict the spin-orbit interaction working near the atomic nucleus [24]. To treat the band dispersions with spin-orbit interaction in solids, one of the guidelines was proposed in 1954 by R. J. Elliot [8, 9]. Elliot combined the spin-orbit interaction effect [8, 9] with the group theoretical approach to band dispersions [6, 28], by taking the diamond-type crystal structures (space group $Fd\bar{3}m$) as examples, with the help of band calculation [12, 13, 15]. Figures 1.2(a) and (b) show the schematics of band dispersions with and without spin-orbit interaction in the

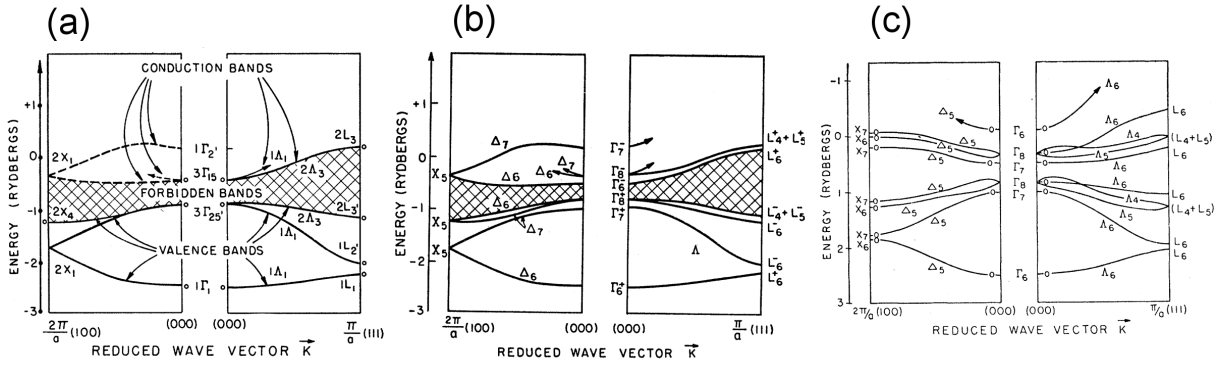

Figure 1.2: (a),(b) Schematics of the band dispersions of diamond with and without spin-orbit interaction, adapted from ref. [8]. The band dispersions without spin-orbit interaction are based on Herman's calculation [13, 14]. (c) A schematic of band dispersion for a zinc-blende type structure modification of boron nitride based on Herman's calculation for diamond [13, 14], adapted from ref. [7]. The spin-orbit splittings are highly exaggerated for the purpose of illustration. The levels marked with 0 have zero slope along that axis.

diamond adapted from ref. [8]. Despite a small contribution compared to the energy scale of the bandwidth, the spin-orbit interaction modifies band dispersions and lifts the band degeneracy around the band gap [e.g., the energy level of the Γ_{15} state in Fig. 1.2(a) splits into two energy levels, Γ_8^- and Γ_6^- states, represented by irreducible representations of the double group [9] in Fig. 1.2(b)]. In 1955, G. Dresselhaus proposed the $\mathbf{k}\cdot\mathbf{p}$ perturbation theory including spin-orbit interaction [6,7] to deal with band dispersions of zinc-blende-type crystal structures (space group $F\bar{4}3m$). The $\mathbf{k}\cdot\mathbf{p}$ Hamiltonian at $\mathbf{k}=\mathbf{k_0}+\mathbf{q}$, given $\mathbf{q}$ is small, including spin-orbit interaction is given by

$$H(\mathbf{k}) = \left[\frac{\mathbf{p}^2}{2m} + V + \frac{\hbar}{4m^2c^2}(\nabla V \times \mathbf{p})\cdot\boldsymbol{\sigma}\right] + \frac{\hbar^2 q^2}{2m} + \frac{\hbar}{m}\mathbf{q}\cdot\mathbf{p} + H_{(1)} + H_{(2)} \tag{1.4}$$

where

$$H_{(1)} = \frac{\hbar^2}{4mc^2}(\nabla V \times \mathbf{q})\cdot\boldsymbol{\sigma},\ H_{(2)} = \frac{\hbar^2}{4mc^2}(\nabla V \times \mathbf{p})\cdot\boldsymbol{\sigma}, \tag{1.5}$$

V is the crystal potential, m is the mass of the electron, c is the velocity of light, $\mathbf{p}$ is the momentum operator, and $\boldsymbol{\sigma}$ denotes Pauli matrices, respectively. Given the solutions at $\mathbf{k_0}$, the first term on the left side of eq. (1.4) represents the unperturbed Hamiltonian as

$$H_0 = \frac{\mathbf{p}^2}{2m} + V + \frac{\hbar}{4m^2c^2}(\nabla V \times \mathbf{p})\cdot\boldsymbol{\sigma} \tag{1.6}$$

In the following terms, the contribution of $H_{(1)}$ to band modification is negligible compared with $H_{(2)}$ because the crystal momentum $\mathbf{q}$ is considered to be much smaller than the actual momentum $\mathbf{p}$. Thus, the perturbation Hamiltonian is given by

$$H' = \frac{\hbar}{m}\mathbf{q}\cdot\mathbf{p} + \frac{\hbar^2}{4mc^2}(\nabla V \times \mathbf{p})\cdot\boldsymbol{\sigma} \tag{1.7}$$

Then, the energy at $\mathbf{k}$ for a nondegenerate level is obtained as

$$E_{\mathbf{k}} = E_{\mathbf{k_0}} + \frac{\hbar^2 q^2}{2m} + \left\langle u_{\mathbf{k}}^n \middle| H' \middle| u_{\mathbf{k}}^n \right\rangle + \frac{\hbar}{m}\sum_{m\neq n}\frac{\langle u_{\mathbf{k}}^n | H' | u_{\mathbf{k}}^m\rangle \langle u_{\mathbf{k}}^m | H' | u_{\mathbf{k}}^n\rangle}{\varepsilon_n - \varepsilon_m} + \cdots, \tag{1.8}$$

where n and m denote the band indices. The group theoretical approach is useful to evaluate those matrix elements. Dresselhaus succeeded in parameterizing the band dispersions in the zinc-blends-type crystal structure byusing several parameters, and provided a schematic of the

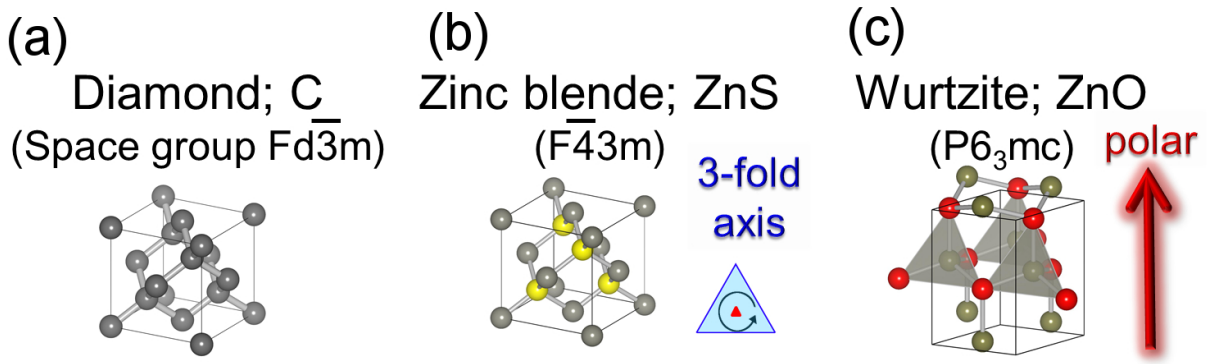

Figure 1.3: (a),(b),(c) Diamond-type, zinc-blende-type and wurtzite-type crystal structures. Zinc-blende-type and wurtzite-type crystal structures lack the inversion symmetry because of the three-fold rotational symmetry and polar structure, respectively.

band dispersions with the help of band calculation, as shown in Figs. 1.2(c) [7, 13, 14]. The $\mathbf{k}\cdot\mathbf{p}$ perturbation theory suggests that the spin-orbit interaction derived from the atomic orbital motion in eq. (1.7) still plays an essential role in the band dispersions in solids.

Let us focus on the difference between the diamond-type and zinc-blende-type crystal structures from the view point of crystal symmetry. The zinc-blende-type crystal structure with a three-fold rotational symmetry axis lacks space inversion symmetry, in contrast to the diamond-type crystal structure, as shown in Figs. 1.3(a) and (b). In the centrosymmetric crystal structure, the Kramers' theorem $E(\mathbf{k},\uparrow) = E(-\mathbf{k},\downarrow)$ and inversion symmetry $E(\mathbf{k},\uparrow) = E(-\mathbf{k},\uparrow)$ require the doubly degenerate band dispersion over the entire Brillouin zone, as represented by

$$E(\mathbf{k},\uparrow) = E(-\mathbf{k},\uparrow). \tag{1.9}$$

In other words, the absence of inversion symmetry allows the lifting of spin degeneracy in momentum space, as discussed in ref. [7] [which does not appear in Fig. 1.2(c)], except for the time-reversal invariant momenta $\mathbf{k} \equiv -\mathbf{k} \,(\mathrm{mod}\, \mathbf{G})$, where $\mathbf{G}$ is the reciprocal vector. The spin-split band dispersions in the noncentrosymmetric crystal structure is also discussed for the wurtzite type crystal structure (space group $P6_3mc$) in Fig. 1.3(c) by E. I. Rashba [10, 11] and R. C. Casella [29, 30]. The wurtzite-type crystal structure has a polar axis along the main axis. Roughly speaking, since the spin-orbit interaction works vertical to the potential gradient, the

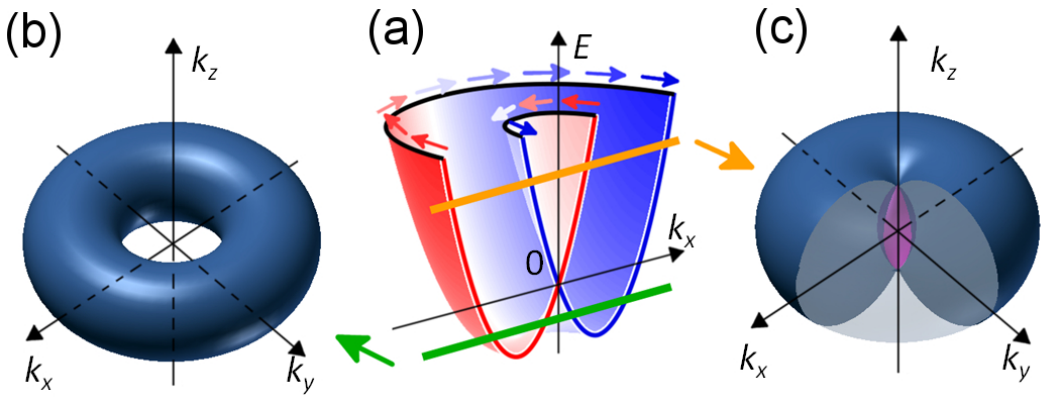

Figure 1.4: (a) Schematic of the spin-split band dispersions at $k_z = 0$ in the wurtzite type crystal structure. (b), (c) Schematics of constant energy surfaces below [green line in (a)] and above [green line in (a)] the band crossing point at $k_x = k_y = 0$.

in-plane spin polarization is obtained in the polar crystal structure. (The microscopic origin of the spin-split band dispersions are discussed in detail in ref. [26, 27]) Figure. 1.4(a) shows a schematic of the spin-split band dispersions at $k_z = 0$, which are characterized by the **k**-linear spin-split bands with the in-plane spin-polarizations [10, 11, 29, 30]. The constant energy surface below (above) the band crossing point at $k_x = k_y = 0$ has the toroidal (double elipses) structure as shown in Fig. 1.4(b) [(c)].

Those symmetry analyses on semiconductors became the basis for the electronics sustaining today's society. However, the effect of the spin-orbit interaction had been omitted in realistic device applications owing to its small energy scale.

1.3 Spin-momentum locked electronic structures

The discovery of the giant magneto resistance effect [31] in 1989 and the proposal of the spin FET transistor [32] in 1990 ushered in a new era of applications utilizing the spin degree of freedom. Consequently, the spin-momentum locked electronic structure such as those of zinc-blende and wurtzite has reattracted attention within the emergent field of spintronics. The main concept of spintronics is the control of magnetization (spin) by an electronic field / current

with the use of the electron's charge and spin coupling. For example, the current of spin angular momentum (called spin current) can be generated by the intrinsic spin Hall effect [33–35] without using magnetic materials, and it can switch the magnetization [36–38]. Since the spin-split band dispersions driven by the spin-orbit interaction in momentum space have the potential to generate spin current universally, the band dispersions in various semiconductors and metals with strong spin-orbit interaction are energetically investigated by using angle-resolved photoemission spectroscopy (ARPES) [18–21], which enables the direct observation of the band dispersions and its spin polarization. Here, we briefly introduce the spin-momentum locked electronic structure of the polar semiconductor BiTeI and a topological insulator.

1.3.1 Rashba-type spin-splitting in polar semiconductor BiTeI

The crystal structure of polar semiconductor BiTeI (space group P3m1) is characterized by the piling up of Te-, Bi-, and I-triangle lattice in order, generating the electric polarization in a unit cell, as shown in Fig. 1.5(a). It gives rise to the huge Rashba-type spin-split conduction bands in bulk and those localized in a surface-confinement potential; they have been observed by ARPES and spin-resolved ARPES [39–44], as shown in Figs. 1.5(b) and (c). Figure. 1.5(d) shows the characteristic Rashba-type band dispersions of the **k**-liner spin-split parabolic band dispersions, as represented by

$$E^{\pm}(\mathbf{k}) = \frac{\hbar^2\mathbf{k}^2}{2m*} \pm \alpha_{\mathrm{R}} |\mathbf{k}| \,, \tag{1.10}$$

where m^* is the effective mass of an electron and α_{R} is the Rashba parameter [10, 11, 45] characterizing the spin-splitting. The Rashba spin-splitting of BiTeI ($\alpha_{\mathrm{R}} = 3.8$ eVÅ [39]) is one or more orders of magnitude greater than those observed in the surface states of Au(111) ($\alpha_{\mathrm{R}} = 0.33$ eVÅ [46,47]), Bi(111) ($\alpha_{\mathrm{R}} = 0.55$ eVÅ [48]), and interface states of InGaAs/InAlAs ($\alpha_{\mathrm{R}} = 0.07$ eVÅ [49]), and it is comparable to the gigantic Rashba-type spin-splitting observed on the surface alloy Bi/Ag(111) ($\alpha_{\mathrm{R}} = 3.05$ eVÅ [50]). Those investigations imply that the huge atomic spin-orbit interaction of the Bi atom (> 1 eV) is not only the necessary condition for the huge **k**-linear band splitting.

M. S. Bahramy, R. Arita, and N. Nagaosa have revealed the origins of the giant Rashba-type spin-split in bulk BiTeI by using the $\mathbf{k}\cdot\mathbf{p}$ perturbation theory including the spin-orbit interaction

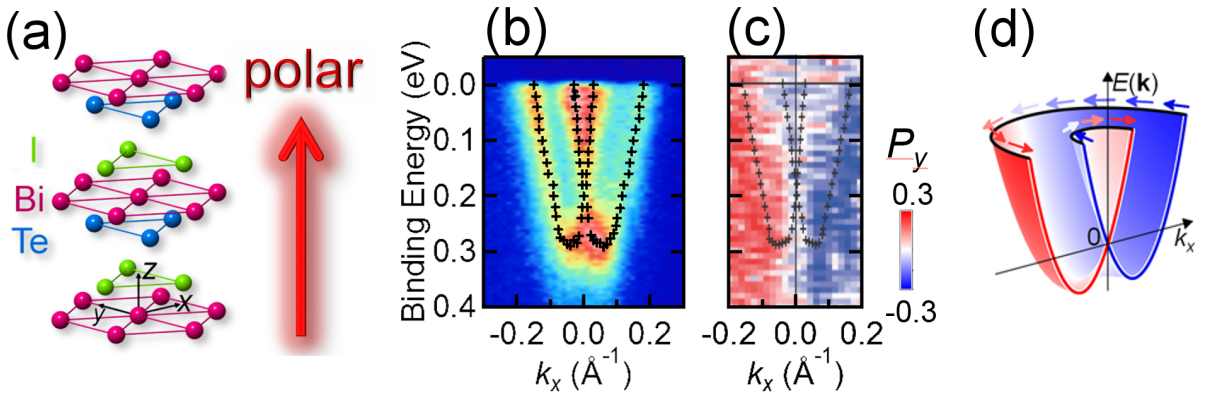

Figure 1.5: (a) Crystal structure of BiTeI. (b) Rashba-type spin-split conduction bands observed by angle-resolved photoemission spectroscopy (ARPES). (c) Spin-resolved ARPES image of the Rashba-type spin-splitting. (d) Schematic of the Rashba-type spin-split band dispersions. All images are adopted from ref. [44]

with the help of a first-principles calculation [51]. The second-order perturbation [as discussed in section 1.2] contributing to the **k**-linear spin-splitting is represented by

$$\Delta\varepsilon_n(\mathbf{k}) = \frac{\hbar}{m}\sum_{m\neq n}\frac{\left\langle u^n_{\mathbf{k}}\left|H_{(2)}\right|u^m_{\mathbf{k}}\right\rangle\left\langle u^m_{\mathbf{k}}\left|\mathbf{q}\cdot\mathbf{p}\right|u^n_{\mathbf{k}}\right\rangle + c.c.}{\varepsilon_n - \varepsilon_m}, \tag{1.11}$$

where *c.c.* stands for complex conjugation. In BiTeI, since the eigenstates across the band gap have the same symmetries owing to the opposing crystal fields between Bi and Te atoms, non-zero matrix elements $\left\langle u^n_{\mathbf{k}}\left|H_{(2)}\right|u^m_{\mathbf{k}}\right\rangle$ are obtained with the help of group theoretical analysis [51]. They proposed three conditions for the huge Rashba-type spin splitting in bulk: (I) the strong atomic spin-orbit interaction, (II) the narrow energy difference between the neighboring states m and n, and (III) the symmetry characters of their corresponding eigenstates. Those factors share a common basis with the early studies on the zinc-blende and wurtzite. Experimentally, the observed spin-splitting in BiTeX (X =I, Br, and Cl) roughly scales with the inverse of the band-gap size in BiTeX [43, 44]. Regarding the application possibility, owing to the Fermi surface with huge spin-splitting in bulk, BiTeI has the potential to generate the highly efficient spin-torque proposed theoretically [52].

1.3.2 Spin-polarized Dirac cone on Z_2 topological insulator

A topological insulator is a nonmagnetic phase theoretically proposed in 2005 by C. L. Kane and E. J. Mele [53–55]. The topological insulator has a band gap in bulk, but a robust metallic state exists at edges for two-dimensional systems or on the surface of three-dimensional system, as schematically shown in Figs. 1.6(b). The difference between a topological insulator and normal insulator is characterized by the Z_2 topological invariant [53,56–58]. Its physical meaning is that there exist an odd number of inverted band structures, which cannot be dissolved by continuous adiabatic deformation, across the Fermi level in the momentum space of the topological insulator, as schematically shown in Figs. 1.6(a) and (b), and they generate an odd number of metallic surface states across the bulk band gap.

Experimentally, a two-dimensional topological insulator has been confirmed in the HgTe quantum-well system by detecting the quantized resistance derived from the edge metallic state in 2007 [59]. Regarding three dimensional systems, an ARPES study on the Bi-Sb alloy system has revealed an odd number of surface states in 2008 [60]. The metallic surface state lying in the bulk band gap is simply described by the cone-like band dispersion called Dirac cone with

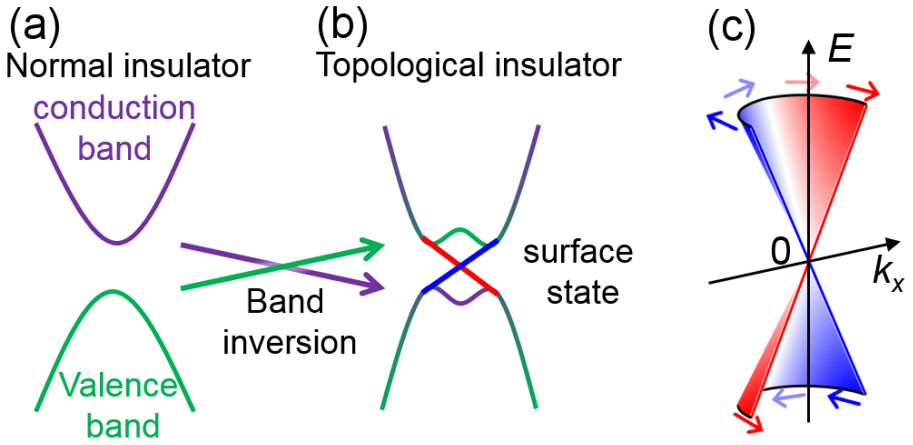

Figure 1.6: (a), (b) Schematics of the electronic structure of normal insulator and topological insulator. In the topological insulator, odd number of the inverted band dispersions exist in momentum space. (c) Metallic surface states with linear dispersions lying in bulk band gap with helical spin-polarization texture.

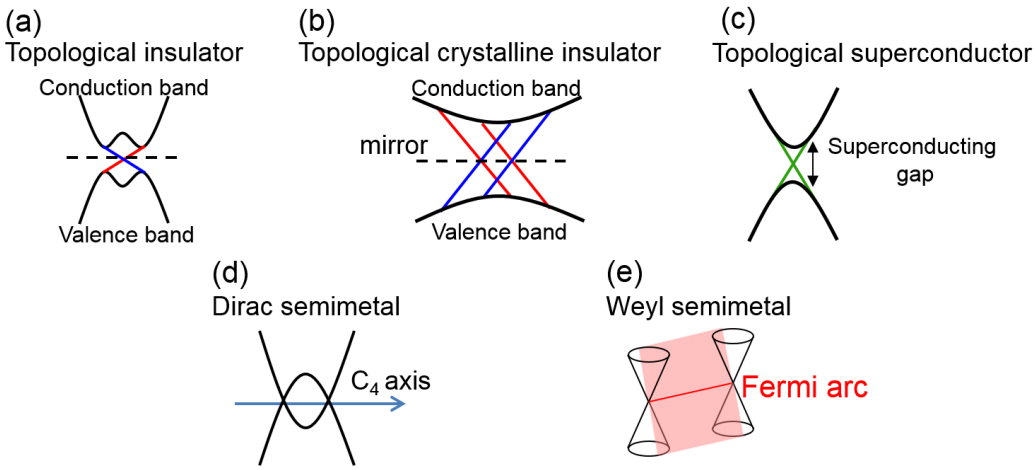

Figure 1.7: Schematics of representative electronic structures of topological materials: topological insulator (a), topological crystalline insulator (b), topological superconductor (c), Dirac semimetal (d) and Weyl semimetal (e). Bulk electronic structures are denoted by black color.

a helical spin-polarization texture as schematically shown in Fig. 1.6(c). In layered materials bismuth chalcogenides Bi_2X_3 (X = Se, Te), an simple Dirac cone as described in Fig. 1.6(c) has been realized [61–65]. Since topological insulators are the nonmagnetic materials, the spin polarization of the surface Dirac cone originates from the spin-orbit interaction. Usually, topological insulators tend to be realized in materials including heavy atoms with strong spin-orbit interaction, because the spin-orbit interaction can play an important role in modifying those band dispersion in bulk from the normal insulator phase into the topological insulator phase (as discussed in Chapter 5).

Starting from the discovery of the topological insulator, topological materials, which are characterized by some kinds of topological invariants, are theoretically and experimentally investigated energetically. Figures 1.7(a)-(e) show schematics of the representative electronic structures of the topological insulator, topological crystalline insulator [66–68], topological superconductor [69–72], Dirac semimetal [73–75], and Wyle semmetal [76–85], respectively. The topological crystalline insulator has an even number of Dirac cones, in contrast to the topological insulator, but they are symmetrically protected by the crystal mirror plane. The topological su-

perconductor has a topological surface state in the superconducting gap, in analogy to the band gap of the topological insulator. The Dirac / Weyl semimetal does not have the energy gap, but it has topological surface states connecting the crossing points of the Dirac-cone-type bulk band dispersions. The Weyl semimetal is realized in the time-reversal symmetry broken system [76,79] or the space inversion symmetry broken system [77, 78, 80–85], and it forms unclosed arc-type surface states with the spin polarization, as shown in Figure 1.7(e).

1.4 Motivation

As discussed in section 1.2, the spin-orbit interaction had been considered as a subsidiary effect on the band dispersions in solids, as it was treated as a perturbation in $\mathbf{k} \cdot \mathbf{p}$ theory. In contrast, the spin-orbit interaction plays an essential role in the band dispersions in recently investigated materials such as BiTeI and topological insulators, attracting much attention because of possible applications and the own characteristic electronic structure. Since the energy of the electron disperses in momentum space owing to the kinetic energy and ligand field, the effect of spin-orbit interaction also depends on them at each $\mathbf{k}$-point. In this thesis, to clarify the effect of the spin-orbit interaction in band dispersions, we experimentally investigate the electronic structure of materials with strong spin-orbit interaction by using angle-resolved spectroscopy (ARPES) and spin-resolved ARPES with the help of a first-principles calculations based on density functional theory [22, 23]. ARPES and spin-resolved ARPES can directly observe the band dispersions and spin polarization in solids. The first-principles calculations can provide information on the Wannier function in comparison with the observed band dispersions. To understand the effect of the spin-orbit interaction, as discussed in the case of BiTeI using the $\mathbf{k} \cdot \mathbf{p}$ theory, we should focus on not only the energy levels at each $\mathbf{k}$-point but also the symmetry of wave function.

This thesis consists of 8 chapters. In Chapter 2, the principles of ARPES and spin-resolved ARPES are explained. In Chapter 3, we present the laser ARPES system developed using commercial nonlinear optical crystals in Ishizaka laboratory, which enables the precise measurement of the band dispersions near the Fermi level. In Chapter $4 \sim 6$, we present ARPES and spin-resolved ARPES studies on materials hosting spin-momentum locked electronic structures.

In Chapter 4, we discuss the electronic structure of 3R-MoS_2, which has a noncentrosymmteric crystal structure due to the three-fold rotational symmetry. We reveal the origin of the observed out-of-plane full spin polarization by focusing on the wave function symmetry of the spin-polarized band dispersions. In Chapter 5, we present a study on the electronic structure of the centrosymmetric superconductor β-$PdBi_2$. Though β-$PdBi_2$ is a metal in the normal state, its topological surface sates with spin polarization are observed to be similar to those of Z_2 topological insulators. The origins of topological surface states are revealed by considering the parity eigenvalues of corresponding eigenstates in analogy to topological insulators. In Chapter 6, we discuss the electronic structure of polar semimetal orthorhombic $MoTe_2$. The unclosed topological surface states similar to those of the Weyl semimetal, which are derived from the combined noncentosymmetric crystal structure and topological electronic structure, are directly observed by laser ARPES measurements. In Chapter 7, we present a general discussion on the effect of the spin-orbit interaction on the band dispersions in solids. Chapter 8 presents a summary of this thesis.

Chapter 2

Experimental methods

In this chapter, we briefly introduce the principle of angle-resolved photoemission spectroscopy (ARPES) measurement and the spin polarimeter used in spin-resolved ARPES measurement. Photoemission spectroscopy is a powerful tool to investigate the electronic structures of solids. The photoemission spectrum of electrons emitted from the solid by the photoelectric effect [86,87] gives much information about the electronic structure of a sample of interest by detecting the electron's kinetic energy, direction of emission, spin polarization, and their dependence on photon energy and polarization. Nowadays, ARPES using vacuum ultraviolet light with a sufficiently narrow line width has achieved great success and become popular as a direct experimental technique to observe the band dispersions in solids, and there are many textbooks [18, 19] and review articles [20, 21] focusing on this technique. In this chapter, we briefly introduce the principle of ARPES measurement and of the spin polarimeter used in spin-resolved ARPES measurement.

2.1 Angle-resolved photoemission spectroscopy (ARPES)

2.1.1 Three-step model and sudden approximation

The photoemission process consists of the photo-excitation process and the transport to and through the sample surface. Though it can be treated as a single coherent process (called the one-step model) as shown in ref. [18], such a treatment is very difficult to handle. Instead, the ARPES measurement is often explained using the three step model, which is suitable for

various realistic situations [21, 88–90]. The three steps consist of 1. photo-excitation process, 2. transport to the sample surface, and 3. escape into vacuum. Here, we briefly explain these processes based on ref. [21].

The first step is described as the optical excitation process between the final state and initial state of N electrons. The translation probability w_{fi} is obtained by the Fermi's golden rule as

$$w_{fi} = \frac{2\pi}{\hbar} \left| \left\langle \Psi_f^N \left| H_{int} \right| \Psi_i^N \right\rangle \right|^2 \delta(E_f^N - E_i^N - h\nu), \tag{2.1}$$

where Ψ_i^N and Ψ_f^N are the initial and final states of the N-particle system, respectively, and E_f^N and E_i^N are the energy of the final and initial states, respectively. The interaction of a photon and an electron is treated as a perturbation given by

$$H_{int} = -\frac{e}{2mc}(\mathbf{A}\cdot\mathbf{p} + \mathbf{p}\cdot\mathbf{A}) = -\frac{e}{mc}\mathbf{A}\cdot\mathbf{p}, \tag{2.2}$$

where $\mathbf{A}$ is the vector potential and $\mathbf{p}$ is the electronic momentum operator. In eq.(2.1), we use the relation $[\mathbf{p}, \mathbf{A}] = -i\hbar\nabla\cdot\mathbf{A}$ and the dipole approximation. To evaluate a photoelectron in eq. (2.1.1), the N-particle final state is treated as

$$\Psi_f^N = A\phi_f^{\mathbf{k}}\Psi_f^{N-1}, \tag{2.3}$$

where A is the antisymmetric operator and $\phi_f^{\mathbf{k}}$ is the single-particle wave function of the final state with momentum $\mathbf{k}$. Its physical meaning is that the $(N-1)$-particle system is not relaxed within the photoemission process (sudden approximation). For the initial state, we assume the Hartree-Fock formalization given by

$$\Psi_i^N = A\phi_i^{\mathbf{k}}\Psi_i^{N-1}. \tag{2.4}$$

Then, we can rewrite the matrix element in eq. (2.1) as

$$\left\langle \Psi_f^N \left| H_{int} \right| \Psi_i^N \right\rangle = \left\langle \phi_f^{\mathbf{k}} \left| H_{int} \right| \phi_i^{\mathbf{k}} \right\rangle \left\langle \Psi_m^{N-1} | \Psi_i^{N-1} \right\rangle, \tag{2.5}$$

where we can define the single-electron dipole matrix element $\left\langle {\phi_f}^{\mathbf{k}} \left| H_{int} \right| \phi_i^{\mathbf{k}} \right\rangle \equiv M_{f,i}^{\mathbf{k}}$, and we sum over all possible excited states m for the total transition probability. As a result, the total photoemission intensity $I(\mathbf{k}, E_{\rm kin}) = \sum_{f,i} w_{f,i}$ measured as a function of $E_{\rm kin}$ and $\mathbf{k}$ is given by

$$I(\mathbf{k}, E_{\rm kin}) \propto \sum_{f,i} \left| M_{f,i}^{\mathbf{k}} \right|^2 \sum_m |c_{m,i}|^2 \, \delta(E_{\rm kin} + E_m^{N-1} - E_i^N - h\nu), \tag{2.6}$$

where $|c_{m,i}|^2 = \left\langle \Psi_m^{N-1} | \Psi_i^{N-1} \right\rangle$ is the probability that removing the electron from the N-electron state i will result in the excited state m of the $(N-1)$-particle system. In the non-interacting system, only one state of m has non-zero $|c_{m,i}|^2$; consequently, the ARPES spectrum as a function of momentum $\mathbf{k}$ will be given by a delta function at the Hartree-Fock orbital energy $E_{\mathrm{B}}^{\mathbf{k}} = -\varepsilon_{\mathbf{k}}$. To treat strongly correlated materials, the Green's-function formalization is useful [21]. Since we treat only weakly correlated materials in this thesis, the formalizations for non-interacting systems describe well the experimental results in the following chapters.

The second step (transport process to the surface surface) is characterized by an effective mean free path of the excited electron. In this process, the inelastic electron scattering generates continuous backgrounds of photoelectrons. The final step (escape process into vacuum) is described by the transmission probability depending on the energy of the excited electron as well as the material work function W.

2.1.2 Energy conservation

The kinetic energy (E_{kin}) of a photoelectron possesses the information of binding energy (E_{B}) in the initial state (corresponding to the Hartree-Fock orbital energy as discussed in the previous section). The energy diagram of photoemission measurement is summarized in Fig. 2.1. The spectral broadenings due to the lifetimes of the initial and the final states, the correlation effect, and the background electrons due to inelastic scattering are omitted for simplicity. Owing to energy conservation, the binding energy E_{B}, which is negative relative to the Fermi level (E_{F}), is given by

$$E_{\mathrm{B}} = h\nu - E_{\mathrm{kin}} - W, \tag{2.7}$$

where W is the work function of material (typically $4 \sim 5$ eV) and $h\nu$ is the incident photon energy. In the actual experiment, the Fermi level (E_{F}) of a sample is usually referred to that of the polycrystalline Au electrically connected to it. As a result, the kinetic energy of a photoelectron relative to $E_{\mathrm{F}} + h\nu - W$ directly gives the binding energy.

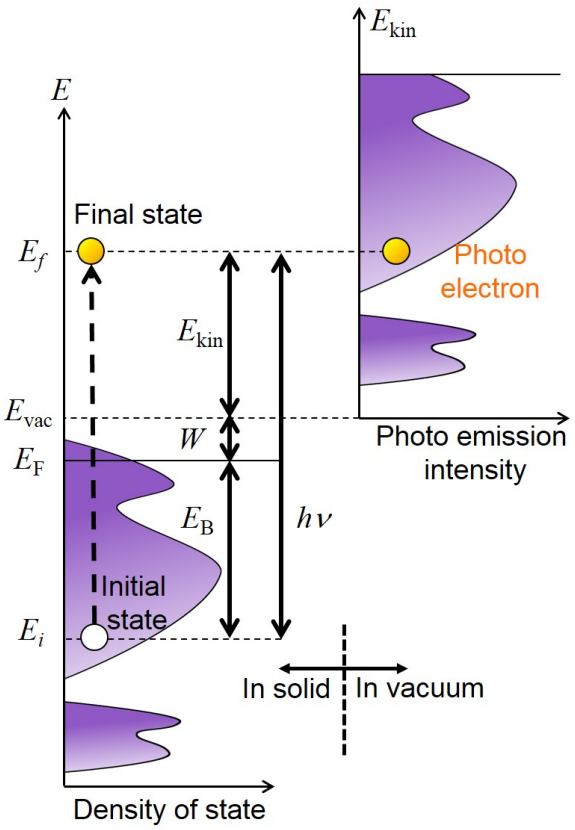

Figure 2.1: The energy-level diagram of a photoemission measurement. E_f and E_i are the energies of the final and initial state of a single electron, respectively; E_{vac} is the vacuum level; E_{F} is the Fermi level; E_{kin} is the kinetic energy of the photoelectron; W is the work function; E_{B} is the binding energy; and $h\nu$ is the photon energy. Here, the spectral broadenings and secondary electrons are omitted for simplicity.

2.1.3 Momentum conservation

The momentum of the photoelectron reflects the crystal momentum of the initial state in solids. As shown in Fig. 2.2, translation symmetry exists along the surface direction; thus, the in-plane component of momentum is conserved within the translation process from solid into vacuum as

$$\hbar K_{||} = \hbar k_{||}, \tag{2.8}$$

where $\hbar K_{||}$ and $\hbar k_{||}$ are the in-plane components of the momentum of the photoelectron and the crystal momentum of the final state, respectively. Usually, the momentum of the incident photon is negligible compared with the momentum of the photoelectron. By detecting the emission angle (θ) and kinetic energy ($E_{\rm kin}$) of the photoelectron, the in-plane component of the crystal momentum of the initial state is given by

$$k_{||} = \frac{\sqrt{2m}}{\hbar}\sqrt{E_{\rm kin}}\sin\theta, \tag{2.9}$$

where m is the mass of the electron. In principle, the two-dimensional electronic structure is identified completely by this equation. On the other hand, the out-of-plane momentum component is not conserved. Then, a parameter V_0 called *inner potential* is used to evaluate the out-of-plane components of the crystal momentum as

$$k_{\perp} = \frac{\sqrt{2m}}{\hbar}\sqrt{(E_{\rm kin})\cos^2\theta + V_0}. \tag{2.10}$$

The physical meaning of this equation is that the final state dispersions are approximated as parabolic free-electrons. V_0 is equal to the energy between the vacuum level and the bottom of the approximated free-electron dispersions. Experimentally, V_0 can be determined by varying the photon energy to fit the observed $k_{\perp}$band dispersions to the known Brillouin zone periodicity. V_0 is typically in the range of $0 \sim 20$ eV.

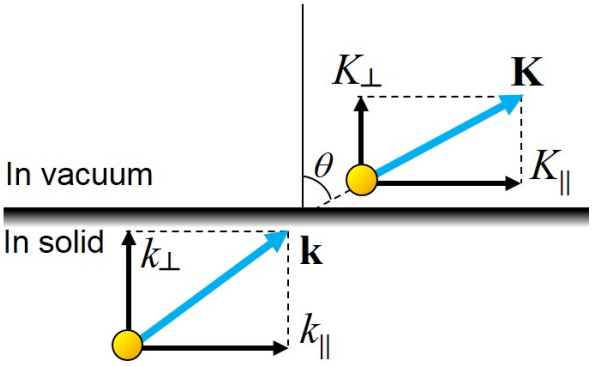

Figure 2.2: Schematic of the in-plane momentum conservation for the electron translation process from solid (lower) into vacuum (upper). **K** and **k** denote the momentum of the photoelectron and the crystal momentum of the final state, respectively.

2.2 Spin-resolved ARPES

2.2.1 VLEED spin polarimeter

Spin-resolved ARPES can detect the photoelectron's spin polarization. For spin-resolved ARPES, two types of spin polarimeters are widely used. The one of them is the Mott-type spin polarimeter [91–99], which utilizes the Mott scattering [100] of a heavy metal target. In Mott scattering, transversely polarized electrons accelerated by a high voltage are scattered by a target with strong spin-orbit coupling, which generates left-right asymmetry of the scattering intensities.

The other is the Very Low Energy Electron Diffraction (VLEED) spin polarimeter [101–107]. In the VLEED detector, the spin-exchange interaction of the electron is utilized to measure the spin polarization [108,109], instead of the spin-orbit interaction in the case of the Mott detector. Figure 2.3 shows a schematic of the spin-dependent electron reflection process of very low energy (a few eV to a few tens of eV) electrons at a magnetized ferromagnetic target. It utilizes the difference of diffraction process depending on the photoelectron's spin being parallel or anti-parallel to the target magnetization. In our study, we performed the spin-polarized ARPES measurements at the beam line BL-9B in the Hiroshima Synchrotron Radiation Center (HSRC) [106, 107] and at the BL19A in photon factory, KEK [103]. Both of them use Fe(001)$p(1\times1)$-O films fabricated on MgO(001) substrate as VLEED targets. A layer of oxygen protects irons

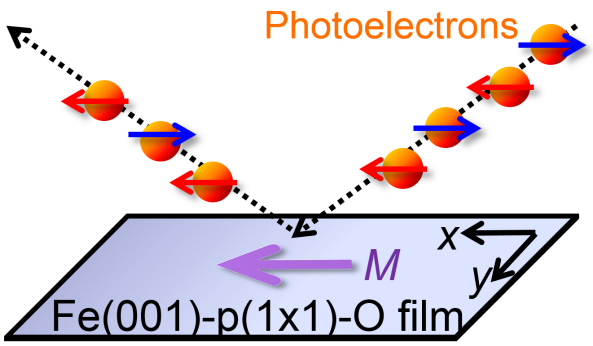

Figure 2.3: Schematic of Very Low Energy Electron Diffraction (VLEED) spin polarimeter utilizing the Fe(001)$p1\times1$-O target. Photoelectrons with spin represented by red and blue arrows are injected into the Fe(001)$p1\times1$-O target with magnetization M and reflected by the target.

from oxidization [103]. Since Fe(001) has a four-fold rotational axis, two directions of spin polarizations can be detected.

2.2.2 Experiment of spin-resolved ARPES

Figures 2.4(a) and (b) show schematics of the spin-resolved ARPES experimental geometry at the Efficient SPin REsolved SpectroScOpy (ESPRESSO) end station attached to the APPLE-II type variable polarization undulator beam line (BL-9B) at the Hiroshima Synchrotron Radiation Center (HSRC) [106, 107] and at BL19A in the photon factory, KEK [103].

The ESPRESSO machine has two VLEED detectors [107], which enable the detection of the three-dimensional spin-polarization components of photoelectrons. The geometry of the experiment is shown in Fig. 2.4(a). Here, x, y, z represent the axes of the sample, whereas X, Y, Z are the coordinate system fixed at the spin detector system. The magnetization of the targets in the two VLEED spin detectors can be selectively aligned along X, Z and Y, Z, respectively by using electric coils. The acquisition of the spin polarization along the sample

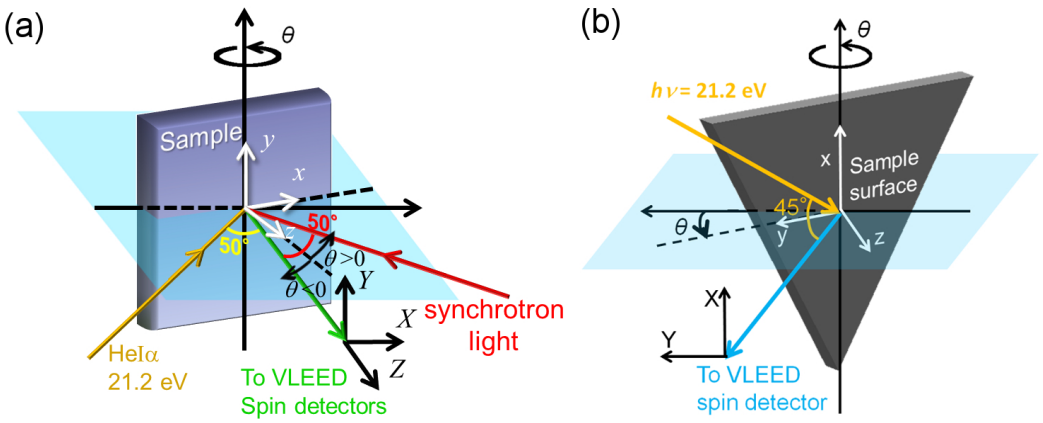

Figure 2.4: (a)Schematic of the experimental geometry of spin- and angle-resolved photoemission spectroscopy at the Efficient SPin REsolved SpectroScOpy (ESPRESSO) end station attached to the APPLE-II type variable polarization undulator beam line (BL-9B) at the Hiroshima Synchrotron Radiation Center (HSRC) [106, 107] using the HeIα light source (21.2 eV), the synchrotron light source and the VLEED spin detectors. (b) Schematic of the spin-resolved ARPES experimental geometry at BL19A in the photon factory, KEK [103].

axes, x, y, z, is enabled through the following procedures.

The spin polarization of the electron at the spin detector (P_X for X-direction), is obtained by

$$P_X = \frac{1}{S_{eff}} \frac{I_X^+ - I_X^-}{I_X^+ + I_X^-}, \tag{2.11}$$

where $S_{eff} = 0.32$ is the effective Sherman function ($S_{eff} = 0.30$ for BL19A in the photon factory, KEK), and I_X^+, I_X^- are the raw spin-resolved ARPES spectra recorded with the target magnetization of plus and minus along the X-direction. P_Y and P_Z are similarly obtained from $I_Y^{+,-}$ and $I_Z^{+,-}$ respectively. The spin-up and spin-down spin-resolved spectra $I_X^{\uparrow,\downarrow}$, $I_Y^{\uparrow,\downarrow}$, $I_Z^{\uparrow,\downarrow}$ are calculated by

$$I_X^{\uparrow,\downarrow} = (1 \pm P_X) \frac{I_X^+ + I_X^-}{2}, \tag{2.12}$$

and so on.

To detect the spin polarization at all **k**-point except the Γ point, we should rotate a sample with the corresponding angle θ in Fig. 2.4. Thus, the spin polarization P_x, P_y, P_z projected along the x, y, z sample crystal axes are related to P_X, P_Y, P_Z by

$$\begin{pmatrix} P_x \\ P_y \\ P_z \end{pmatrix} = \begin{pmatrix} 1 & 0 & 0 \\ 0 & \cos\theta & \sin\theta \\ 0 & -\sin\theta & \cos\theta \end{pmatrix} \begin{pmatrix} P_X \\ P_Y \\ P_Z \end{pmatrix}. \tag{2.13}$$

Using P_x, P_y, P_z, the spin-resolved ARPES spectra for x, y, z are calculated as

$$I_x^{\uparrow,\downarrow} = (1 \pm P_x) \frac{I_{tot}}{2}, \tag{2.14}$$

and so on, where I_{tot} is expressed by $I_{tot} = I_X^+ + I_X^- = I_Y^+ + I_Y^- = I_Z^+ + I_Z^-$. The spin-resolved ARPES spectra for the x-, y-components at BL19A in the photon factory, KEK are obtained in a similar manner. In this thesis, $I_x^{\uparrow,\downarrow}$, $I_y^{\uparrow,\downarrow}$, $I_z^{\uparrow,\downarrow}$ and P_x, P_y, P_z are mainly shown as spin-resolved ARPES results.

Chapter 3

Development of laser ARPES system

3.1 Introduction

Angle-resolved photoemission spectroscopy (ARPES) is a powerful experimental technique to observe band dispersions directly. Especially, a laser light source is very useful for a precise measurement of the electronic structure near the Fermi level [110–114]. In this chapter, we present the laser ARPES system developed in Ishizaka laboratory with commercial nonlinear optical crystals.

3.1.1 Advantages of laser ARPES

A laser light source for the ARPES measurement has several advantages compared with a He discharge lamp ($h\nu$ = 21.2 and 40.8 eV), which is a typical light source used in a laboratory system. The first advantage is its power density. A laser enables a smaller spot size and higher photon flux (typically $\phi \sim 0.1$ mm, $\sim 10^{15}$ photons/s) than those of the He discharge lamp ($\phi \sim 2$ mm, $\sim 10^{13}$ photons/s). This high power density of a laser makes the measurement time short. The second advantage is its high energy and momentum resolutions. The narrow natural linewidth of the laser can provide the ARPES system with an energy resolution better than $\Delta E < 1$ meV [110–113, 115]. In addition, the low energy and directivity of the laser resulted in high momentum resolution. The third advantage is the easy polarization control of photons. Since ARPES is an electron excitation process occurring through photon absorption, as expressed in eq. (2.2), a polarized laser light source can give information about the symmetry

of the initial state [18, 116, 117].

3.1.2 Nonlinear optical crystals

In order to use a laser light source for the ARPES measurement, the photon energy must be greater than the work functions of materials (typically $4 \sim 5$ eV). One of the strategies is to utilize high harmonic generation by using a nonlinear optical crystal.

Figure 3.1 adopted from ref. [112] shows typical nonlinear optical crystals used to generate ultraviolet laser light with the second harmonic generation (SHG) limits, the fifth harmonic generation limits and the absorption edges. The $KBe_2BO_3F_2$ (KBBF) crystal [118, 119] can generate the shortest SHG < 200 nm (> 6.2 eV). Actually, the vacuum ultraviolet laser light generated by the KBBF crystal is utilized for several laser ARPES systems [112–114].

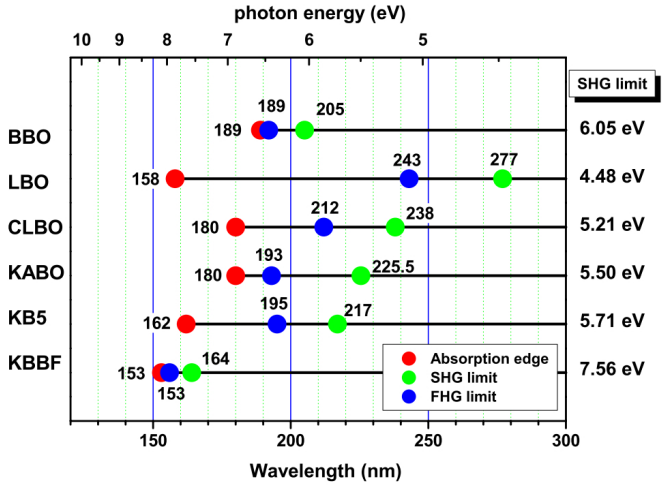

Figure 3.1: A collection of some typical nonlinear optical crystals and their second harmonic generation (SHG) limit, fifth harmonic generation limit, and absorption edge. The $KBe_2BO_3F_2$ (KBBF) crystal shows the shortest SHG wavelength (the highest SHG energy) among all the available nonlinear optical crystals. This graph is adopted from ref. [112].

However, the KBBF crystals are noncommercial. In our study, we use commercial β-BiB_2O_4 (BBO) crystals to obtain the ultraviolet laser light generated by the fourth harmonic generations (FHG: $2\omega + 2\omega$ or $3\omega + \omega$). Because the atmospheric absorption starts from the wavelength

of $\sim$ 190 nm, we choose the wavelength of 193 nm of FHG ($3\omega + \omega$) for the basic setup. At the wavelength of 193 nm, many optical components are commercially available because the ArF-excimer laser generates the same energy.

3.2 Developed optical system

The developed optical system is schematically shown in Fig. 3.2. To obtain the FHG at 193 nm, a mode-locked Ti:sapphire laser (Verdi and Mira, Coherent) is used as the fundamental light source (772 nm). This Ti:sapphire laser has a high repetition rate (73 MHz) and long pulse duration (10 ps) that help to suppress the space charge effect [120, 121], which broadens the photoemission spectra owing to the Coulomb repulsions of emitted electrons. The wavelength tunability of the Ti:sapphire laser (from 660 nm to 1050 nm) is also useful for the ARPES measurements [114]. In the developed optics, two optical passes for the FHGs ($2\omega + 2\omega$ or

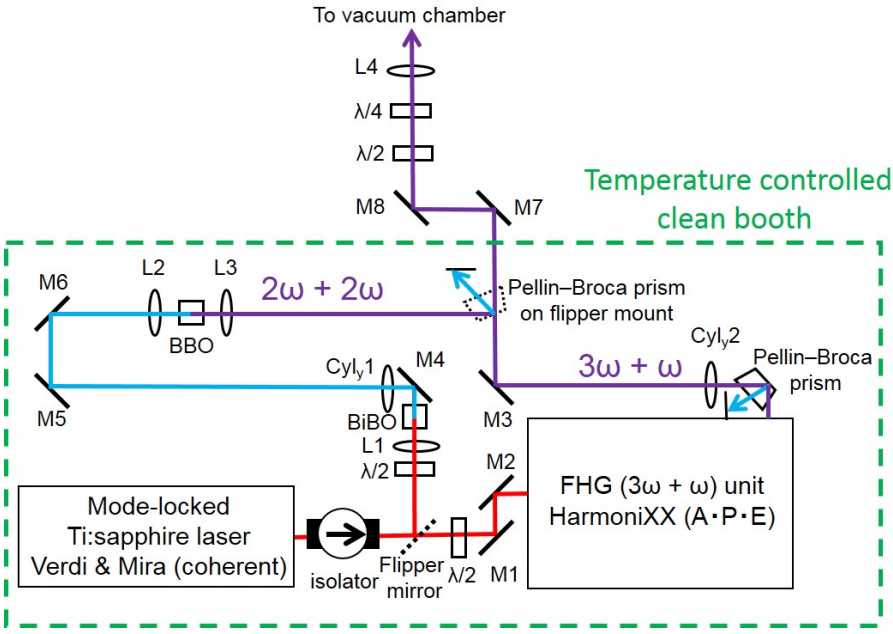

Figure 3.2: Schematic of optical systems. L1: $f = 100$, L2: $f = 100$, L3: $f = 100$, L4: $f = 300$, Cyl(y)1: $f = 80$, Cyl(y)2: $f = 300$. Two optical passes for FHGs ($2\omega + 2\omega$ or $3\omega + \omega$) can be switched by using flipper mounts with a mirror and a Pellin-Broca prism.

$3\omega + \omega$) can be easily switched by using flipper mounts with a mirror and a Pellin-Broca prism, as the situation demands. For the $2\omega + 2\omega$ FHG, the second harmonic light is generated by a BiB_3O_6 (BiBO) crystal with high durability. Fourth harmonic light of $\sim$ 10 mW at 210 nm is obtained using the BBO crystal with the input of fundamental light (840 nm) of 3.0 W [122]. For the $3\omega + \omega$ FHG, fourth harmonic light of $\sim$ 0.2 mW at 193 nm is obtained by using a commercial FHG unit (HarmoniXX, A·P·E) with the input of 3.0 W at 772 nm. This optical system is in a clean booth with a temperature stabilized at $T = 24.5 \pm 0.1$°C.

The FHG laser light enters the vacuum chamber with an incident angle 45 degree as schematically shown in Fig. 3.3(a). To measure the laser spot size just on a sample position, we performed the knife-edge measurement utilizing a copper block edge as schematically shown in Fig. 3.3(b).

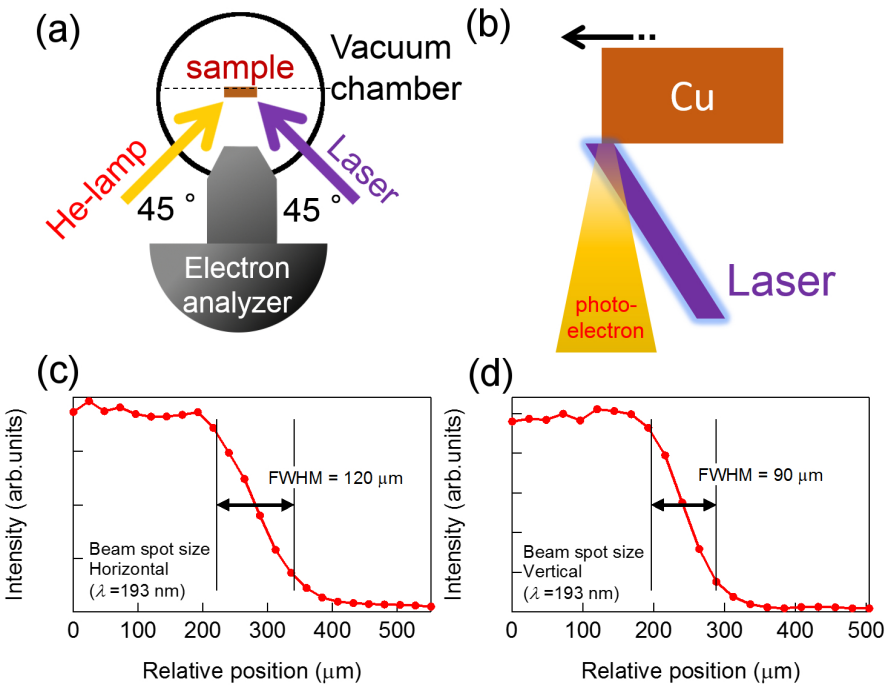

Figure 3.3: (a) Schematic topview geometry of the ARPES system developed in Ishizaka laboratory. (b) Schematic of the knife-edge measurement for the laser spot size just on a measurement sample position in vacuum. (c), (d) Results of the laser spot-size measurements (photoelectron intesity vs. sample relative position) for the horizontal and vertical direction, respectively.

The spot size is evaluated to be 0.12 mm (horizontal) × 0.09 mm (vertical) as shown in Figs. 3.3(c) and (d) at the measurement position in vacuum, respectively. The theoretical limit of the smallest beam (r) is estimated by

$$r \approx \frac{M^2 f \lambda}{\pi r_0} \tag{3.1}$$

where M^2 is the beam quality factor, f is the focal length of the lens, λ is the wave length and r_0 is the radii of incident light. The diameter limit is ~ 0.08 mm estimated by the current setup ($r_0 = 1$ mm, $M^2 \sim 1.1$ and $f = 300$ mm). The achieved value (vertical direction: 0.09 mm) has room for improvement.

3.3 Optimization of angle-resolved mode of electron analyzer

In addition to preparing the laser light source, fine optimization of electron lenses in the electron analyzer is required for the laser-ARPES measurements because the emitted photoelectrons with a low kinetic energy are easily affected by the inaccurate electric fields [123].

Here, we made a angular device [a photograph is shown in Fig. 3.4(a)] to optimize four

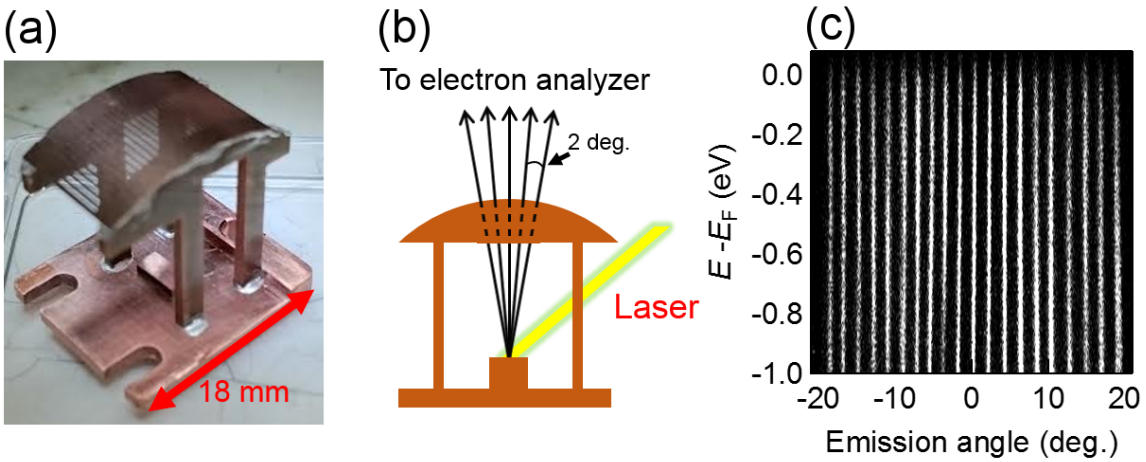

Figure 3.4: (a) Photograph of the homemade angular device. (b) Schematic of the photoelectrons emitted from the angular device. (c) Obtained ARPES image of the angular device after the optimization of the electron lenses.

lens parameters in the electron analyzer (VG Scienta, R4000). As schematically shown in Fig. 3.4(b), the emitted photoelectrons should be observed at intervals of 2 degrees, regardless of the photon energy. After the optimization, the ARPES image of parallel photoelectron signals at intervals of 2 degrees is obtained [Fig. 3.4(c)]. Though the electron analyzer is fine tuned, we should still pay attention to the fact that the emitted photoelectron is easily effected by the environment around the sample (e.g., work function difference between a sample and a sample mounting, sample shape, etc.) [123, 124].

3.4 Evaluation of energy and momentum resolution

To evaluate the energy resolution of the developed laser ARPES system, we carried out angle-integrated photoemission measurement on the Au polycrystal at the lowest temperature ($T = 7.4$ K in the current setup). Figure 3.5 shows the Fermi-edge spectrum of Au taken at $T = 7.4$ K. The fitting function is the Fermi-Dirac distribution function convolved by the Gaussian of FWHM = 0.6 meV. Taking account of the temperature error of the sample, we conclude that a total energy resolution of < 0.9 meV is achieved.

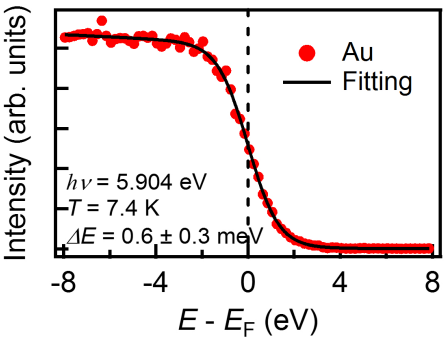

Figure 3.5: Angle-integrated photoemission spectrum of Au at $T = 7.4$ K together with the Fermi-Dirac distribution function convolved by a Gaussian with FWHM of 0.6 meV.

The designed energy resolution ΔE of the hemispherical electron analyzer is given by

$$\Delta E = \frac{wE_0}{2R} \tag{3.2}$$

where w is the slit size, E_0 is the pass energy and R is the radius of electron pass in the analyzer.

The expected value of energy resolution of the current setup with $w = 0.2$ mm, $E_0 = 1$ eV, and laser light linewidth of 0.34 meV [122] at $\lambda = 210$ nm ($h\nu = 5.90$ eV) is $\Delta E = 0.60$ meV. The fitting function of Gaussian width of 0.6 meV in Fig. 3.5 is in good agreement with the expected energy resolution. Since $k_{\mathrm{B}}T$ at $T = 7.4$ meV is 0.64 meV, which is comparable to the evaluated energy resolution, a lower-temperature setup is required to evaluate the energy resolution precisely.

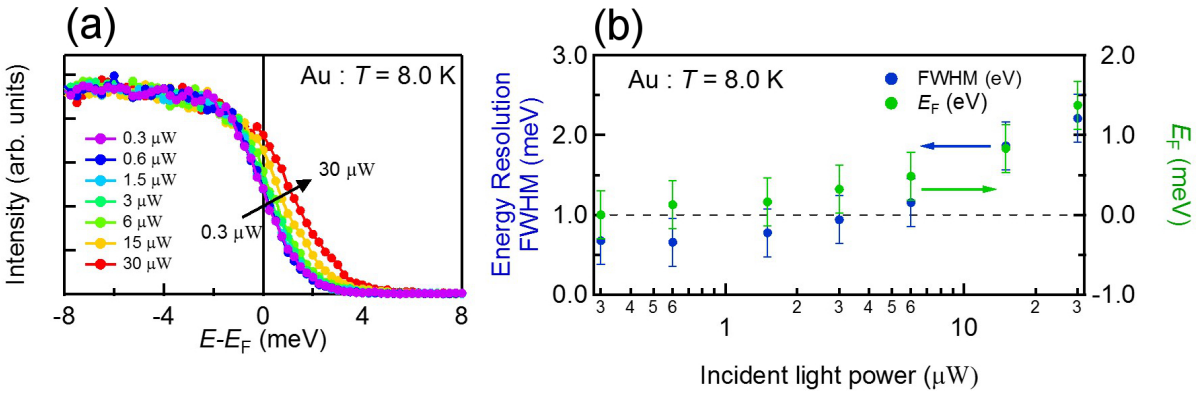

Figure 3.6: (a) Dependence of Fermi-edge spectra of Au polycrystal at $T = 8.0$ K on the incident laser light power. (b) Dependence of the energy resolution (blue) and Fermi-edge position (green) on the incident laser power relative to that taken with 0.3 μW. Incident light power of 30 μW is the limit of the fluorescent screen in the photoelectron analyzer.

To check the suppression of space charge effect [120, 121], the dependence of the Fermi-edge spectra of Au polycrystal at $T = 8.0$ K on the incident laser light power is shown in Fig. 3.8(a). Here, the Fermi level is defined by the Fermi-edge position with the incident power of 0.3 μW. The spectra is fitted by the Fermi-Dirac distribution function at $T = 8.0$ K convolved by a Gaussian of FWHM as a free parameter. On increasing the incident light power, the Fermi edge shifts to higher energies and broadens owing to the Coulomb repulsion of photoelectrons [120, 121], as shown in Fig. 3.8(b). The incident power of 30 μW is the limit of the fluorescent screen in the photoelectron detector. The space charge effect is confirmed to be suppressed well (energy resolution < 1 meV) for the range of usual operation (incident light power < 3 μW).

The upper limit of momentum resolution is evaluated by the spectrum of orthorhombic

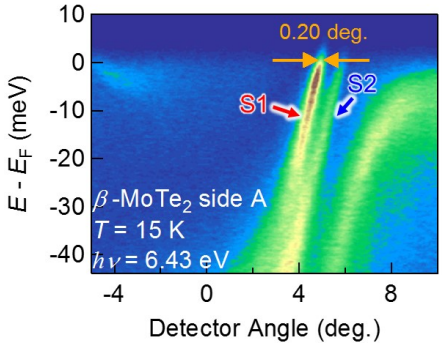

Figure 3.7: Laser ARPES image of β-$MoTe_2$ (as discussed in Chapter 6) at $T = 15$ K with the photon energy of $h\nu = 6.43$ eV. The spectrum width of the S1 surface band is evaluated to be 0.2 degree along the momentum direction.

$MoTe_2$ (as discussed in Chapter 6) at $T = 15$ K as shown in Fig, 3.8. The spectrum width of sharp intensity of the S1 surface state (denoted by red arrow) along the momentum direction is 0.2 degree at the Fermi level fitted by the Gauss function. Since the lifetime of this band dispersion is not taken into account, it gives the upper limit of momentum resolution. The measured upper limit value of 0.2 deg is comparable to the catalog spec of 0.1 deg (VG Scienta, R4000).

3.5 Measurement examples

In this section, we present examples of ARPES images obtained by using the developed laser-ARPES system.

3.5.1 Polar semiconductor BiTeBr

BiTeBr is a polar semiconductor in which the Rashba-type spin-split bands in bulk have been realized [43]. On surface, the ladders of two-dimensional Rashba-type spin-split conduction bands confined in the surface potential have been observed in a previous laser-ARPES study [43].

Here, we show the ARPES image of BiTeBr obtained by using the laser-ARPES system developed in Ishizaka laboratory in Fig. 3.8(a). The ladders of Rashba-type spin-split conduction bands are clearly observed. They are in good agreement with the calculation result obtained

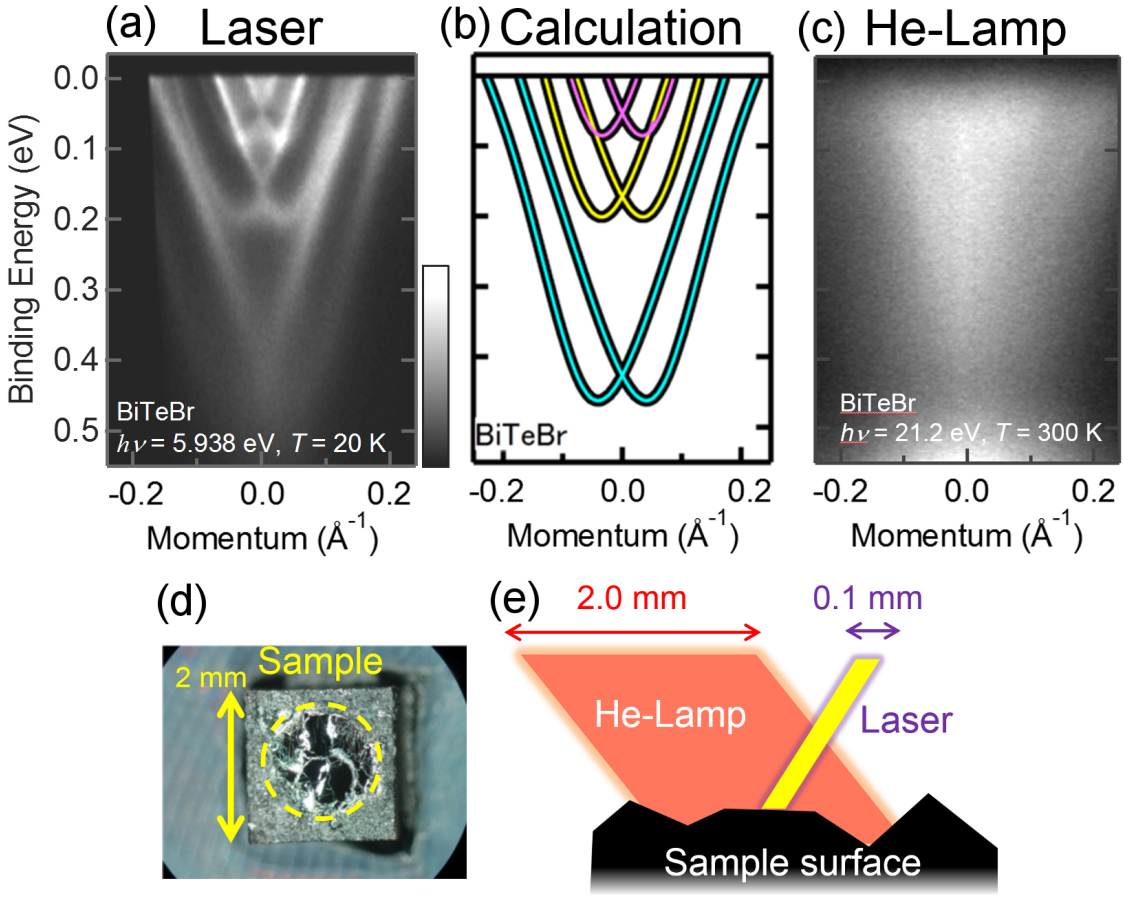

Figure 3.8: (a) Laser-ARPES image of polar semiconductor BiTeBr. The ladders of Rashba-type spin-split bands confined in the surface potential are clearly observed. (b) Calculated subband structures obtained by the Poisson-Schrödinger method [43]. (c) ARPES image of BiTeBr obtained using a He discharge lamp. (d) A photograph of the measurement sample. (e) Schematic of the rough surface of BiTeBr and a comparison between the spot sizes of the incident laser (~ 0.1 mm) and He discharge lamp (~ 2.0 mm).

using the Poisson-Schrödinger method [43], as shown in Fig. 3.8(b). On the other hand, with the use of a He discharge lamp, the ARPES cannot detect such a ladder of spin-split bands, as shown in Fig. 3.8(c),

The most important reason why the clear image is obtained only when using the laser light source is the spot size of incident light. A photograph of the sample after ARPES measurement

is shown in Fig. 3.8(d). It indicates that the cleavage surface is rough and the scale size of the flat part is about 0.3 mm, as schematically shown in Fig. 3.8(e). The smaller spot size ($\sim$ 0.1 mm) of laser ARPES is superior for investigating materials with such a rough surface or small sample in comparison with the He discharge lamp.

3.5.2 Iron-based superconductor FeSe

FeSe is an iron-based superconductor. It shows structural and superconducting transitions at $T_S \simeq 90$ K and $T_c \simeq 9$ K, respectively, without any magnetic order [125]. Recent ARPES studies have reported a lifting of degeneracy in d_{zx}/d_{yz} orbitals at the Γ and M point, which appear at low temperature [126–129]. Polarization-dependent ARPES utilizing the polarization of incident laser light enables us to determine the symmetry of the wave function of the initial state [18, 130], taking account of the measurement geometry and the mirror plane of the crystal structure. In our study, we reveal the sign change of orbital polarization between the Γ and M

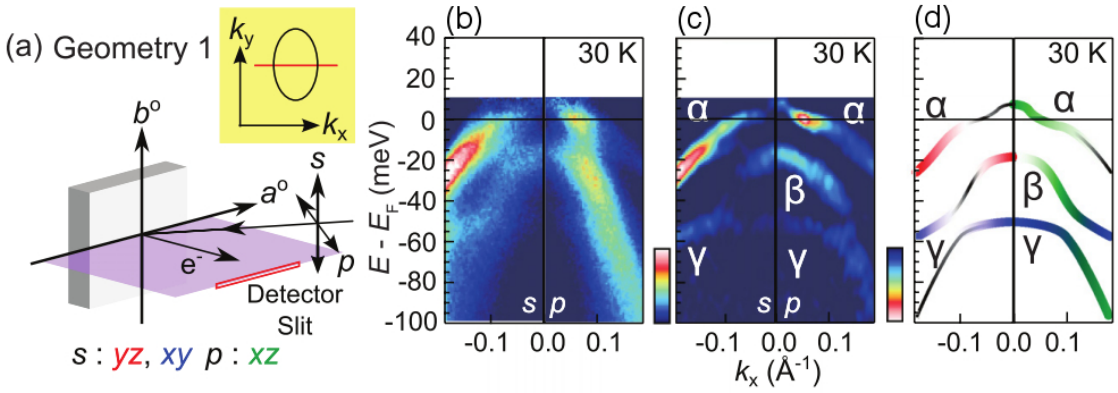

Figure 3.9: (a) Experimental geometry for polarization-dependent laser ARPES. The purple plane represents a mirror plane of the orthorhombic lattice. Observable orbital characters are also shown for each polarization. (b), (c) E-k image divided by the Fermi-Dirac distribution function and its second E derivative detected in Geometry 1 at 30 K, respectively. The left (right) panels are E-k images obtained by s (p) polarization. (e) Schematic band dispersions and their orbital characters. Band dispersions colored in green, red, and blue are composed of d_{zx}, d_{yz} and d_{xy} orbitals, respectively. The black curves are guides for the eyes. All images are adopted from [117]

points by the polarization-dependent ARPES [117].

The polarization ARPES image and its second derivative along the k_x direction are shown in Figs. 3.9(b) and (c), respectively. The left (right) panel is obtained by using s (p) polarization, and the measurement geometry is shown in Fig. 3.9(a). Light polarization $> 99\%$ is confirmed from the power of reflected light by Brewster's angle. The ARPES intensity changes drastically by changing the incident light polarization, reflecting the symmetry of eigenstates through the interaction between a photon and an electron in eq. (2.2). In particular, the eigenvalues of mirror operation for the d_{zx} orbital and s-polarization light are $+1$ and -1, respectively. Their products, observed through the photoexcitation process, should be $+1$. Thus, the ARPES intensity mainly derived from d_{zx} by using s polarization is suppressed, as shown in the left panel of Figs. 3.9 (b)-(d). The experimentally obtained orbital characters around the Γ point [as schematically shown in Fig. 3.9 (c)] clarify the opposite sign of orbital polarization compared to the M point [117]. The easy control of laser polarization by using wave plates is a powerful tool to detect the wave function symmetries.

3.6 Summary

In Chapter 3, we have presented the developed laser ARPES system with commercial nonlinear optical crystals. The achieved values are listed in Table 3.6.

Table 3.1: Achieved values of laser ARPES system developed in Ishizaka laboratory.

Photon energy	$5.90 \sim 6.43$ eV
Lowest temperature	~ 8 K
Energy resolution	< 0.9 meV
Momentum resolution	< 0.2 deg. (~ 0.002 Å^{-1})
Spot size	0.12 mm (horizontal) $\times$ 0.09 mm (vertical)
Light polarization	$> 99\%$

The high intensity of laser light coexisting with the good energy resolution of < 1 meV enables quick and precise measurements near the Fermi level. In addition, utilizing the small spot size and polarization of laser widens the range of target materials of the ARPES measurement

in a laboratory system. The combined ARPES system with the laser and He discharge lamp developed in Ishizaka laboratory will clarify various materials' electronic structures and unknown physical phenomena.

Chapter 4

Spin-valley coupling in 3R-polytype MoS_2

4.1 Introduction

The spin-momentum locked electronic structure is realized in bulk band dispersions of a noncentrosymmetric crystal structure. In this chapter, we present the results of an angle-resolved photoemission spectroscopy (ARPES) study on noncentrosymmetric transition metal dichalcogenide 3R-MoS_2 with three-fold rotational symmetry [131].

4.1.1 Spontaneous spin polarization in system with three-fold rotational symmetry

In nonmagnetic materials, the spin polarization in momentum space is achieved by the spin-orbit interaction (SOI). The effect of SOI in momentum space is understood as an interplay between the spin magnetic moment and orbital magnetic moment at each **k**-point. In the polar crystal structure [10,11,29,30,39–43,45–47,49,50], the non-zero y-component of orbital magnetic moment along the k_x direction can contribute to the helical spin texture in Rashba-type spin-splitting as schematically shown in Fig. 4.1(a) [26,27,132]. In particular, the orbital component of $(p_z + ip_x)$ [denoted by a blue maker ($\otimes$) in Fig. 4.1(a)] along the k_x direction is necessary for the Rashba-type spin-splitting in the p-electron polar system. It suggests that the polar system includes a dilemma in obtaining a large spin-splitting inherently because the orbital magnetic moment vertical to the crystal momentum vector should vanish at the Brillouin zone boundary

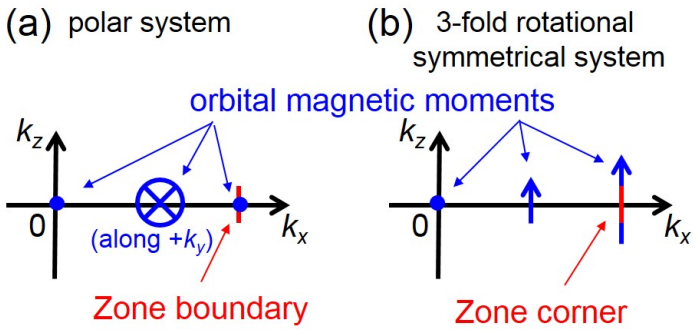

Figure 4.1: Schematic of orbital magnetic moments in **k**-space in the polar system (a) and system with three-fold rotational symmetry (b). The orientation of orbital magnetic moments are represented by a blue mark $\otimes$ (along $+k_y$ direction) and blue arrows (along $+k_z$ direction). Blue solid circles indicate the vanished orbital magnetic moments at the Brillouin zone center and/or boundary.

and center, which are represented by blue solid circles in Fig. 4.1(a). In other words, the non-zero magnetic quantum number l_y (l_x) along the k_x (k_y) direction cannot be a good quantum number even at the high symmetrical points in momentum space. It suppresses the energy of spin-splitting compared with the energy of atomic SOI over the entire Brillouin zone.

On the other hand, in the system with three-fold rotational symmetry, the non-zero magnetic quantum number can be a good quantum number at Brillouin zone corners as schematically shown in Fig. 4.1(b). For example, a band dispersion consisting of only a $(d_{x^2-y^2} + id_{xy})$ orbital component with the magnetic quantum number $l_z = -2$ can exist at the Brillouin zone corner. The well-defined non-zero integer magnetic quantum number l_z at the Brillouin zone corner yields the spin-polarization along the z direction with the large spin-splitting directly reflecting the strength of atomic SOI. In addition, such out-of-plane spin polarizations at the Brillouin zone corners are useful for spintronics function. It is known that the D'yakonov-Perel spin relaxation [133, 134], which is one of the spin-scattering mechanisms, is suppressed in the two-dimensional electrons system with the out-of-plane spin polarizations, resulting in the long lifetime of spin [135].

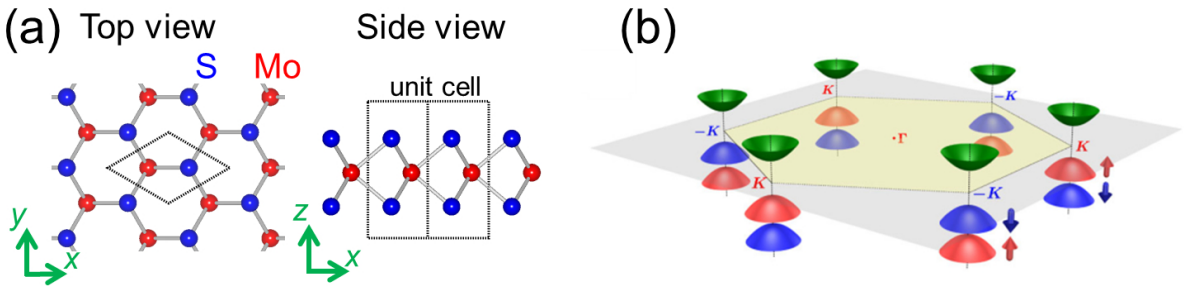

Figure 4.2: (a) Top and side view of crystal structure of monolayer MoS_2. Molybdenum (sulfur) atoms are denoted by red (blue) circles. (b) Schematic spin-valley coupled electronic structure in the momentum space in monolayer MoS_2 adopted from ref. [139]. Red and blue parabolic band dispersions at Brillouin zone corners ($\bar{K}$ and $-\bar{K}$ points) indicate the spin-splitting with the out-of-plane spin polarization.

4.1.2 Spin-valley coupling in monolayer transition metal dichalcogenide

Monolayer transition metal dichalcogenide (TMDC) MX_2 (M = Mo or W, X =S, Se) [136] has attracted attention as a candidate material for spintronics and valleytronics [6, 137] devices theoretically proposed in ref. [138, 139]. The top view of the monolayer MoS_2 shows the honeycomb-like crystal structure consisting of a molybdenum layer sandwiched by sulfur layers with three-fold rotational symmetry, as shown in Fig. 4.2(a). This three-fold rotational symmetry combined with the SOI of the Mo $4d$ orbital provides spin-polarized multi-valley electronic structures [138–140], which are defined as energetically degenerate band dispersions distinguished in momentum space, at the Brillouin zone corners in Fig. 4.2(b) adopted from ref. [139]. The valley degree of freedom as seen in silicon [141], diamond [142], AlAs [143–145], bismuth [146] and graphene [147–150], can be manipulated as an information carrier in the optical or transport experiments. For monolayer MoS_2, the photoluminescence circular dichroism [151–153] and the valley hall effect [154] reflecting the direct band gap at the inequivalent Brillouin zone corners have been experimentally confirmed. However, the direct observation or detection of the characteristic spin-valley coupled function in the group of monolayer TMDC has not occurred because of the difficulty in the fabrication of large area monolayer TMDC. Recently, CVD-grown [155] or MBE grown [156, 157] samples have enabled the *in situ* measurement to

observe its band dispersions by using ARPES and spin-resolved ARPES. This fabrication difficulty of monolayer TMDC still restricts the kinds of physical property measurements for the spin-valley coupled electronic structures and/or physical phenomena.

4.2 Rich polytypism in MoS_2

In this study, we have noted the rich polytypism in layered TMDCs. Usually, the monolayer MoS_2 is obtained by simple mechanical cleaving [the so-called scotch tape method [158]] from

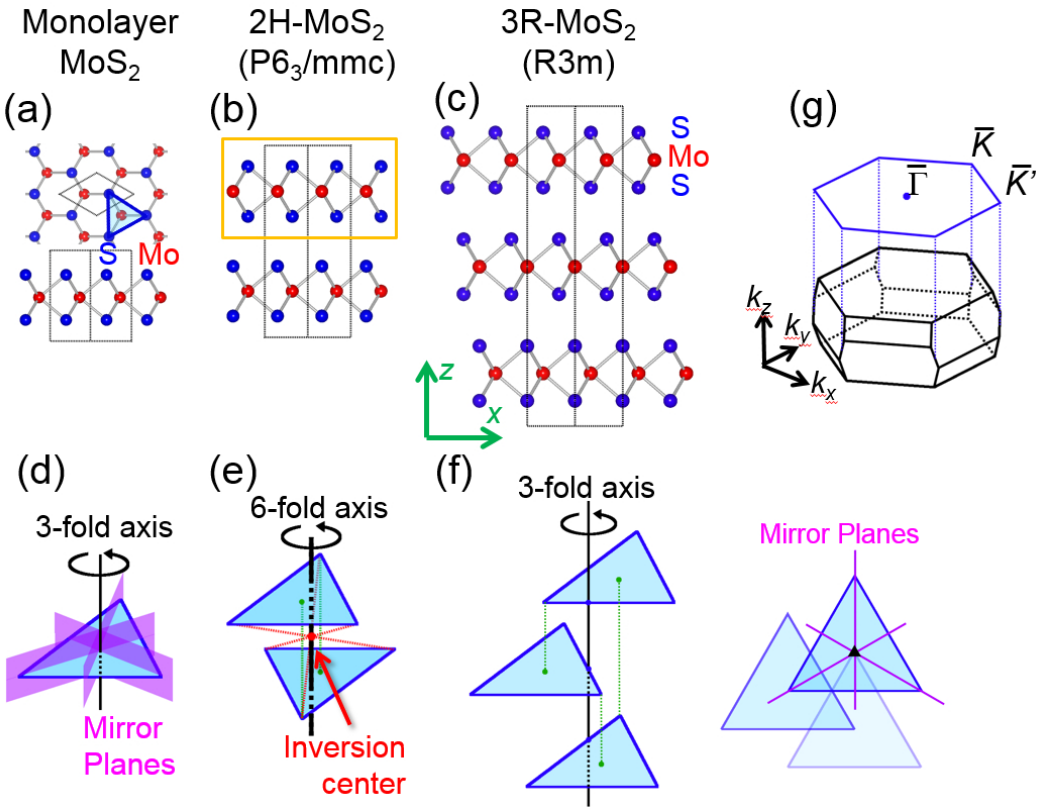

Figure 4.3: (a)-(c) Crystal structures of monolayer MoS_2, 2H-MoS_2 and 3R-MoS_2, respectively. (d)-(f) Schematics of the crystal symmetries in monolayer MoS_2, 2H-MoS_2 and 3R-MoS_2, respectively. A light-blue triangle represents the sulfur triangle lattice as denoted in (a). Purple planes or lines represent the crystal mirror planes parallel to the z axis. (g) First Brillouin zone of 3R-MoS_2. Blue flames represent the two dimensionally projected Brillouin zone with high symmetrical points ($\bar{\Gamma}$, $\bar{\mathrm{K}}$ and $\bar{\mathrm{K}}'$).

the stable bulk phase 2H-MoS_2 represented by the orange rectangle in Fig. 4.3(b). Crystal structures of the monlayer MoS_2 and 2H-MoS_2 are shown in Figs. 4.2(a) and (b), respectively. In Figs. 4.3(d) and (e), those crystal symmetries are schematically represented by using light-blue triangles indicating the sulfur triangle lattice denoted in Fig. 4.2(a). As discussed in the earlier section, the monolayer MoS_2 has a noncentrosymmetric crystal structure reflecting the three-fold rotational symmetry. On the other hand, the 2H-MoS_2 (belonging to space group $P6_3/mmc$) consisting of stacked monolayers has an inversion center with a six-fold rotational axis as shown in Fig. 4.2(e). Though it seems to lack inversion symmetry locally when observing the half unit cell represented by an orange rectangle in Fig. 4.3(b), such local inversion symmetry breaking reflecting the nonsymmorphic operations (glide mirrors or screw rotations) cannot generate net spin polarization in bulk [6, 25, 159, 160].

In MoS_2, as well as the most stable 2H-phase, the 3R-phase is known to exist as another stable phase [161–163]. The crystal structure and schematic of its symmetry are shown in Figs. 4.3(c) and (f) in the same manner as for the monolayer MoS_2 and 2H-MoS_2. The 3R-MoS_2 has a rhombohedral Bravais lattice (space group R3m), and its unit cell is composed of a trilayer (S-Mo-S) stacked in such a way that the three fold rotational symmetry is kept in the bulk form in

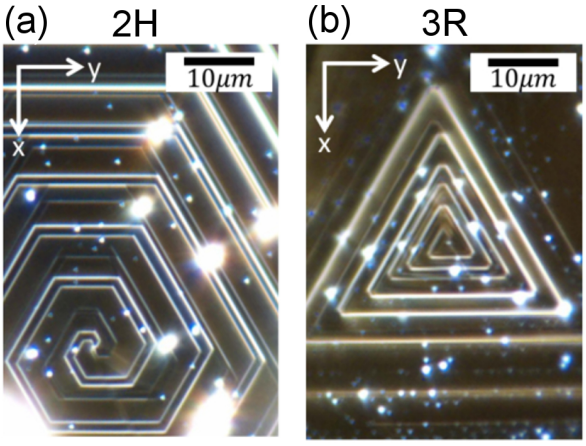

Figure 4.4: (a), (b) Optical micrographs of the surface of 2H-MoS_2 and 3R-MoS_2 crystals, respectively, showing contrasting screw dislocations reflecting the crystal symmetry. The images are provided by Mr. Suzuki (Iwasa group, Dept. of Appl. Physics, the University of Tokyo).

contrast to 2H-MoS_2 as schematically shown in Fig. 4.3(f). We note that the rhombohedral unit cell of 3R-MoS_2 includes only one Mo atom and two S atoms, giving simple band dispersions. The first Brillouin zone is shown in Fig. 4.3(g). Hereafter, for simply describing the ARPES results, we use the two-dimensionally projected Brillouin zone depicted by blue frames with two-dimensional high-symmetry points ($\bar{\Gamma}$, $\bar{\mathrm{K}}$, and $\bar{\mathrm{K}}'$). In the 3R-MoS_2, the spin-valley coupled electronic structure in bulk is expected to be similar to the monolayer MoS_2 reflecting the Van der Waals stacking nature of the TMDCs.

The large single crystal of 3R-MoS_2 (> 1 mm $\times$ 1 mm) and 2H-MoS_2 as a reference sample are provided by Mr. Suzuki (Iwasa group, Department of Applied Physics, the University of Tokyo). These samples are grown by using a chemical vapor transport technique, with Cl_2 and I_2 as carrier gases, respectively [162, 164]. Figures 4.4(a) and (b) present optical micrographs of typical surfaces of the 2H and 3R single crystals, respectively. The screw dislocations observed in these two forms of crystals have hexagonal and trigonal structures [163], respectively, clearly reflecting their crystal symmetries, as shown in Figs. 4.3(e) and (f).

4.3 Experimental setup and calculation condition

ARPES measurements ($h\nu$ = 21.2 and 40.8 eV) were performed at the Department of Applied Physics, the University of Tokyo, by using a VUV5000 He-discharge lamp and an R4000 hemispherical electron analyser (VG-Scienta). The total energy resolution was set to 10 meV and 20 meV for $h\nu = 21.2$ and 40.8 eV, respectively. Samples were cleaved *in situ* near room temperature and measured at 15 K.

Spin-resolved ARPES measurement utilizing the synchrotron beam ($h\nu = 20$ eV, p-polarized light) was performed at the Efficient SPin REsolved SpectroScOpy (ESPRESSO) end station attached to the APPLE-II type variable polarization undulator beam line (BL-9B) at the Hiroshima Synchrotron Radiation Centre (HSRC) [106]. The angular resolution was set to $\pm 0.75^\circ$ and the total energy resolution was set to 25 - 50 meV. Samples were cleaved *insitu* near room temperature and measured at 20 K.

SARPES with a HeI light source ($h\nu$ = 21.2 eV) was performed at BL19A in the photon

factory, KEK [103]. The spin analyzer in this system consists of a single VLEED spin detector. The angular resolution was set to $\pm 1^\circ$, and the total energy resolution was set to 100 meV. Samples were cleaved in situ near room temperature and measured at 110 K.

Band calculations were made by Dr. Akashi (Department of physics, the University of Tokyo) and Prof. Arita (RIKEN). The first-principles calculations for bulk systems were performed with the full-potential linearized augmented plane wave code WIEN2k [165]. We employed the generalized gradient approximation for the exchange-correlation functional [166]. For the input atomic configurations, we referred to previous experimental observations for the crystals [167, 168]. The muffin-tin radii for Mo and S atoms r_{Mo} and r_{S} were set to 2.40 and 2.13, respectively, and the maximum modulus for the reciprocal vectors K_{max} was chosen so that $r_S \times K_{max} = 7.00$.

4.4 Band dispersions obtained by ARPES and calculation

First, to figure out the whole band dispersions, we performed the ARPES measurement on 3R-MoS_2. The obtained ARPES image ($E - E_{\mathrm{F}}$ vs. momentum) of 3R-MoS_2 along the $\bar{\Gamma}$-$\bar{\mathrm{K}}$ line clearly shows the valence band dispersions spreading down to $E - E_{\mathrm{F}}$ = -8 eV in Fig. 4.5(a). Comparing the left panel (obtained by $h\nu$ = 40.8 eV) and the right panel (obtained by $h\nu$ = 21.2 eV), slight differences are observed at the top of the valence band at the $\bar{\Gamma}$ point. This photon energy dependence suggests that the corresponding band disperses three dimensionally (as explained in section 2.1.3). In the 3R-MoS_2, the maximum of valence bands (VBM) is located at the $\bar{\Gamma}$ point, in contrast to that of monolayer MoS_2 located at Brillouin zone corners. On the other hand, the top of valence bands at the $\bar{\mathrm{K}}$ point, which is very similar to that of monolayer MoS_2, shows no photon-energy dependence, indicating its two-dimensionality. These dimensionalities of valence bands are consistent with the electronic structure of monolayer MoS_2 [136, 138, 139, 155].

Focusing on the ARPES intensity near the Fermi-level multiplied by a factor of 100 in Fig. 4.5(a), energetically degenerate conduction band edges are faintly observed at the $\bar{\mathrm{K}}$ point and the middle point on the $\bar{\Gamma}$-$\bar{\mathrm{K}}$ line. The ARPES intensity mapping obtained by the photon energy

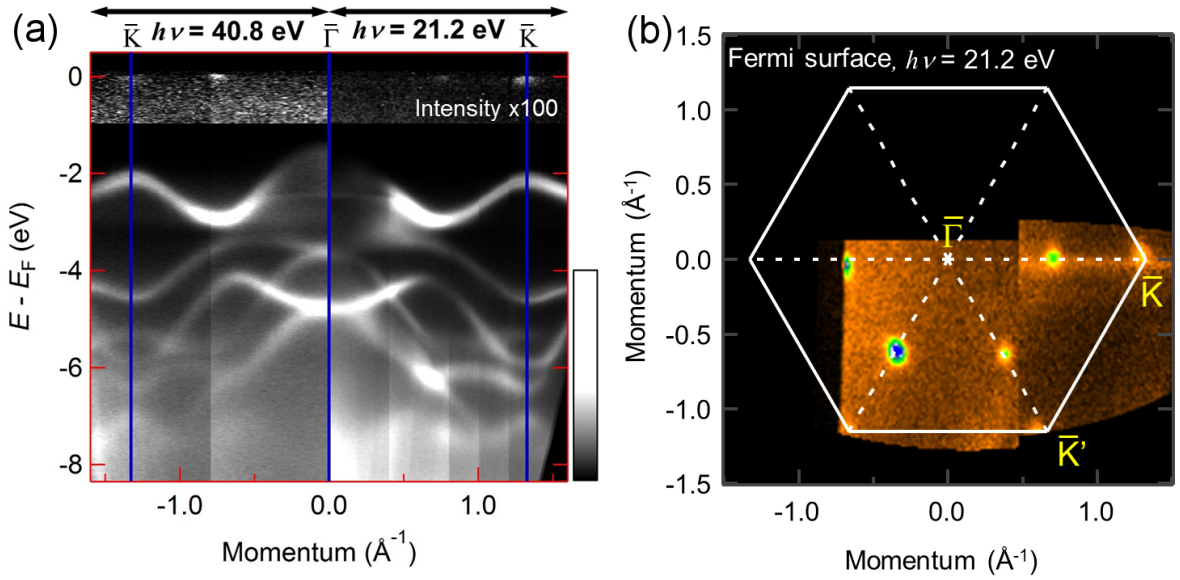

Figure 4.5: (a) ARPES image of 3R-MoS_2 along $\bar{\Gamma}$-$\bar{K}$ with $h\nu$ = 40.8 (left) and 21.2 (right) eV The intensity near the Fermi level is multiplied by a factor of 100. (b) ARPES intensity mapping at the Fermi level with the energy window of 16 meV. White frames represent the two-dimensional Brillouin zone with the high symmetrical points.

$h\nu$ = 21.2 eV at the Fermi level with the energy window of ±16 meV is shown in Fig. 4.5(b) with the two dimensional Brillouin zone (white). It clearly indicates the multi-valley conduction band structure ($\bar{K}$ point, $\bar{K}'$ point, and the middle points on the $\bar{\Gamma}$-$\bar{K}$ and $\bar{\Gamma}$-$\bar{K}'$ lines) as well as the valence band structure in the n-type semiconductor 3R-MoS_2. The indirect band-gap size between the VBM and Fermi level is evaluated to be 1.3 eV, and the direct energy gap at the Brillouin zone corners is evaluated to be 2.0 eV. Those parameters are comparable to those in 2H-MoS_2 [155,169], reflecting the van der Waals stacking nature of MoS_2. To evaluate the energy gaps of 3R-MoS_2 precisely, we should take account of the exciton effect on the conduction band edges at the Brillouin zone corners [131,164,170] and the band gap shrinkage effect observed on the surface of 2H-WSe_2 [171].

To discuss the characteristic electronic structure of 3R-MoS_2, bulk band dispersions of 3R-MoS_2 and 2H-MoS_2 along $\bar{K}'$-$\bar{\Gamma}$-$\bar{K}$ obtained by the first principles calculations and corresponding ARPES results along $\bar{\Gamma}$-$\bar{K}$ are shown in Figs. 4.6(a)-(d), respectively. The energy axes of the

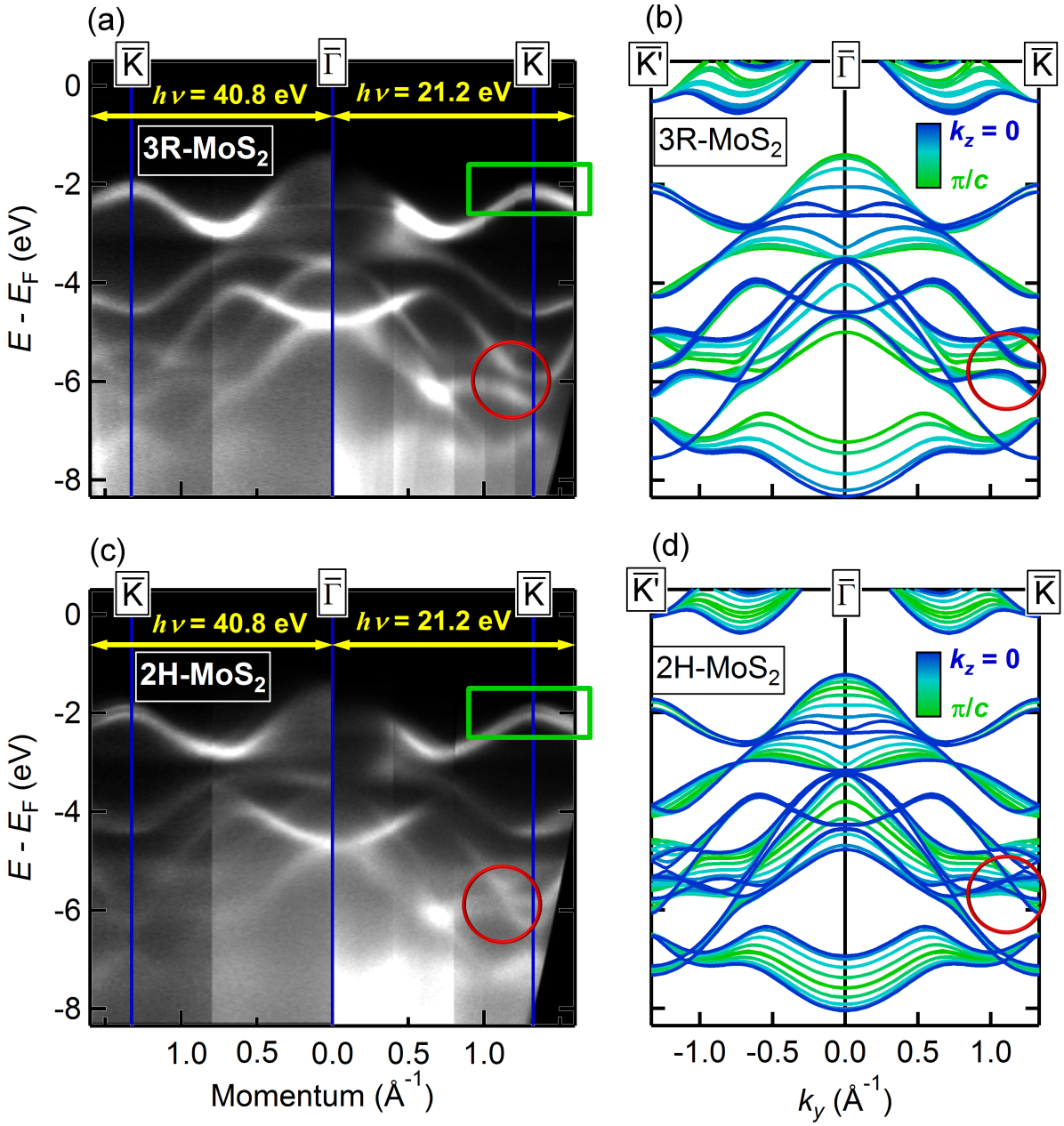

Figure 4.6: (a) ARPES image of the valence band structure of 3R-MoS_2 recorded along $\bar{\Gamma}$-$\bar{K}$ with $h\nu$ = 40.8 eV (left) and 21.2 eV. (b) Bulk band structure of 3R-MoS_2 along k_y obtained by the first-principles calculations. The band dispersions for various k_z, indicated by the inset color scale, are overlapped. The energy axis is shifted to match the top of the valence band at the $\bar{K}$ point to the ARPES result. (c), (d) Band structures of 2H-MoS_2 obtained by ARPES and calculation, as in (a), (b).

calculated results in Figs. 4.6(b) and (d) are shifted to match the energies of the top of valence band at $\bar{\mathrm{K}}$ point with the ARPES results. The band dispersions for various k_z are overlapped with corresponding colors indicated by the inset color-scale. Given that the ARPES images in Figs. 4.6(a) and (c) include the projection of finite k_z-dispersions, they are in good agreement with the calculated band dispersions in Figs. 4.6(b) and (d), respectively. The overall band dispersions of 3R- and 2H-MoS_2 are found to be very similar, reflecting the van der Waals stacking nature of TMDCs. On closely observing the detailed band dispersions, however, small but contrasting differences between the ARPES images of 3R- and 2H-MoS_2 can be observed. For example, near the $\bar{\mathrm{K}}$ point at $E - E_{\mathrm{F}} \sim -6$ eV represented by red circles in Figs. 4.6(a) and (c), bands are crossed in 2H-MoS_2 but not in 3R-MoS_2. Corresponding behaviors are also observed in the calculated results in Figs. 4.6(b) and (d). They suggest that the metastable phase of 3R-MoS_2 are separately synthesized from the 2H-phase.

4.5 Valence band top at $\bar{\mathrm{K}}$ point compared with 2H-MoS_2

Another difference between 3R- and 2H-MoS_2 can be seen at the top of the valence band at the $\bar{\mathrm{K}}$ point. Figures 4.7(a) and (c) show close-up views near the valence band top at the $\bar{\mathrm{K}}$ point for 3R-MoS_2 and 2H-MoS_2, respectively, and the measurement regions are denoted by green rectangles in Figs. 4.6(a) and (c). Corresponding calculation results are shown in Figs. 4.6(b) and (d), which indicate that those bands mainly consist of Mo orbitals. In both 3R- and 2H-MoS_2, similar band splittings at the Brillouin zone corners are observed in Figs. 4.6(a) and (c), respectively. The values of splitting (~ 0.14 eV for 3R and ~ 0.17 eV for 2H) agree well with those calculated as shown in Figs. 4.7(b) and (d), although there remains some ambiguity arising from the k_z-dependent dispersion.

Given the crystal symmetry of 3R- and 2H-MoS_2, it is found that these similar band splittings have different origins. As for the 2H-MoS_2, the band splitting consists of four bands with spin degeneracy due to the space inversion symmetry. These two sets of two bands are considered to be the bonding and anti-bonding state derived from two S-Mo-S layers in a unit cell. Without SOI, the 6_3 screw axis makes them stick on the $k_z = \pi/c$ plane [6] in the Brillouin zone. Then,

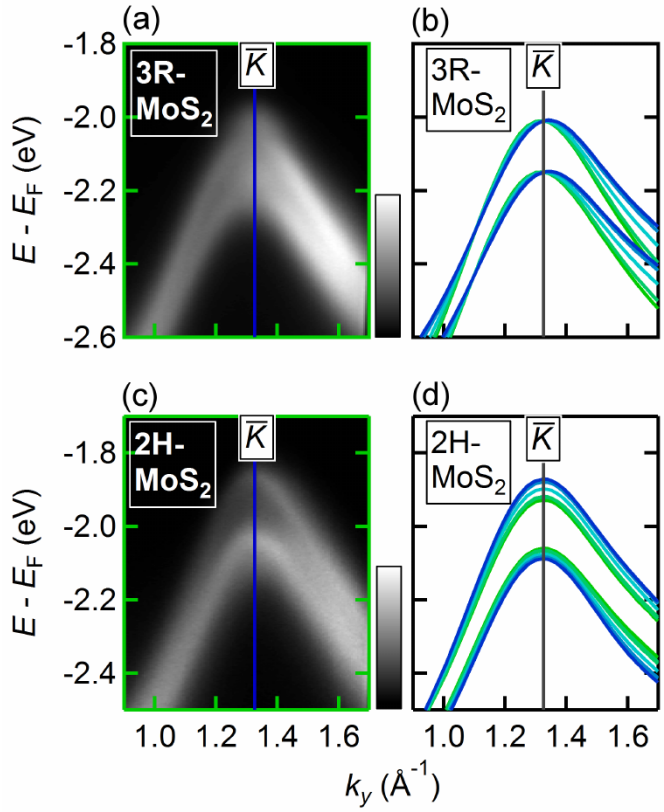

Figure 4.7: (a), (b) ARPES image and corresponding calculation, respectively, focusing on the region near the valence band top at the $\bar{\mathrm{K}}$ point for 3R-MoS_2. (c), (d) ARPES image and corresponding calculation for 2H-MoS_2, respectively. The measurement regions for (a) and (c) correspond to the green rectangles in Figs. 4.6(a) and (c), respectively.

the SOI can lift this band degeneracy resulting in the layer-locked staggered spin-polarization in bulk [160]. Except at $k_z = \pi/c$, this band splitting occurs owing to the coexistence of SOI splitting and the bonding and anti-bonding band splitting. These effects give the slight k_z dependence of the top of the valence band in 2H-MoS_2 as shown in Fig. 4.7(d).

On the other hand, the top of the valence band at the $\bar{\mathrm{K}}$ point of 3R-MoS_2 seems non-dispersive along the k_z direction. Because there is one Mo atom in a unit cell of 3R-MoS_2, this band splitting is not derived from the bonding and anti-bonding states. The band splittings in 3R-MoS_2 likely correspond to the spin-split band dispersions similar to those in monolayer

MoS_2 [138, 139] at Brillouin zone corners.

4.6 Spin-valley coupling at $\bar{\mathrm{K}}$ and $\bar{\mathrm{K}}'$ point

To detect spin-polarization on the top of the valence band, we carried out spin-resolved ARPES measurement for the noncentrosymmetric 3R-MoS_2 and centrosymmetric 2H-polytypes as references. By utilizing a three-dimensional spin polarimeter [106] (as shown in section. 2.2), spin polarizations along the x, y and z directions (P_x , P_y and P_z) can be measured. Figure 4.8(a) shows the ARPES intensity mapping of 3R-MoS_2 at $E - E_{\bar{\mathrm{K}}} = -0.3$ eV, where $E - E_{\bar{\mathrm{K}}}$ represents the energy level relative to the valence band maximum at the $\bar{\mathrm{K}}$ point. The experimentally obtained images indicate the existence of hole-like equi-energy surfaces around the $\bar{\Gamma}$, $\bar{\mathrm{K}}$ and $\bar{\mathrm{K}}'$ points. Upon closely examining the experimental images at the $\bar{\mathrm{K}}$ and $\bar{\mathrm{K}}'$ points, it is found that the hole-like equi-energy surfaces form double contours reflecting the band splitting as shown in Fig. 4.7(a). These are in good agreement with the calculated equi-energy contours which are colored by red and blue corresponding to the sign of $P_z > 0$ and < 0, respectively. As indicated by spin-resolved calculations as the red (spin-up) and blue (spin-down) curves in Fig. 4.8(g), the top of the valence band at the $\bar{\mathrm{K}}$ point is expected to show large SOI-induced Zeeman-type band splitting [172] with inverted spin polarization at the $\bar{\mathrm{K}}'$ point ($P_z \sim \pm 1$). Indeed, this was confirmed by the spin-resolved ARPES spectra in Fig. 4.8(b). The red (blue) curves indicate the intensity of spin-up (spin-down) components obtained at the $\bar{\mathrm{K}}$ point. The spectra for z-oriented spin s_z clearly show that the upper (lower) band at the $\bar{\mathrm{K}}$ point top is spin-up (spin-down) polarized, whereas the in-plane s_x and s_y components have nearly equivalent intensities. Figure 4.8(c) indeed shows almost full polarization along the z-direction ($P_z \sim \pm 1$), in contrast to the very small in-plane P_x, P_y. Furthermore, the spin-resolved ARPES s_z spectra for the $\bar{\mathrm{K}}$ and $\bar{\mathrm{K}}'$ points as shown in Fig. 4.8(d), clearly indicate the inversion of spin polarization for both upper and lower bands. It thus offers direct evidence of the valley/spin coupled state realized in bulk 3R-MoS_2, a counterpart of the recently reported Tl/Si(111) surface state [173]. In marked contrast, the valence band tops at the $\bar{\mathrm{K}}$ point for 2H-MoS_2 and 2H-WSe_2 are much less polarized, with negligible inequivalency of the spin-up and spin-down components in Fig.

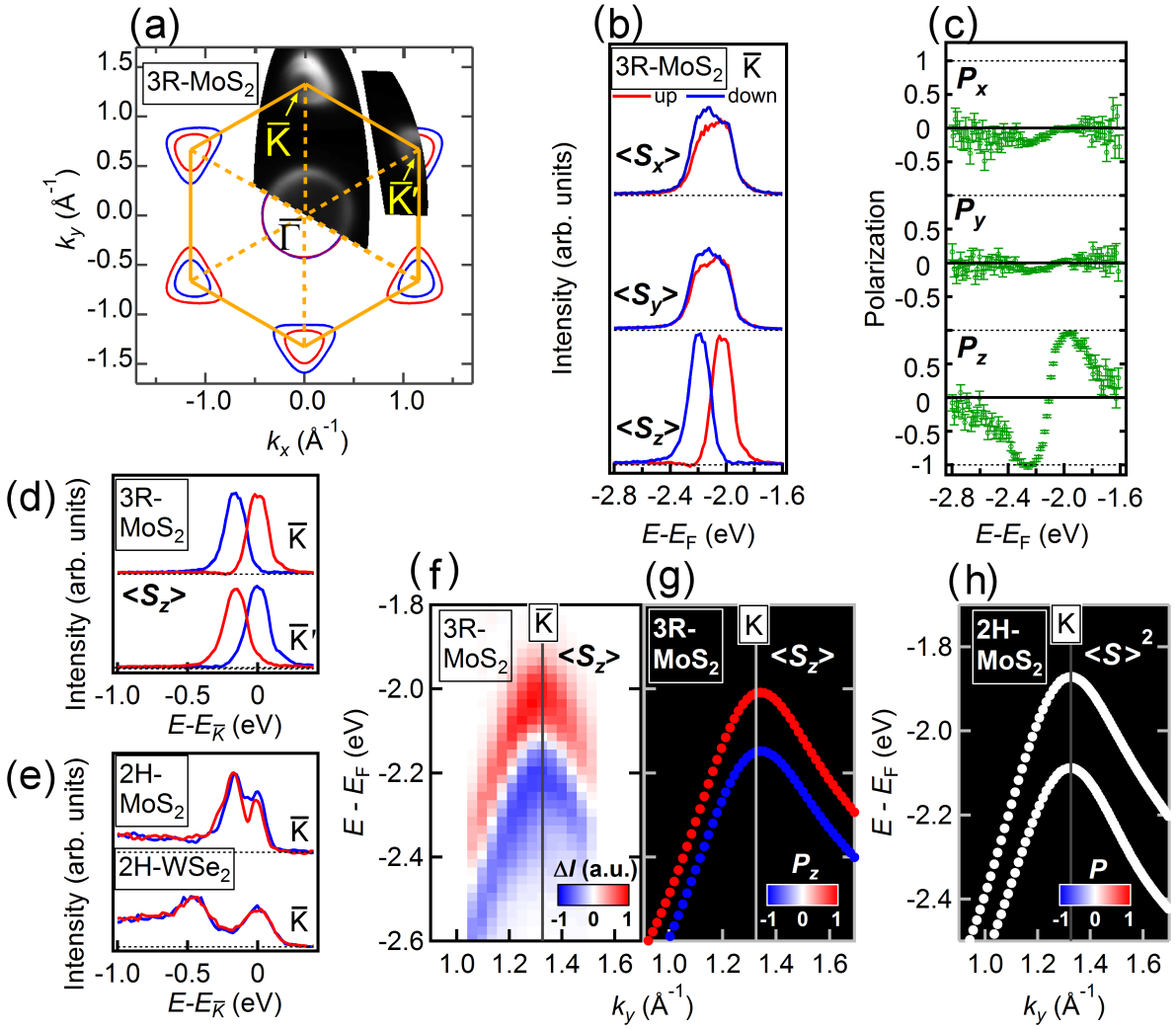

Figure 4.8: (a) Intensity mapping at 0.3 eV relative to the top of the valence band at the $\bar{K}$ point ($E - E_{\bar{K}} = -0.3$ eV) obtained by ARPES ($h\nu = 21.2$ eV) and the calculated equi-energy surfaces at $k_z = \pi/c$) overlaid on the two-dimensional first Brillouin zone. Hereafter, red and blue indicate spin-up and spin-down components, respectively. (b), (c) Spin-resolved energy distribution curves [EDCs, (b)] at the $\bar{K}$ point and the corresponding spin polarization with statistical errors of photoelectron counting [(c)] for 3R-MoS_2, obtained by spin-resolved ARPES. Here, the quantization axes of spin are along the x, y and z crystal axes defined in Fig. 4.3(g). (d) Spin-resolved EDCs for spin along the z axis, recorded at the inequivalent valleys of the $\bar{K}$ and $\bar{K}'$ points. (e) Spin-resolved EDCs at the $\bar{K}$ point from the centrosymmetric materials 2H-MoS_2 and 2H-WSe_2. (f) Spin-resolved ARPES image obtained by subtraction of the spin-resolved ARPES intensities for z-oriented spin-up and spin-down (ΔI) recorded along k_y. (g) Calculated spin polarizations P_z of the valence bands along (0, k_y, 0) for 3R-MoS_2. (h) Calculated total spin polarization of the valence bands along (0, k_y, 0) for centrosymmetric 2H-MoS_2.

4.8(e), as expected theoretically in Fig. 4.8(h). It suggests that the effect of inversion symmetry breaking at the surface can be ruled out as the origin of the huge spin splitting emerging in the 3R system. We should note that the net spin-polarization of $\sim 100\%$ is not derived from the local inversion symmetry breaking in 2H polytype [160] unless an atomically flat cleavage surface with a comparable size to the spot size of incident light is obtained. To demonstrate the spin-dependent valence band dispersion of 3R-MoS_2, the difference in s_z spin-up and spin-down spin-resolved ARPES intensities is shown in Fig. 4.8(f). This provides a firm and clear image of the out-of-plane spin polarization at the valence band top of the $\bar{\text{K}}$ point, in agreement with the calculation in Fig. 4.8(g).

4.7 Discussion: Interlayer hopping at Brillouin zone corners

The experimentally observed full spin-polarized ($P_z \sim \pm 1$) band dispersions at the Brillouin zone corners in 3R-MoS_2 are very similar to theoretically proposed ones of the monolayer MoS_2 [138, 139], even though they have different dimensions and crystal symmetries. This similarity is also confirmed in other experiments. Figure 4.9 adopted from ref. [131] shows the circular photoluminescence measurement result on the layer number (N) dependence of circular

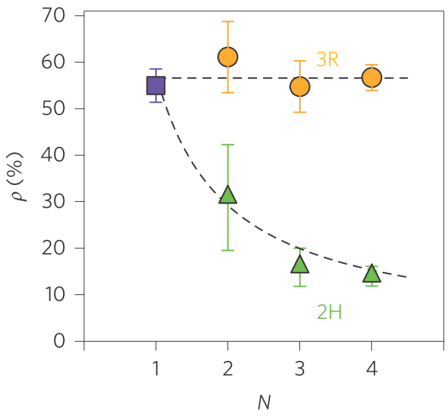

Figure 4.9: Layer number (N) dependence of circular polarization (ρ) obtained by the photoluminescence measurement for 2H- and 3R-stackings with error bars of experimental standard deviation for several samples. This image is adopted from ref. [131].

polarization (ρ) for 2H- and 3R-stackings. The observed polarization of the 3R-type stacking does not decrease with the stacking of S-Mo-S layers in contrast to 2H-type stacking. It experimentally supports that the 3R-MoS_2 possesses the same electronic structure at the Brillouin zone corners as with monolayer MoS_2. In this section, we discuss and evaluate this similarity by considering interlayer hoppings at the Brillouin zone corners in 3R-MoS_2 based on ref. [170].

To evaluate the interlayer hopping, we consider accompanied phases by three-fold rotational operation (C_3: $\frac{2}{3}\pi$ rotation). Figures 4.10(a)-(c) are adopted from ref. [170]. There are three different three fold rotational symmetry axes, α, β, and γ, on the monolayer MoS_2 as denoted in Fig. 4.10(a). The 3R-type stacking with the three-fold axes α, β, and γ for each S-Mo-S layer is schematically shown in Fig. 4.10(b). It indicates that the α, β, and γ axes are overlapped for the 3R-type stacking. The three-fold rotations around those axes are defined as $C_{3;j} \equiv RP_j$ ($j = \alpha$, β, and γ,), where R is a simple rotational operator described as $\exp(i\theta l_z)$ ($\theta = 2/3\pi$, l_z is the orbital magnetic moment) and P_j is the site permutation, which is schematically shown in Fig. 4.10(c) for the case of the α axis. Since the top of valence bands at the $\bar{\mathrm{K}}$ point mainly consist of Mo d orbitals with $l_z = -2$ [139], the acquired phase from the $2/3\pi$ rotation is $\exp(i\frac{2}{3}\pi)$. Furthermore, the contribution of site permutations to the phase around α, β, and γ axes are $\exp(i\frac{4}{3}\pi)$, $\exp(i\frac{2}{3}\pi)$, and 1, respectively.

The interlayer hopping amplitude (t) is defined by

$$t \equiv \langle \Psi_{\mathrm{K},1}|H|\Psi_{\mathrm{K},2}\rangle\,. \tag{4.1}$$

Here, $|\Psi_{\mathrm{K},}L\rangle$ denotes the $\bar{\mathrm{K}}$ point Bloch functions at the Lth layer, and H is the total Hamiltonian of the bulk crystal. Suppose C_3 denotes a certain three fold rotation under which H is invariant. Then,

$$\begin{aligned}
\langle \Psi_{\mathrm{K},1}|H|\Psi_{\mathrm{K},2}\rangle &= \langle \Psi_{\mathrm{K},1}|C_3^{-1}C_3HC_3^{-1}C_3|\Psi_{\mathrm{K},2}\rangle &(4.2)\\
&= (\langle \Psi_{\mathrm{K},1}|C_{3;j}^{-1})H|(C_{3;j'}\Psi_{\mathrm{K},2}\rangle) &(4.3)\\
&= \exp[-2\pi i\Delta_{12;\mathrm{j}\mathrm{j}'}]\langle \Psi_{\mathrm{K},1}|H|\Psi_{\mathrm{K},2}\rangle &(4.4)
\end{aligned}$$

where $\Delta_{12;jj'}$ is the phase acquired from the $2/3\pi$ rotation around the j and j'-axis for the Lth layer, respectively. In 3R-stacking, $(j, j') = (\alpha, \beta), (\beta, \gamma)$, and (γ, α) only appear for the

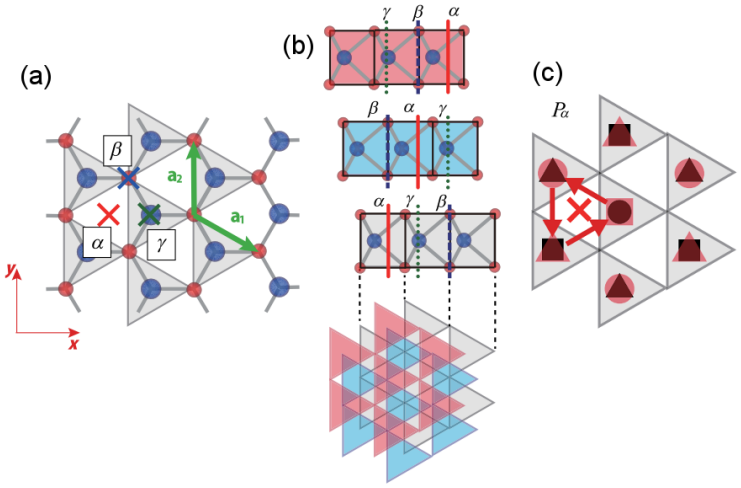

Figure 4.10: (a) Top-view of the monolayer MoS_2, where the trigonal prisms as shown in Fig. 4.3(a) are denoted by shaded triangles. α, β and γ represent inequivalent 3-fold rotational axes. a_1 and a_2 are primitive lattice vectors. (b) Side view (top) and top view (bottom) of the 3R-type stackings. The three fold rotational axes for each S-Mo-S layer are also indicated. (c) Schematic of the phase change due to site permutation around the α-axis. Real-space configuration of the phase of the $\bar{\mathrm{K}}$ point Bloch state $[\exp(i\mathbf{k}\cdot\mathbf{r})]$ is represented, where the circle, triangle, and square represent the three phase values 1, $e^{i(2\pi/3)}$ and $e^{i(4\pi/3)}$, respectively. All images are adopted from [170]

nearest-neighbor and next-nearest-neighbor interlayer hoppings as shown in 4.10(b). Since α, β, and γ axes yield the phases $\exp(i\frac{4}{3}\pi)$, $\exp(i\frac{2}{3}\pi)$, and 1 respectively, the non-zero phase term of $\Delta_{12;jj'}$ forces the interlayer hopping amplitude t to be zero.

This vanishing of interlayer hopping gives theoretical assurance of the spin-valley coupled electronic structure in bulk 3R-MoS_2, which is the same as that in monolayer MoS_2. Conversely, the experimentally observed multi-valley electronic structure with the full spin polarizations of $P_z \sim \pm 100\%$ on 3R-MoS_2 gives experimental support to the spin-valley coupling in monolayer MoS_2.

4.8 Summary

We have investigated the electronic structure of the n-type semiconductor 3R-MoS_2 by using ARPES and spin-resolved ARPES. Valence band dispersions down to $E - E_F \sim 8$ eV are clearly

observed on the single crystal of 3R-MoS_2. The valence band maximum is located at $E-E_F \sim 1.3$ eV at the Brillouin zone center (Γ point), and nearly degenerate bottoms of conduction bands touching the Fermi level are located at the Brillouin corners and the middle point between the Brillouin zone center and corners, forming the multi-valley electronic structure. They provide the indirect gap of ~ 1.3 eV in bulk 3R-MoS_2, in contrast to monolayer MoS_2 with the direct band gap of ~ 2.0 eV at the Brillouin zone corners.

The band dispersions of 3R-MoS_2 are very similar to centrosymmetric 2H-MoS_2, reflecting the van der Walls stacking. With the use of spin-resolved ARPES, the difference between them becomes clear. Only 3R-MoS_2 shows band splitting with net spin polarizations at the Brillouin zone corners owing to the three-fold rotational symmetry. It shows the full spin polarizations along the z-direction of $P_z \sim \pm 1$ at the inequivalent valleys ($\bar{K}$ and $\bar{K}'$ points), respectively. These results provide experimental evidence for the spin-valley coupled electronic structure in the noncentrosymmetric 3R-MoS_2, similar to those in the monolayer MoS_2.

The circular dichroic photoluminescence [131] and the first-principles calculation results [131, 170] suggest that the electronic structures at the Brillouin zone corners in the 3R-MoS_2 are two-dimensionally localized with the lack of interlayer hopping. Based on the group theoretical analysis on the 3R-MoS_2 [170], the nearest-neighbor and next-nearest-neighbor interlayer hopping are evaluated to be exactly zero. This clearly supports the out-of-plane full spin polarizations observed in the 3R-MoS_2, which are the same as those in the monolayer MoS_2 proposed theoretically [139].

The spin polarization at the high symmetrical point, where the non-zero orbital magnetic moment at each **k**-point can be a good quantum number, is realized in 3R-MoS_2. It is worth noting that the two-dimensional electronic structures are built in a three-dimensional crystal structure in 3R-MoS_2,providing the additional function as seen in circular dichroic photoluminescence. This study clarifies that the three fold rotational symmetrical system has an advantage for obtaining large spin-split band dispersions over the polar system.

Chapter 5

Topological surface states on superconductor β-$PdBi_2$

5.1 Introduction

The spin-momentum locked electronic structure emerges not only in bulk band dispersions of the noncentrosymmetric materials but also on the surface of materials. For example, the surface states of heavy metals [46, 48] show **k**-linear spin-splitting known as the Bychkov-Rashba effect [45]. Another example is a topological insulator, which is a new class of materials theoretically proposed by Kane and Mele [53], hosting the metallic spin-polarized surface states described by the massless Dirac fermion, as described in section 1.3. In this chapter, we present the electronic structure of superconductor β-$PdBi_2$ [174–176] in the normal state by using ARPES and spin-resolved ARPES. In the β-$PdBi_2$, topologically protected spin-polarized surface states similar to the topological insulator are realized in metallic band dispersions. At the end of this chapter, we discuss the origins of those topologically protected surface states.

5.1.1 Effect of spin-orbit interaction on Z_2 topological insulator's band dispersions

A topological insulator hosting the spin-momentum locked electronic structure has been realized in both two-dimensional [53–55, 59] and three-dimensional [57, 58, 60, 61] materials, regardless of the existence of space inversion symmetry breaking. The three-dimensional topological insulators are characterized by the four topological invariants as shown in ref. [56, 179]. One of those

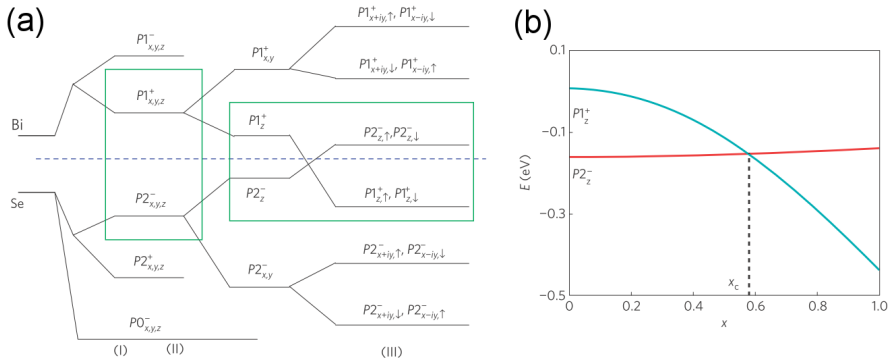

Figure 5.1: (a) Schematic energy level diagram of the evolution from the atomic orbitals (p_x, p_y and p_z) of bismuth and selenium into the conduction and valence bands of Bi_2Se_3 at the Γ point. The three different stages (I), (II), and (III) represent the effect of turning on chemical bonding, crystal-field splitting, and spin-orbit coupling, respectively. The blue dashed line represents the Fermi energy. (b) The energy levels $|P1_Z^+\rangle$ and $|P2_Z^-\rangle$ of Bi_2Se_3 at the Γ point versus an artificially rescaled atomic spin-orbit coupling $\lambda(\mathrm{Bi}) = x\lambda_0(\mathrm{Bi})$, $\lambda(\mathrm{Se}) = \lambda_0(\mathrm{Se})$. Here, λ_0 denotes the bear atomic spin-orbit coupling constant of bismuth ($\lambda_0 = 1.25$ eV) and selenium ($\lambda_0 = 0.22$ eV). A level crossing occurs between these two states at $x = x_c \simeq 0.6$. These graphs are adopted from ref. [62].

topological invariants, ν_0, indicates whether the system is a strong topological insulator ($\nu_0 = 1$), the topologically protected metallic surface states of which exist on all faces, or not ($\nu_0 = 0$). The physical meaning of $\nu_0 = 1$ is that an odd number of parity inversions across the band gap at the time-reversal invariant momenta [$\mathbf{k} \equiv -\mathbf{k}\,(\mathrm{mod}\,\mathbf{G})$] is necessary for the strong topological insulator with the inversion symmetry (as discussed in section 1.3.2). Spin-orbit interaction (SOI) can play an important role in the parity inversion in topological insulators. For typical strong topological insulators Bi_2Se_3 and Bi_2Te_3 [63–65] hosting the single Dirac cone surface states around the Brillouin zone center, parity inversion at the Γ point, driven by the spin-orbit interaction, occurs. A schematic of the energy levels at the Γ point for Bi_2Se_3 is shown in Fig. 5.1(a), which is adopted from ref. [62]. The three different stages (I), (II), and (III) represent the effect of turning on chemical bonding, crystal-field splitting and spin-orbit coupling, respectively. Without spin-orbit coupling (stage II), the conduction bands above (valence bands below) the Fermi level (represented by a blue broken line) mainly consist of Bi $6p$ (Se $4p$) orbitals. The

SOI decreases the energy level of the Bi $6p_z$ bonding state with even parity owing to mixing with in-plane orbital components, resulting in the parity inversion between the Se $4p_z$ anti-bonding state (stage III). Figure 5.1(b) adopted from [62] shows the energy-level dependence of the artificially rescaled SOI λ(Bi) = $x\lambda_0$(Bi) and λ(Se) = $x\lambda_0$(Se). Here, λ_0(Bi) = 1.25 eV and λ_0 (Se) = 0.22 eV are the realistic values of Bi and Se atomic spin-orbit coupling constants, respectively [174]. This indicates that the topological transition from the normal insulator into the topological insulator occurs at $x = x_c \simeq 0.6$.

As seen above, the SOI can trigger band inversion; then, the electronic structure in bulk is distinguished as the topologically non-trivial phase. In addiction to topological insulators, related topological materials such as topological crystalline insulators [66–68], Dirac/Weyl semimetals [73–83] and topological superconductors [69–72] are similarly characterized by the band inversions. Here, we introduce a superconductor β-$PdBi_2$ with a centrosymmetric tetragonal crystal structure [174–176]. Since the band dispersions of β-$PdBi_2$ consist of Pd $4d$ and Bi $6p$ orbitals, parity inversion is likely to occur between them at the boundary of the Pd $4d$ and Bi $6p$ local density of states. In addition, the strong atomic spin-orbit interaction of Bi $6p$ orbitals ($\lambda > 1$ eV) provides a drastic band modification suitable for the topologically non-trivial band dispersions.

5.2 Crystal structure and physical properties

The body-centered tetragonal crystal structure of β-$PdBi_2$(space group I4/mmm) with the lattice constants a = 3.362 Å and c = 12.983 Å [175] is shown in Fig. 5.2(a). Pd atoms, each located at the centre of a square prism of eight Bi atoms, form the layered crystal structure. $PdBi_2$ layers are stacked in the van der Waals nature, making it a feasible compound for cleaving. In this chapter, the x, y, and z axes are taken along the tetragonal crystal structure as shown in Fig. 5.2(a). The first Brillouin zone with the high-symmetry points (Γ, Z, N, X and M) is shown in Fig. 5.2(b). For simply describing the (S)ARPES results, hereafter, we use the projected two-dimensional (2D) surface Brillouin zone with 2D high-symmetry points ($\bar{\Gamma}$, $\bar{\mathrm{K}}$ and $\bar{\mathrm{M}}$) depicted in Fig. 5.2(b) by a green square.

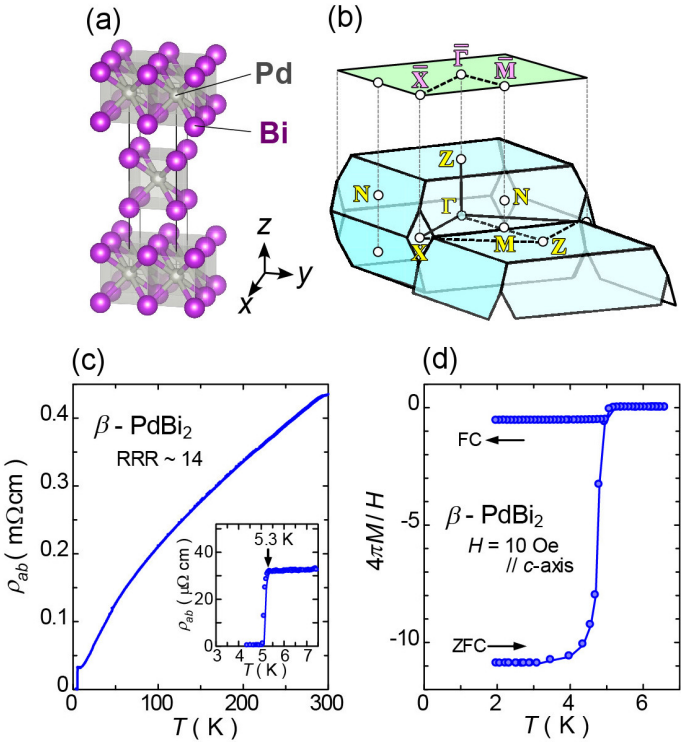

Figure 5.2: (a) Crystal structure of superconductor β-$PdBi_2$. x, y, and z axes are taken along the body-centered tetragonal crystal orientation. (b) The blue solid line (green plane) indicates the three (two)-dimensional Brillouin zone with high-symmetry points Γ, Z, N, X, and M ($\bar{\Gamma}$, $\bar{\mathrm{M}}$, and $\bar{\mathrm{X}}$) (c) In-plane electrical resistivity (ρ_{ab}) as a function of temperature (T). The inset shows ρ_{ab} near the critical temperature (5.3 K). (d) Magnetic susceptibility (χ) as a function of T, recorded under the field-cooled (FC) and zero-field-cooled (ZFC) conditions. A magnetic field of 10 Oe was applied along the c-axis direction.

The in-plane electric resistivity measured using a large single-crystalline β-$PdBi_2$ of good quality exhibits a high residual resistivity ratio ($\sim$ 14) and a clear superconducting transition at T_c = 5.3 K as shown in Fig. 5.2(c). The magnetic susceptibility of the sample also shows a clear sharp superconducting transition in bulk in Fig. 5.2(d). The single crystal of β-$PdBi_2$ ($\sim$ 1 cm $\times$ 1 cm) grown by a melt growth method and the transport measurement data were provided by Mr. Okawa (Sasagawa group, Materials and Structures Laboratory, Tokyo Institute of Technology).

5.3 Experimental setup and calculation condition

The ARPES measurement with the HeIα light source (21.2 eV) was performed at the Department of Applied Physics, The University of Tokyo, by using a VUV5000 He-discharge lamp and an R4000 hemispherical electron analyzer (VG Scienta). The total energy resolution was set to 10 meV. Samples were cleaved in situ at around room temperature and measured at 20 K.

Spin-resolved ARPES with the HeIα light source (21.2 eV) was performed at the Efcient SPin Resolved SpectroScOpy (ESPRESSO) end station attached to the APPLE-II-type variable polarization undulator beamline (BL-9B) at the Hiroshima Synchrotron Radiation Center (HSRC) [106]. The angular resolution was set to $\pm 1.5^\circ$, and the total energy resolution was set to 35 meV. Samples were cleaved in situ at around room temperature and measured at 20 K.

First-principles electronic structure calculations within the framework of the density functional theory were performed by Prof. Sasagawa (Materials and Structures Laboratory, Tokyo Institute of Technology) using the full-potential linearized augmented plane-wave method as implemented in the WIEN2k code [165], with the generalized gradient approximation of the Perdew, Burke, and Ernzerhof exchange-correlation function [166]. SOI was included as a second variational step with a basis of scalar-relativistic eigenfunctions. The experimental crystal data ($a = 3.362$ Å, $c = 12.983$ Å, z(Bi) $= 0.363$) were used for the bulk calculations. The (001) surface was simulated by a slab model: a stacking of 11 $PdBi_2$ -triple layers along the c axis with a 15 Å of vacuum layer, forming a tetragonal crystal structure of space group P4/mmm with the lattice constants of $a = 3.362$ Å and $c = 83.423$ Å. The plane-wave cutoff energy was set to $R_{\mathrm{MT}}K_{\mathrm{max}}$, where the muffin tin radii are $R_{\mathrm{MT}} = 2.5$ a.u. for both Bi and Pd. The Brillouin zone was sampled with the Monkhorst-Pack scheme [177] with momentum grids finer than $\Delta k = 0.02$ Å^{-1}(for example, a Γ-centred $38 \times 38 \times 38$ k-point mesh was used for the Fermi surface visualization, corresponding to $\Delta k = 0.009$ Å^{-1}).

5.4 Band dispersions: ARPES vs. calculation

The electronic structure of β-$PdBi_2$ observed using ARPES is shown in Figs. 5.3(c) and (d). The calculated Fermi surfaces as shown in Fig. 5.3(a), indicate the three-dimensionally dispersive

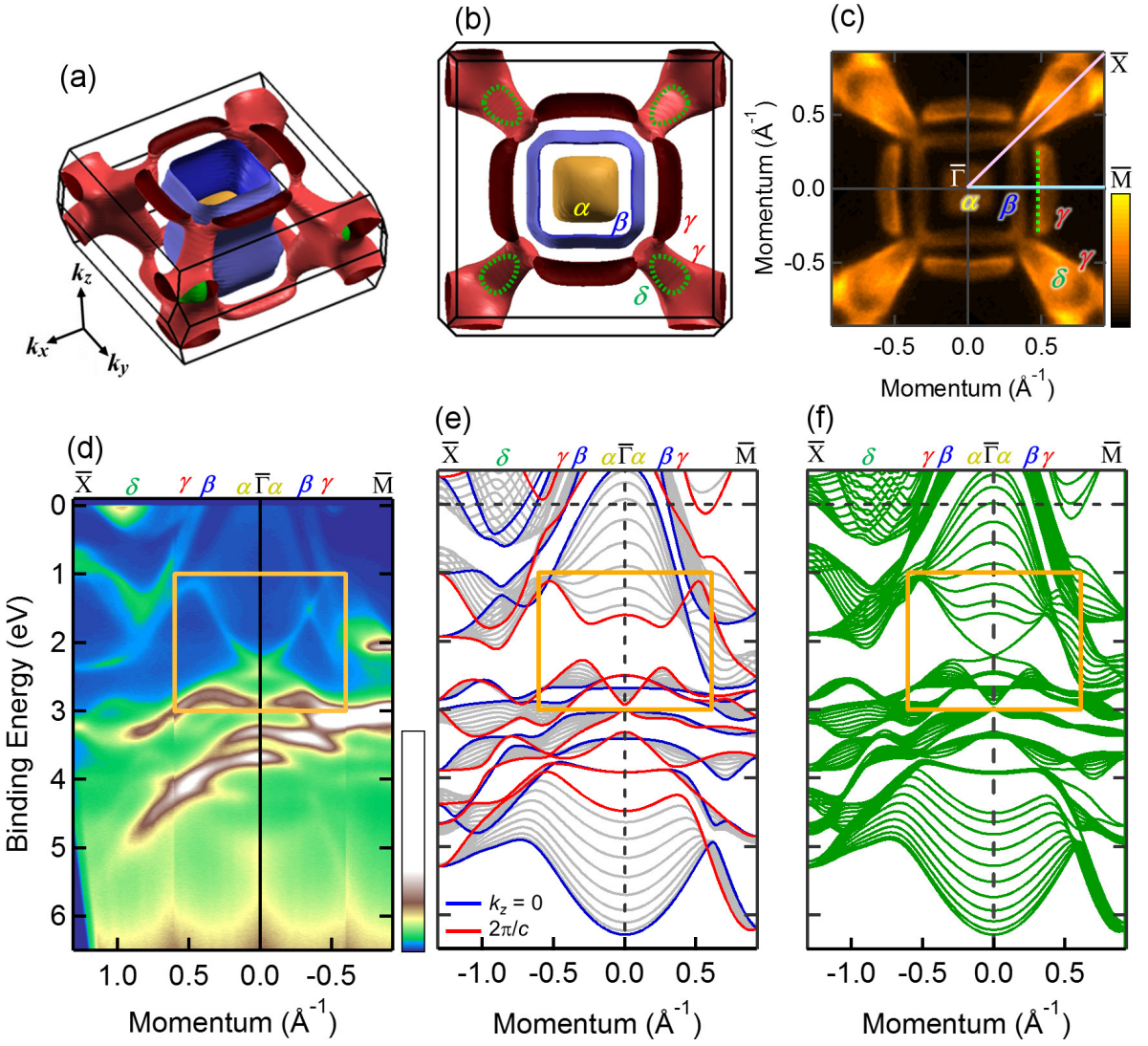

Figure 5.3: (a) Calculated Fermi surfaces shown with the first Brillouin zone. (b) Image of Fermi surfaces projected along the k_z direction. Two electron-like and two hole-like Fermi surfaces are denoted by α, β and γ, δ, respectively. Green broken contour line indicates the Fermi contour of δ at $k_z = 0$. (c) Four-fold symmetrized Fermi surface image recorded by ARPES. The image is obtained by integrating intensities in the energy window of ± 8 meV at the Fermi level. The color scale indicates the intensity. Surface state with sharp intensity denoted by the green broken line is discussed in detail in section 5.7. (d) ARPES image recorded along $\bar{\text{X}}$-$\bar{\Gamma}$ and $\bar{\Gamma}$-$\bar{\text{M}}$ cuts, shown as the light blue and pink lines in (c), respectively. The color scale indicates the intensity. (e) Calculated bulk band dispersions projected onto 2D surface Brillouin zone. Blue (Red) curves correspond to $k_z = 0$ ($2\pi/c$). (f) Surface band dispersions obtained by slab calculation of 11 $PdBi_2$-layers. Orange rectangles in (d)-(f) indicate the region where the surface Dirac cone appears.

electronic structure of β-$PdBi_2$. Considering that the ARPES intensity includes the integration of finite k_z-dispersions due to the surface sensitivity, the experimental Fermi surface mapping in Fig. 5.3(c) agrees well with the 2D projection of the calculated bulk Fermi surfaces [Fig. 5.3(b)]. The ARPES image in Fig. 5.3(d) is recorded along $\bar{\mathrm{X}}$-$\bar{\Gamma}$ and $\bar{\Gamma}$-$\bar{\mathrm{M}}$. Bands crossing the Fermi level E_F are predominantly derived from Bi 6p components with large dispersions from $E_\mathrm{B} \sim 6$ eV to above E_F. On the other hand, bands mainly consisting of Pd 4d orbitals are located around $E_\mathrm{B} = 2.5 \sim 5$ eV with rather small dispersions. Reflecting the difference of the photo-absorption cross sections of Bi 6p and Pd 4d orbitals (1 : 9.6 at 21.2 eV), the band dispersions mainly consisting of Pd 4d orbitals are comparatively brighter than those of Bi 6p in the ARPES image. Upon examining the region near E_F, two hole-like band dispersions (α, β) and one electron-like band dispersions (γ) are observed along $\bar{\Gamma}$-$\bar{\mathrm{M}}$. For $\bar{\mathrm{X}}$-$\bar{\Gamma}$, an electron-like band dispersion (δ) with a sharp ARPES intensity is additionally observed.

For comparison with ARPES, the calculation of bulk band dispersions projected onto the 2D Brillouin zone is shown in Fig. 5.3(e). Considering that the ARPES intensity includes the integration of finite k_z-dispersions due to the surface sensitivity, the overall electronic structure is in good agreement with the calculation. Two hole-like band dispersions (α and β) and two electron-like band dispersions (γ and δ) are well reproduced. Nevertheless, several differences can be noticed. The most prominent one appears in the orange rectangles in Figs. 5.3(d) and (e). A sharp Dirac-cone-like band dispersion is experimentally observed where the calculated bulk bands form a gap of ~ 0.55 eV around the $\bar{\Gamma}$ point. To confirm its origin, we performed a slab calculation for 11 $PdBi_2$ layers [Fig. 5.3(e)]. Apparently, a Dirac-cone-type dispersion appears in the gapped bulk states, showing a striking similarity to ARPES [Fig. 5.3(d)]. The observed Dirac-cone-like band dispersion is considered to be a two-dimensionally localized surface state.

5.5 Spin-polarized surface Dirac-cone band

Now, we focus on the observed surface Dirac-cone band. A close-up of the surface Dirac cone is shown in Fig. 5.4(a), indicating its crossing point at E_B= $E_\mathrm{D} = 2.41$ eV (E_D : the energy of the Dirac point where the bands cross each other). Such a clear Dirac-cone-shaped band strongly

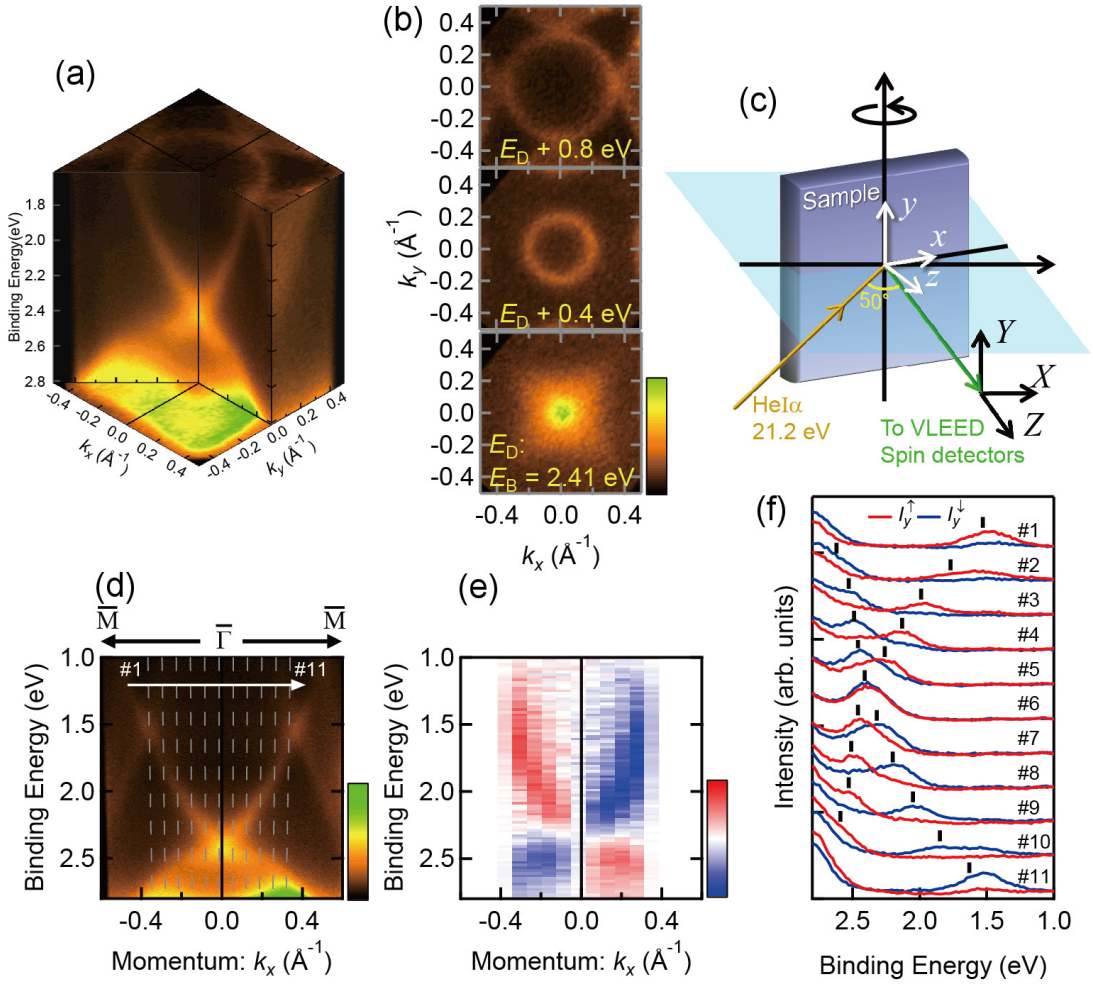

Figure 5.4: (a) Close-up of the observed surface Dirac-cone dispersions. (b) Constant energy cuts of surface Dirac cone at $E_B = E_D + 0.8$ eV, $E_D + 0.4$ eV and E_D (= 2.41 eV), respectively, where E_D is the band-crossing point of the surface Dirac cone. The color scale indicates the intensity. (c) Schematic of spin- and angular-resolved photoemission spectroscopy (SARPES) experimental geometry using the HeIα light source (21.2 eV) and very-low-energy electron diffraction (VLEED) spin detectors. (d) Intensity image of the surface Dirac cone along $\bar{\Gamma}$-$\bar{\mathrm{M}}$. The color scale indicates the intensity. Grey broken lines (# 1-11) represent the measurement cuts for energy distribution curves (EDC) shown in (f). (e) Spin-resolved image of the surface Dirac-cone dispersions for spin y-component. The color scale indicates the spin polarization P_y, from $P_y = -1$ (blue) to $P_y = +1$ (red). (f) Spin-resolved EDCs for momenta # 111 as shown in d. Red (blue) curves show the spin-up (spin-down) component of the intensity, $I_y^{\uparrow}$ ($I_y^{\downarrow}$). The black markers denote the peak positions of the EDC in (d).

reminds us of the helical edge states in three-dimensional (3D) strong topological insulators. We can see the very isotropic character of the surface Dirac cone in its constant-energy cuts [Fig. 5.4(b)], appearing as a perfectly circular contour even at $E_{\rm B}$= $E_{\rm D}$ − 0.8 eV with a large momentum radius of 0.3 Å^{-1}. It reflects the C_{4v} point group symmetry on the surface, in contrast to the warping effect often appearing in trigonal strong topological insulators [178]. The spin polarization of the surface Dirac cone is also directly confirmed by SARPES experiments as depicted in Fig. 5.4(c) [106]. Figures 5.4(e) and (f) show the results for the y-component spin, measured along k_x ($\bar{\Gamma}\bar{\rm M}$). Because of C_{4v} symmetry, x-and z-components are forbidden. The red (blue) curves in Fig. 5.4(f), indicating the energy distribution curves of spin-up (-down) components, clearly show the spin-polarized band dispersions. As easily seen in the SARPES image (Fig. 5.4(e)), spin polarization with spin-up (spin-down) for negative (positive) dispersion of the surface Dirac cone is confirmed. The observed spin-polarized surface Dirac cone thus presents a strong resemblance to the helical surface state in strong topological insulators.

5.6 Parity analysis for Z_2 topological invariant

To evaluate whether the observed surface state is topologically non-trivial, we derive the Z_2 invariant ν_0 for β-PdBi$_2$, in analogy to 3D strong topological insulators [57, 179]. For 3D band insulators with inversion symmetry, the ν_0 obtained from the parity eigenvalues of filled valence bands at eight time-reversal invariant momenta (TRIM) [where $\mathbf{k} \equiv -\mathbf{k}$ (mod $\mathbf{G}$), $\mathbf{G}$ is the reciprocal vector] indicates whether it is a strong topological insulator ($\nu_0 = 1$) or not ($\nu_0 = 0$). The bulk β-PdBi$_2$ is apparently a metal; nevertheless, here we define a gap in which there is no crossing of the bulk band dispersions through the entire Brillouin zone as schematically shown in Fig. 5.5(e). By considering this gap, we discuss its topological aspect by calculating ν_0. The calculated bulk band structure without and with SOI are shown in Figs. 5.5(a) and (b), respectively. The valence bands are identified by numbers (from 1st to 10th), as indicated on the right side of respective graphs. The bands are numbered by the energy (E) at the Z point. Note that all bands are doubly spin-degenerate owing to the space inversion symmetry. By comparing Fig. 5.5(a) and (b), we notice that many anti-crossings are introduced by spin-orbit interaction,

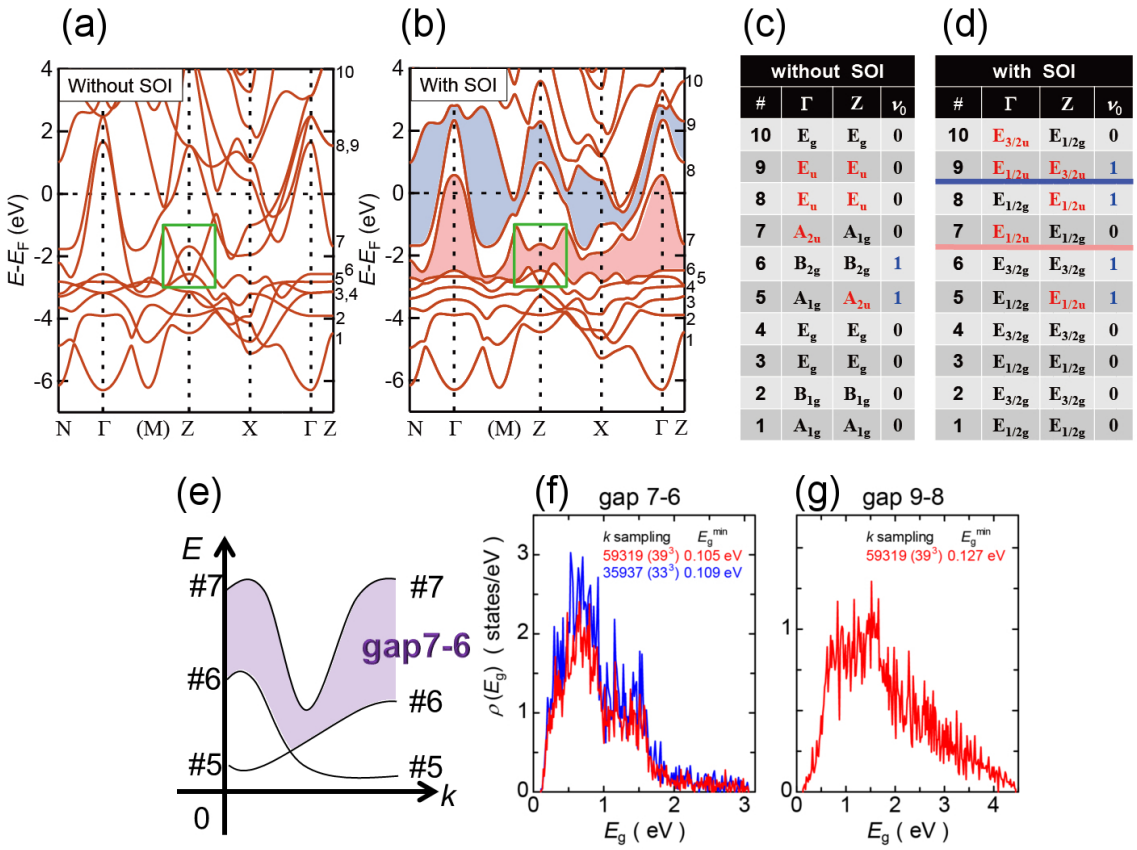

Figure 5.5: (a) (b) First-principles band calculations without and with spin-orbit interaction (SOI), respectively. Valence bands are numbered by the energy (E) at the Z point, as shown in the right side of panels. The green rectangles indicate the energy region where the surface Dirac-cone appears. The pink (blue) shaded area in (b) shows gap 7-6 (gap 9-8) induced by SOI. (c) (d) Lists of the topological invariant ν_0 and the symmetries of wave-functions at the Γ and Z points without and with SOI, respectively. The left end columns (#) indicate the number of the valence bands as given in (a) and (b). The symmetries indicated with red (black) have the odd- (even-) parity. $\nu_0 = 1$ indicates the topologically nontrivial band-inverted state. The pink (blue) line in (d) denotes gap 7-6 (gap 9-8). (e) Schematic of the definition of gap 7-6. (f) The distribution of the direct gap (E_g) for gap 7-6 showing the minimum direct gap of 0.105 eV (0.109 eV) by k sampling of 39^3 (33^3) obtained by the band calculation. (g) The distribution of the direct gap (E_g) for gap 9-8 showing the minimum direct gap of 0.123 eV by k sampling of 39^3 obtained by the band calculation.

including the ~ 0.55 eV gap opening in the green rectangular region, where the surface Dirac cone appears. Here, we focus on the gap between the 7th and 6th bulk bands, namely gap 7-6, shaded by pink in Fig. 5.5(b). The distribution of the direct gap between the 7th and 6th bands can be evaluated by the joint density of states as a function of the gap energy E_g, defined as

$$\rho(e_g) = \sum_{\mathbf{k}} \delta(E_g - [E_7(\mathbf{k}) - E_6(\mathbf{k})]). \tag{5.1}$$

The result for gap 7-6 is shown in Fig. 5.3(f), which guarantees minimum value of 0.105 eV for the gap opening between the 7th and 6th bands through the entire Brillouin zone.

By considering the obtained gap, we discuss its topological aspect by calculating ν_0 in analogy to 3D strong topological insulators. As shown in Fig. 5.2(b), the eight TRIM in the Brillouin zone of β-PdBi$_2$ with I4/mmm symmetry are Γ, Z, two X, and four N points. Considering these TRIM, the Z_2 invariant for the gap between the $(N+1)$-th and N-th bulk bands, $\nu_0(N)$, can be calculated by

$$(-1)^{\nu_0(N)} = \prod_{i=1}^{8} \prod_{m=1}^{N} \xi_m(\Gamma_i), \tag{5.2}$$

where $\xi_m(\Gamma_i)$ represents the parity eigenvalue (± 1) of the m-th band at the i-th TRIM. Note that, since there are even numbers of X and N points, only $\Gamma_i = \Gamma$ and Z contribute to the calculation of ν_0 (N); that is,

$$(-1)^{\nu_0(N)} = \prod_{m=1}^{N} \xi_m(\Gamma)\xi_m(\mathrm{Z}). \tag{5.3}$$

Thus, ν_0 can be calculated by considering solely the Γ and Z point, the symmetries of wave functions of which are listed in Fig. 5.5(d) for respective bands. Those indicated by red (black) are of odd (even) parity. We find that gap 7-6 is characterized by $\nu_0(6) = 1$, indicating its analogy to 3D strong topological insulators. This requires an odd number of surface states connecting the 7th and 6th bands to topologically link the bulk β-PdBi$_2$ and vacuum. The observation of a spin-helical surface Dirac cone in gap 7-6 clearly represents the characters of such topologically protected surface states.

5.7 Topologically protected surface state near Fermi level

By further examining the list of ν_0 in Fig. 5.5(d), we notice $\nu_0(8) = 1$ for gap 9-8 shaded by blue in Fig. 5.5(b), which has the minimum gap of 0.127 eV, as confirmed by the calculation [Fig. 5.5(g)]. It suggests that topological surface states connecting the 9th and 8th bands must exist, where we may observe the effect of superconductivity if located sufficiently close to $E_{\rm F}$. To clarify this possibility, a close-up of the ARPES image near $E_{\rm F}$ is shown with the calculation in Figs. 5.6(b) and (c). The green curves in Fig. 5.6(c) indicate the calculated surface states crossing $E_{\rm F}$ separately from the 2D projected bulk bands shaded by gray. They appear at the smaller-k_x side of β (8th) and γ (9th) bands. Experimentally, the sharp peaks indicative of 2D surface states are observed in the momentum distribution curve at $E_{\rm F}$, as denoted by S1 and S2 in Fig. 5.6(a). As can be seen in the list of ν_0 in Fig. 5.5(d), S2 should be the topological surface state connecting the 9th and 8th bands ($\nu_0(8) = 1$), whereas S1 appearing in gap 8-7 must be trivial ($\nu_0(7) = 0$).

The spin polarization of the topological surface state S2 as well as the trivial surface state S1 is also confirmed experimentally. As shown in Fig. 5.6(d), the y-oriented spin polarizations of S1 (#2−5) and S2 (#7−10) along k_x ($\bar{\Gamma}$-$\bar{\rm M}$) are clearly observed in the spin-resolved spectra. Here, the peak positions for S1 and S2 (bulk β) bands are depicted by green circles (black squares). We can see that S1 and S2 are both spin polarized with spin-up for $k_x > 0$, whereas they get inverted for $k_x < 0$ [Figs. 5.6(e) and (f)], as required by the time-reversal symmetry. These clearly indicate that both topological and trivial surface states crossing $E_{\rm F}$ possess the in-plane spin polarizations.

The Z_2 invariant analysis shows that an odd number of gapless surface states in gap 9-8, connecting the 9th and 8th bands, must exist between $\bar{\Gamma}$-$\bar{\rm M}$. To confirm whether the experimentally observed S2 indeed corresponds to this topological surface state, we need to examine the slab calculation carefully since S2 crosses $E_{\rm F}$ and extends to the unoccupied state. By tracking the calculated data from $\bar{\rm M}$ towards $\bar{\Gamma}$ [Fig. 5.7(a)], we first notice that S2 is derived from the local minimum of the 9th (γ) band. S2 then crosses $E_{\rm F}$ and reaches up to $E-E_{\rm F}$= 2 eV without merging into the bulk states. At $\bar{\Gamma}$, although it gets overlapped with 2D projected bulk

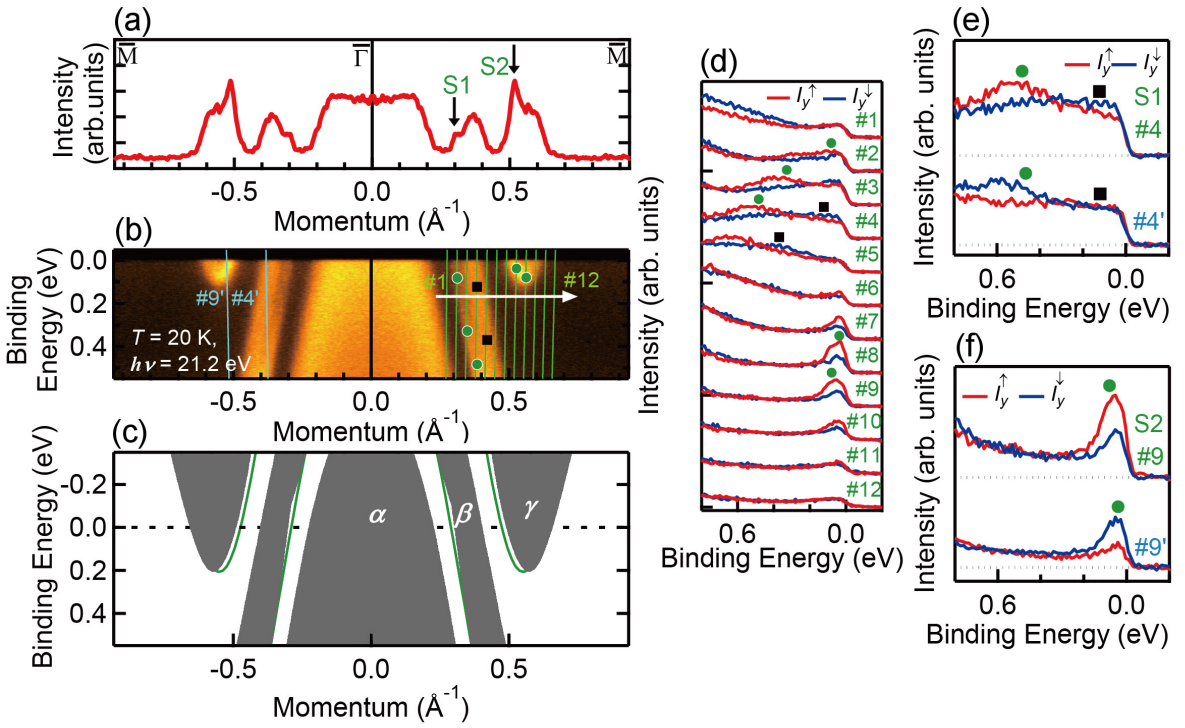

Figure 5.6: (a)-(c) Momentum-distribution curve obtained by integrating the intensity in the energy window of ± 10 meV at the Fermi level, the intensity image, and the calculation, respectively, shown along $\bar{\Gamma}$-$\bar{M}$ The black arrows in (a) indicate the intensities from two different surface bands denoted by S1 and S2. Green circles (black squares) depicted in (b) are the peak positions of energy- and momentum- distribution curves for surface (bulk) bands. In (c), surface band dispersions (green) are overlaid to two-dimensional projected bulk bands (gray), namely the 7th (α), 8th (β), and 9th (γ) bands. (d) Spin-resolved spectra recorded at momenta #1 $\sim$ #12, as shown in (b). (e), (f) Spin-resolved spectra for S1 at momenta #4 and #4$'$ in (b), and for S2 at momenta #9 and #9$'$ in (b), respectively. Red (blue) curves in df show the spin-up (spin-down) component of the intensity for spin-y, $I_y^{\uparrow}$ ($I_y^{\downarrow}$). Green circles (black squares) depicted in (d)-(f) are identical to those in (b).

bands, we can distinguish S2 forming a Rashba-like crossing point at $E-E_{\rm F}=$ 2.4 eV. After the crossing, the S2 band eventually gets merged into the 8th (β) band. It thus shows that S2 indeed connects the 9th and 8th bands. The crossing of the S2 surface band at $\bar{\Gamma}$ is more clearly seen by comparing the 2D projected bulk [Fig. 5.7(b)] and the slab [Fig. 5.7(c)] calculations magnified near the crossing point. The crossing of the S2 surface band at $\bar{\Gamma}$ is distinguished

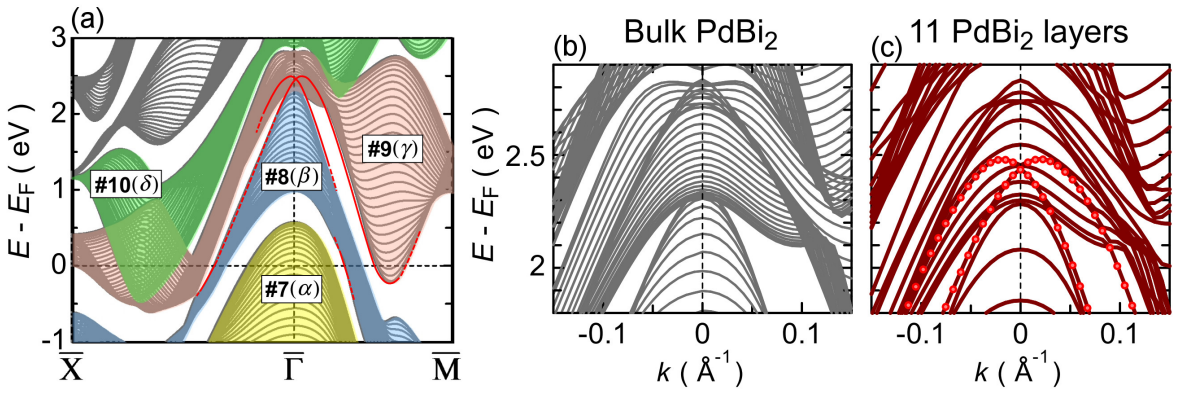

Figure 5.7: (a) Two-dimensional projected bulk bands and the surface state bands obtained by the calculation. The energy (E) relative to the Fermi level (E_{F}) is plotted along $\bar{\mathrm{X}}$-$\bar{\Gamma}$ and $\bar{\Gamma}$-$\bar{\mathrm{M}}$. Those crossing the Fermi level are painted by colors; yellow for 7th (α), blue for 8th (β), pink for 9th (γ), and green for the 10th (δ) bands. The surface-state bands crossing the Fermi level are depicted by the red curves. (b), (c) The calculated band dispersions for the bulk $PdBi_2$ and for the slab of 11 $PdBi_2$ layers, respectively, magnified near the band crossing point. $E-E_{\mathrm{F}}$ for respective bands are plotted as a function of momentum $\mathbf{k}$. The bands at the topmost surface are highlighted by red markers in (c).

in Fig. 5.7(c) by following the eigenenergies highlighted with the red markers. Note that no such crossing exists for the calculation of bulk in Fig. 5.7(b). S2 thus possesses a similarity to the Dirac cone that connects the gap with the crossing at $\bar{\Gamma}$, and it is indeed a topologically protected surface state.

5.8 Discussion: Origins of parity inversions

The spin polarization in the topological surface states originate from SOI, but SOI is not necessary for the parity-inverted band structure realized in gap 7-6 as shown in Fig. 5.4(d). Here, we discuss how the parity inversion occurs with and without the help of SOI for gap 9-8 and gap 7-6 by considering the energy levels of the related molecular orbitals [180, 181] at the Γ and Z points.

5.8.1 Parity inversion for gap 9-8

For the case of S2 in gap 9-8, we can see ν_0 changing to 1 through SOI, as shown in Figs. 5.5(c) and (d). Figures 5.8(a) and (b) show close-up views of calculated band dispersions along the Γ-Z line without and with SOI, respectively. The band indices and irreducible representations in the graphs correspond to those in Figs. 5.5(c) and (d), respectively. The band dispersions with odd (even) parity at the high symmetry points (Γ and Z points) are denoted by red (black) circles. They indicate that band inversion occurs at the Γ point between $E_{1/2g}$ and {$E_{1/2u}$ and $E_{3/2u}$} states with the help of SOI as represented by black and red arrows in Figs. 5.8(a) and (b). Since the band dispersions above the Fermi level mainly consist of Bi $6p$ orbitals, these drastic band modifications reflect the strong atomic SOI of the Bi atom. Roughly speaking, the origin of this band inversion can be understood as the strength of SOI overcomes the energy gap between the bonding (E_u) and the anti-bonding state (E_g) of Bi $\{6p_x, 6p_y\}$ orbitals at only the Γ point. Usually, the energy difference between the anti-bonding state and bonding states becomes minimum at Brillouin zone boundaries, in contrast to the current case. The energy levels of Bi $\{6p_x, 6p_y\}$ states in a body-centered unit cell are understood by using the schematics of molecular orbitals, as shown in Figs. 5.9(b)-(d). These correspond to the wave function of

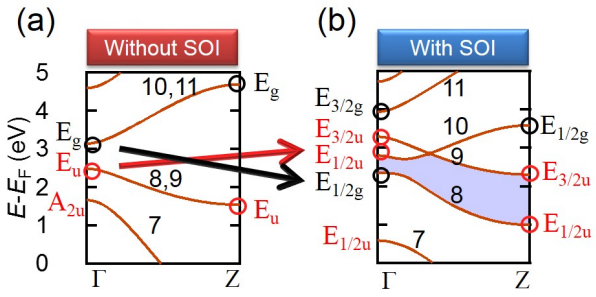

Figure 5.8: (a), (b) Calculated band dispersion along Γ-Z above the Fermi level without and with SOI. The band indices #7 ∼ #11 and irreducible representations corresponding to Figs. 5.5(a)-(d) are represented in graphs. The band dispersions with odd (even) parity at the high symmetry points (Γ and Z points) are denoted by the red (black) circles. The parity inverted gap 9-8 is shaded by blue in (b).

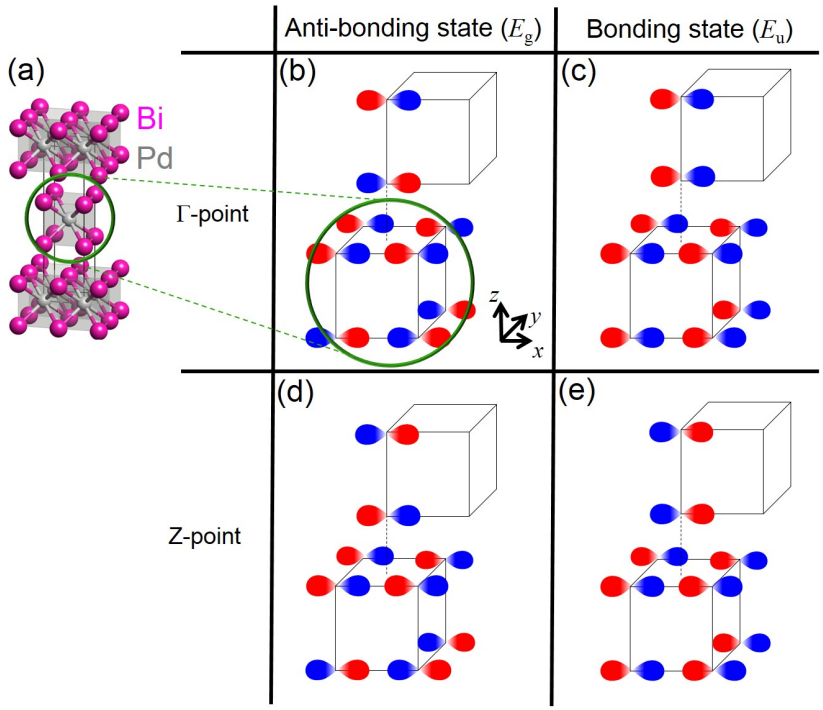

Figure 5.9: (a) Body-centered tetragonal crystal structure of β-$PdBi_2$. (b)-(d) Schematics of the molecular orbitals of Bi $6p$ orbitals for the anti-bonding state (E_g) and bonding state (E_u) at the Γ and Z point in the absence of SOI. A tetragonal parallelepiped represents the square prism of eight Bi atoms, as denoted by a green circle in (a). Red and blue colors denote the phases of wave functions of 0 and π, respectively. Here, only Bi $6p_x$ orbitals are illustrated without loss of generality.

#8, 9 (bonding states) and #10, 11 (anti-bonding states) at the Γ and Z points, respectively. Here, a ribbon-like shape represents the spreading of the Bi $6p_x$ orbital, and red and blue colors represent the phases of the Bloch function of 0 and π. Without loss of generality, only Bi $6p_x$ orbitals are illustrated on the corners of the square prism of eight Bi atoms represented in Fig. 5.9(a). The more same-colored orbitals overlap, the lower the energy level is located. This indicates that the bonding state (E_u) at the Z point [Fig. 5.9(e)] has the lowest energy among them in Figs. 5.9(a)-(d). Likewise, the anti-bonding state (E_g) [Fig. 5.9(d)] at the Z point has the highest energy. Thus, the energy difference of the anti-bonding and bonding states becomes minimum at the Brillouin zone center.

As a result, the energy-level difference between E_g and E_u at the Γ point (Z point) is smaller (larger) than the band modification induced by the SOI of the Bi atom ($\sim$ 1 eV); thus a topologically non-trivial electronic structure similar to the strong three-dimensional topological insulator is achieved in β-$PdBi_2$. We should note that, if the energy level of the Bi $6p_z$ anti-bonding state were far from that of the Bi $\{6p_x, 6p_y\}$ bonding state, the band inversion between $E_{1/2u}$ and $E_{1/2g}$ (#8 and #9 at the Γ point) could not occur. For the Bi $6p_z$ orbitals, the largest energy difference between the bonding and anti-bonding state at the Γ point is understood in the same manner as for the Bi $\{6p_x, 6p_y\}$ orbitals.

5.8.2 Parity inversion for gap 7-6

For gap 7-6 where the surface Dirac cone lies, the parity inversion is realized already in the non-relativistic case as shown in Fig. 5.5(c), in contrast to gap 9-8. Figures 5.10(a) and (b) schematically show the energy levels of Bi $6p_z$ and Pd $4d_{z^2}$ orbitals contributing to the parity inversion at the Z and Γ points without SOI. For the Bi $6p_z$ anti-bonding and bonding states, those energy levels are close (far) at the Z point (Γ point), as understood in the same manner as in the case of the $\{6p_x, 6p_y\}$ states shown in Fig. 5.9. At the Γ point, the band inversion between the A_{1g} and A_{2u} states is introduced by the mixing of Bi $6p_z$ and Pd $4d_{z^2}$ because the Bi $6p_z$ bonding state has the same symmetry as in the Pd $4d_{z^2}$ orbital represented by A_{1g}, forming two A_{1g} states as shown in Fig. 5.10(c). On the other hand, the Bi $6p_z$ anti-bonding state with odd parity cannot mix with the Pd $4d$ orbitals with even parity. Consequently, the Bi $6p_z$ bonding state energetically overcomes the Bi $6p_z$ anti-bonding state with the help of the Pd $4d_{z^2}$ orbital only at the Γ point, leading to the topologically non-trivial electronic structure in the absence of SOI.

Furthermore, the energy levels of the A_{1g} and A_{2u} state at the Z point, as shown in Figs. 5.5(a) and (b) and denoted by green rectangles, are nearly unchanged by SOI. This suggests that those electrons cannot rotate around atoms but stretch straight forward owing to the lack of the transverse component of orbital angular momentum (*i.e.* p_z and d_{z^2} orbitals; $l_z = 0$). However, as mentioned at the beginning of this section, SOI should still play an essential role in the anti-crossing gap around the Z point and in providing the spin polarization on the Dirac

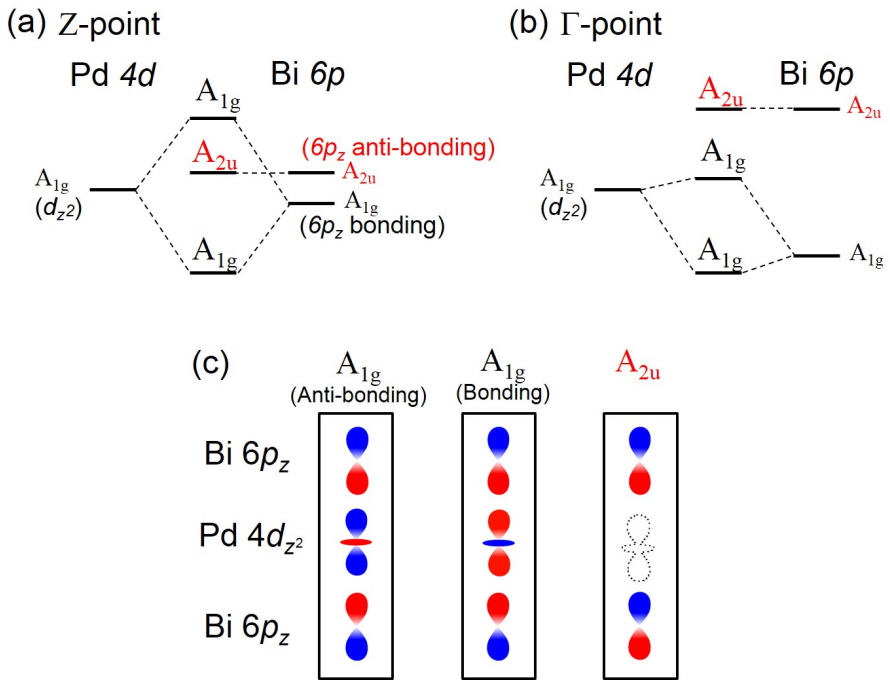

Figure 5.10: (a), (b) Schematics of the energy levels consisting of Bi $6p_z$ and Pd $4d_{z^2}$ orbitals contributing to the parity-inverted band structure in gap 7-6 realized in the absence of SOI at the Γ and Z points. Energy levels having odd parity is denoted by red. (c) Schematic of the molecular orbitals of two A_{1g} (anti-bonding and bonding) states and A_{2u} state consisting of the Bi $6p_z$ and Pd $4d_{z^2}$ orbitals at the Γ and Z points. The A_{2u} state having odd parity cannot mix with the Pd $4d$ orbitals having even parity at the Γ and Z points represented by a contour shaped as a $4d_{z^2}$ orbital indicated by a broken line.

cone band dispersions, as shown in the green rectangle in Fig. 5.5(b).

It is worth noting that the anti-bonding and bonding states are helpful for the parity inversion in the case of both gap 9-8 and gap 7-6 because two Bi atoms in a body-centered tetragonal unit cell form a small energy difference between two eigenstates having odd and even parity. Such materials including several atoms in a unit cell can be candidates for not only topological insulators but also other topological materials.

5.9 Summary

We have investigated the electronic structure in the normal state of a centrosymmetric superconductor β-$PdBi_2$ by using ARPES and spin-resolved ARPES. In addiction to the spin-degenerate bulk bands, several surface band dispersions (surface Dirac cone, S1, and S2) with in-plane spin polarizations are additionally observed. Those bulk and surface band dispersions are in good agreement with the calculated band dispersions obtained by first-principles band calculations for bulk bands and the slab calculation for surface states. Since the slab calculations do not account for any surface reconstruction and relaxations of atoms, the surface Dirac cone band dispersion with spin polarization evokes that of topological insulators.

To discuss the topological nature of bulk band dispersions, we have evaluated the Z_2 invariant derivation in analogy to three dimensional strong topological insulators. In the centrosymmetric tetragonal body-centered crystal structure β-$PdBi_2$, the parity eigenvalues at Γ and Z points dominate the Z_2 topological invariant $\nu_0(N)$, where N is the band index. The parity analysis reveals that the surface Dirac cone [$\nu_0(6) = 1$, lying in defined gap 7-6] and the S2 [$\nu_0(8) = 1$, lying in defined gap 9-8 across the Fermi level] are topologically protected surface states.

The parity inversions of gap 7-6 and gap 9-8 have different origins. For gap 7-6, $\nu_0(6) = 1$ is realized already in the non-relativistic band dispersions. It is derived from the band inversions between A_{1g} and A_{2u} bands introduced by the Bi $6p$ and Pd $4d$ mixing. In that case, the spin-orbit interaction does not modify the energy levels of related band dispersions at the Z point, but it still plays an essential role in gap-opening around the Z point and in providing the spin polarizations for the surface states. For gap 9-8, the strong spin-orbit interaction of Bi $6p_x$, $6p_y$ orbitals realize the parity inversion at the Γ point above the Fermi level. The $\{6p_x, 6p_y\}$ anti-bonding (E_g) and bonding (E_u) states derived from the two Bi atoms in a unit cell provide a good condition for the parity-inverted topologically nontrivial band structure.

To search for new topological materials such as Dirac/Weyl semimetals and topological superconductors, it is useful to pay attention to materials not only including heavy atoms with strong spin-orbit interaction but also including two or more of the same atoms in a unit cell. For example, in analogy with β-$PdBi_2$, there would be many uninvestigated materials in which

a superconducting state and topological surface states coexist without any chemical doping at ambient pressure. For the β-$PdBi_2$, the next step should be the direct elucidation of the superconducting state. There may be a chance to observe non-trivial superconducting excitations, in which Majorana fermions emerge as theoretically suggested [182–185].

Chapter 6

Topological surface states on polar semimetal $MoTe_2$

6.1 Introduction: Weyl semimetal with time-reversal symmetry

The Weyl semimetal is one of the topological materials [76], in which pairs of crossed linear band dispersions (Weyl cones) located off the high symmetrical line in momentum space form a gapless bulk band structure. The effective Hamiltonian for the band crossings obeys the Weyl equation [186] referred to in particle physics that approximately describes the chiral and massless behavior of neutrinos. In solids, the Weyl cones always appear in pairs, and those band crossing points (Weyl nodes) act as a source or sink of Berry curvature [137, 187] in momentum space. This peculiar bulk electronic structure in the Weyl semimetal exhibits exotic transport phenomena such as the chiral anomaly [188–192]. Those Weyl nodes are not protected by any symmetries, but their existence somewhere in the Brillouin zone is topologically guaranteed. The topologically protected appearance of accidental band degeneracies can be realized in the time reversal symmetry broken system [76, 78] or the space inversion symmetry broken system [77]. Topological surface states accompanied by this topological nature are characterized as arc-like unclosed Fermi surfaces (called Fermi arcs) connecting two Weyl nodes with opposite chiralities. Recently, on the magnetic compound $YbMn_2Bi_2$ [79] and the noncentrosymmetric compounds TaAs and related materials [80–85], Fermi arcs have been clearly observed by using angle-resolved photoesmission spectroscopy (ARPES), providing the first evidences of the Weyl semimetallic

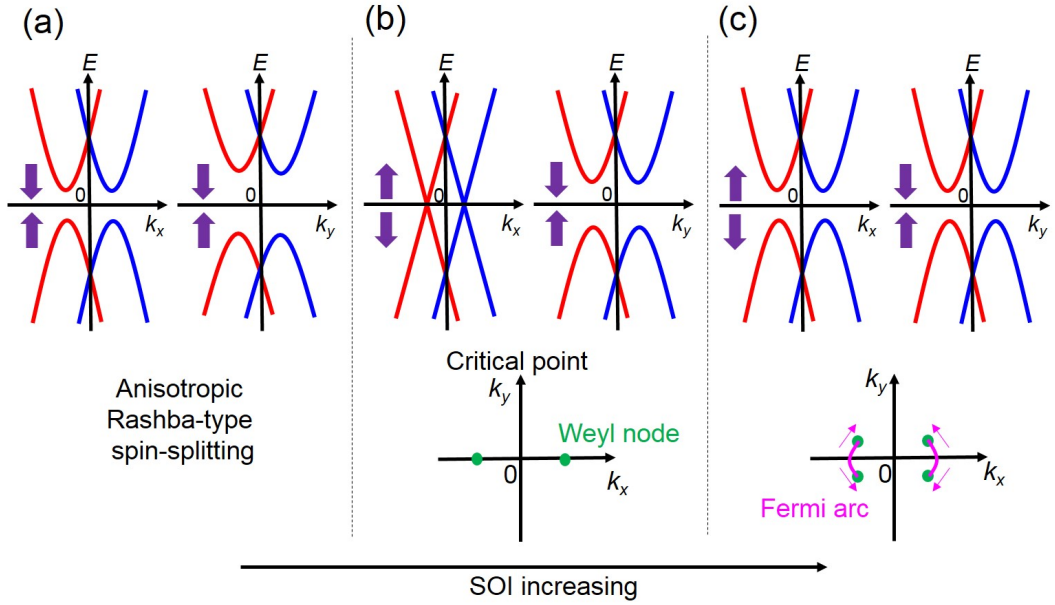

Figure 6.1: Schematics of the phase transition from the normal insulator (a) to the Weyl semimetal (b),(c) in three dimensions. Here, the anisotropic Rashba-type spin-split band dispersions (red and blue lines) both above and below the Fermi level are assumed, given the SOI increasing as a parameter from (a) to (c). Purple arrows indicate the gap closing or opening. The Fermi surface with moving Weyl nodes (green points) and evolving Fermi arcs (pink lines) are shown in the lower panels.

electronic structure realized in real materials.

The Weyl semimetal phase in three dimensions with space inversion symmetry universally exists in the phase transition from a normal insulator into a topological insulator [77]. Tracking the evolution of the Fermi arcs in the phase transition [77, 193–195] is helpful to understand the electronic structure of the Weyl semimetal and the role of spin-orbit interaction (SOI) in it. In Figs. 6.1(a)-(c), the phase transition from the normal insulator (a) to the Weyl semimetal (b), (c) on anisotropic Rashba-type spin-splitting in bulk is schematically shown, given the SOI increasing from (a) to (c). In the first step in Fig. 6.1(a), we assume a gap along the k_x direction narrower than that along the k_y direction owing to the difference of the spin-splitting. With increasing SOI (i.e., energies of spin-splittings), the gap closes on the k_y-axis, and Weyl nodes

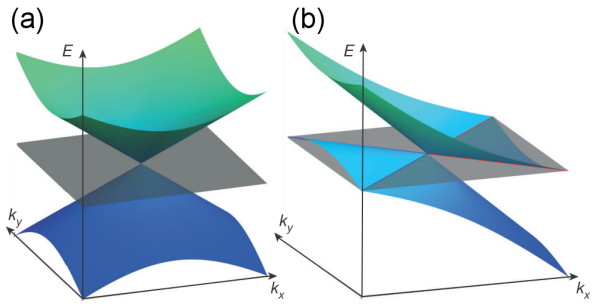

Figure 6.2: Schematics of a Type-I Weyl node with a point-like Fermi surface (a) and a type-II Weyl node appearing as the contact point between electron and hole pockets (b). These graphs are adopted from ref. [196].

(denoted by green markers in the lower panel) are formed at the critical point in Fig. 6.1(b). When the SOI increases further, the energy gap is opening on the k_y-axis; in contrast, it is still closing on the k_x-axis. Furthermore, the generated Weyl nodes are traveling toward the k_y axis as represented by pink arrows in Fig. 6.1(c). This situation indicates that the Weyl cones must exist between the k_x-axis and k_y-axis, accompanied by the Fermi arcs (denoted by pink lines in the lower panel). The Weyl semimetallic electronic structure is translated as partly band-inverted band dispersions in momentum space. Finally, after the Weyl nodes touch the k_y-axis, the system changes into the topological insulator phase in the space inversion symmetry broken system. As seen above, the spin-split band dispersions derived from the SOI play essential roles in the Weyl semimetal phase, and such a situation is realized in pressured BiTeI [193, 194] with the giant Rashba-type spin-splitting, as shown in section 1.3.1.

Very recently, Soluyanov *et al.* theoretically proposed another type of Weyl semimetal called type-II Weyl semimetal [196], in which Weyl nodes appear as the contact point between electron and hole pockets, as shown in Fig. 6.2(b), and its physcal properties are different from those of normal (type-I) Weyl semimetals with the point-like Fermi surface in Fig. 6.2(a). The type-II Weyl node corresponds to sufficiently tilted type-I Weyl nodes [196]. One of the candidates for type-II Weyl semimetal is the polar semimetal MTe_2 (M = Mo, W) [196–203, 210] consisting of electron- and hole-like Fermi surfaces. In this chapter, we investigate the electronic struc-

ture of the polar semimetal $MoTe_2$, which is theoretically proposed to have Weyl nodes in the unoccupied band structure [200, 201].

6.2 Experimental setup and calculation condition

Single-crystalline samples grown by the chemical vapor transport method were provided by Mr. Ikeura (Ishiwata group, Department of Applied Physics, The University of Tokyo).

ARPES measurement with an *s*-polarized laser light source (6.43 eV) at 25 K was performed at the Department of Applied Physics, The University of Tokyo (as discussed in Chapter .3), using an R4000 hemispherical electron analyzer (VG Scienta). The total energy resolution was set to 1 meV. Samples were cleaved in situ at 25 K. ARPES measurement with an *s*-polarized laser light source (6.994 eV) at 25 K and 100 K was performed at Shin group, ISSP, The University of Tokyo, using an DA30 hemispherical electron analyzer (VG Scienta). The total energy resolution was set to 7 meV to prioritize the photoemission intensity. Samples were cleaved in situ at 25 K.

Electronic structure calculations were performed by Dr. M. S. Bahramy (Department of Applied Physics, The University of Tokyo) within the context of density functional theory (DFT) using the Perdew-Burke-Ernzerhof correlation functional as implemented in the VASP program [204]. Relativistic effects, including spinorbit coupling, were fully included. The Brillouin zone was sampled by a $20 \times 10 \times 5$ k-mesh. For the orbital and layer projection calculation, a tight binding Hamiltonian for the bulk band structure was constructed by downfolding the DFT results using maximally localized Wannier functions [205], employing Mo $4d$ and $4s$ orbitals and S $3p$ and $3s$ orbitals as a basis.

6.3 Crystal structure and electronic structure

The layered transition metal dichalcogenide $MoTe_2$ shows a structural transition at $T_C = 240$ K from the high-temperature monoclinic phase [Fig. 6.3(a)] to low-temperature orthorhombic phase[Fig. 6.3(b)] [206–209]. The crystal structure of the high-temperature phase has space inversion symmetry (space group $P2_1/m$), while that of the low-temperature phase lacks an

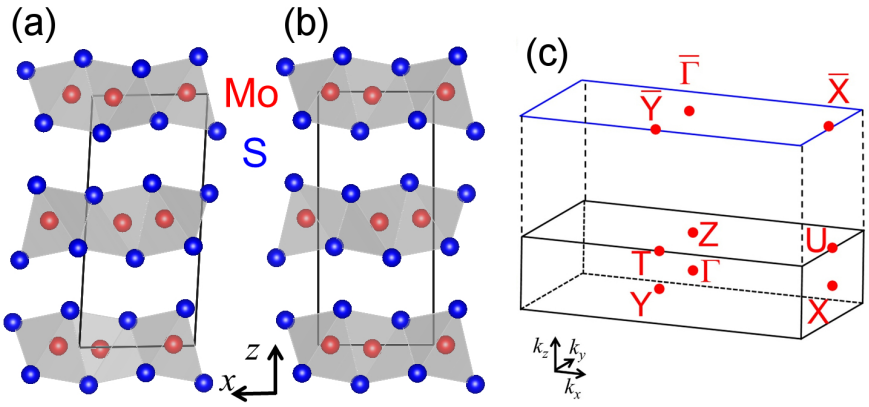

Figure 6.3: (a)(b) Crystal structures of high-temperature monoclinic phase (space group P2$_1$/m) and low-temperature orthorhombic (Pnm2$_1$) phase. (c)Brillouin zone of the orthorhombic crystal structure. Γ, Z, X, U, Y, and T are the high-symmetry points. The blue rectangle represents the projected two-dimensional Brillouin zone with the two-dimensional high-symmetry points ($\bar{\Gamma}$, $\bar{\mathrm{X}}$, and $\bar{\mathrm{Y}}$).

inversion center (Pnm2$_1$). The lattice constants for the low-temperature phase are $a = 3.477$ Å, $b = 6.335$ Å, and $c = 13.883$ Å, which are obtained by an X-ray diffraction study at 120 K [200]. The strong atomic SOIs of Te $5p$ and Mo $4d$ orbitals greater than 0.1 eV leads to Rashba-type spin-split band dispersions in the polar crystal structure of orthorhombic MoTe$_2$. These satisfy the necessary conditions to realize the Weyl semimetallic electronic structure.

The Fermi surfaces of orthorhombic MoTe$_2$ consist of electron-like and hole-like surfaces [200, 201, 210]. The surface electronic structure obtained by the band calculation is shown in Fig. 6.4, which is adopted from ref. [200]. The corresponding two dimensionally projected Brillouin zone is shown in Fig. 6.3(c) (blue rectangle) with the orthogonal momentum axes k_x, k_y, and k_z. The hatched area represents the two-dimensionally projected bulk electronic structure, and sharp linear contours and band dispersions correspond to surface states which can be merged into bulk band dispersions. Figure 6.4(i) shows the electron-like and hole-like band dispersions along $\bar{\mathrm{Y}} - \bar{\Gamma} - \bar{\mathrm{X}}$. The hole-like surfaces around the $\bar{\Gamma}$ point (electron surfaces) becomes smaller (bigger) with increasing energy, as shown in the electronic structure at constant energies of $E_\mathrm{F} + 6$ meV in Fig. 6.4(a) and at $E_\mathrm{F} + 59$ meV in Fig. 6.4(b). In the type-II Weyl

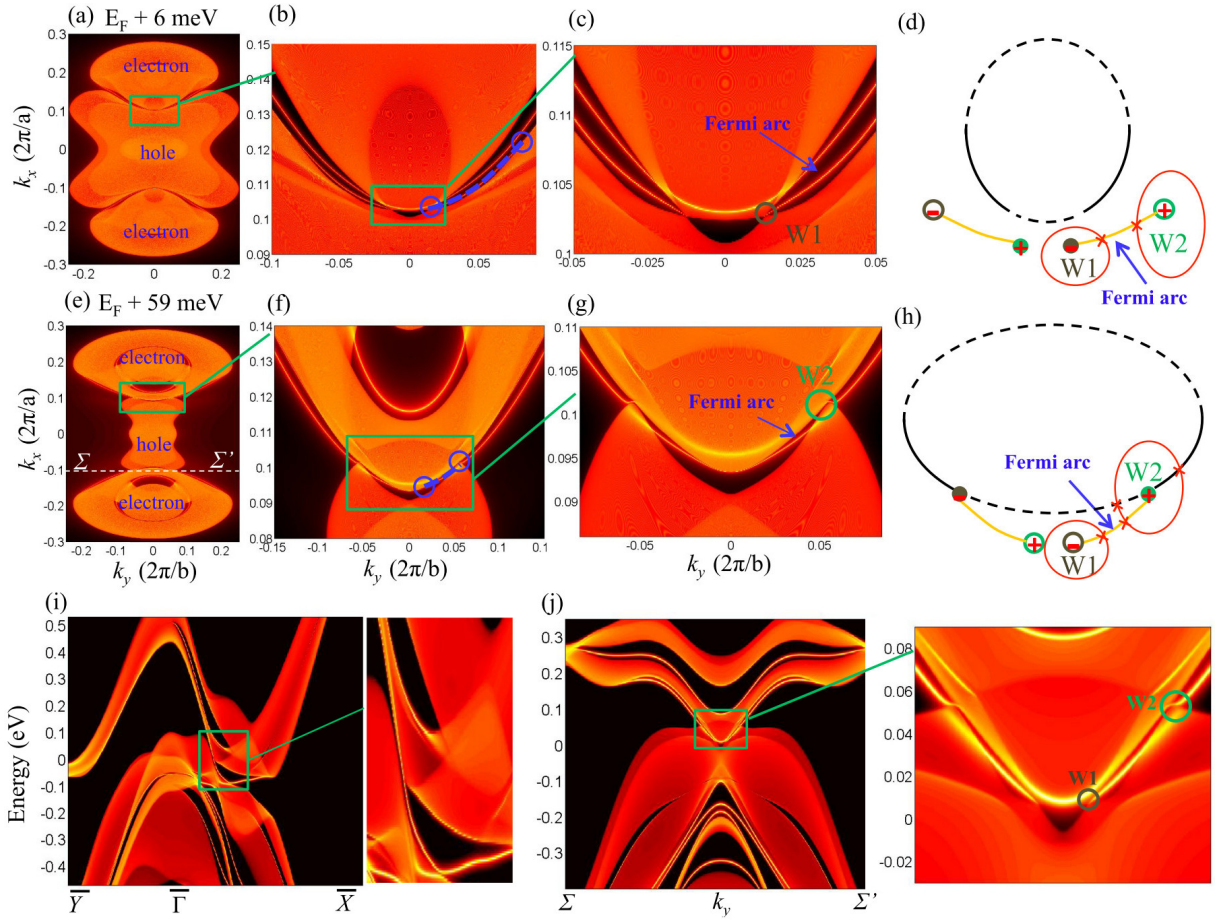

Figure 6.4: (a)-(c) Calculated constant-energy surface at E_F +6 meV where the Weyl nodes (W1) are located. (d) Schematic illustration of Fermi arc at E_F +6 meV. (e)-(g) Calculated constant energy surface at E_F +59 meV where the Weyl nodes (W2) are located. (h) Schematic illustration of Fermi arc at E_F +59 meV. (i) Surface energy dispersion along the high symmetry lines of $\bar{Y}$-$\bar{\Gamma}$-$\bar{X}$. (j) Surface energy dispersion along the Σ-Σ' crossing Weyl nodes. The exact projections of W1 and W2 are denoted as solid gray and green dots. The end points of Fermi arcs are marked as open circles. The Fermi arcs are highlighted by dashed lines in (b) and (f). All images are adopted from ref. [200].

semimetal, Weyl nodes accompanying Fermi arcs appear at the boundary of the electron and hole pockets [196]. The calculated results show the two different kinds of Weyl nodes (W1 and W2) located at different energies of E_F+6 meV and E_F+59 meV. The Fermi arcs connecting

W1 and W2 are clearly seen in the close-up view of Figs. 6.4(b),(c),(f), and (g), and they are schematically summarized in Figs. 6.4(d) and (h). Since the line connecting W1-W2 is almost parallel to the k_y axis, Fig. 6.4(j) presents the Fermi arc surface states along the Σ-Σ' crossing W1 and W2, as denoted in Fig. 6.4(e). Meanwhile, another recent first-principles calculation study on $MoTe_2$ with the lattice parameter experimentally obtained at 100 K [201] suggests only four Weyl nodes of W2. This implies that the band dispersions are very sensitive to the small difference of the lattice parameters [200, 201] and/or the precise treatment of the band calculations. In addiction to the Fermi arcs, several surface states, which do not reflect the Weyl smimetallic electronic structure but possibly some kind of topological electronic structure, are observed at the boundary of the electron and hole pockets. For example, we find a characteristic surface state connecting the bottom of electron pocket and hole bands along $\bar{\Gamma}$-$\bar{\mathrm{X}}$, as shown in the lower part in the close-up view of Fig. 6.4(i). Here, we should recollect that the Fermi arc appears only between the Weyl nodes with opposite chiralities and connects them.

6.4 Different surface states depending on surface terminations

To investigate the electronic structure near the Fermi level precisely, we carried out the laser ARPES measurement on orthorhombic $MoTe_2$ at $T = 25$ K. At a cleavage surface, two different kinds of ARPES images along $\bar{\Gamma}$-$\bar{\mathrm{X}}$ are obtained, as shown in Figs. 6.5(a) and (b). Though the obtained laser ARPES images are very complicated, we can see hole-like electronic states around the Brillouin zone center and electron-like states located at $k_x < -0.2$ Å^{-1} both in Figs. 6.5(a) and (b), similar to the results of the previous first-principles calculation study [200, 201]. By comparing two ARPES images, one of the contrasting differences is the sharp intensities denoted by pink arrows. Those band dispersions likely correspond to surface states connecting the electron and hole pockets, as discussed in the previous section. Taking note of the difference between these ARPES intensities, the surface state observed in Fig. 6.5(a) disperses at a shallower energy relative to the Fermi level than that in Fig. 6.5(b), in contrast to the bulk electron pockets located at the same energy and indicated by yellow broken lines in Figs. 6.5(a) and (b). In addition, a characteristic band-repulsion-like behavior indicated by a purple arrow is only

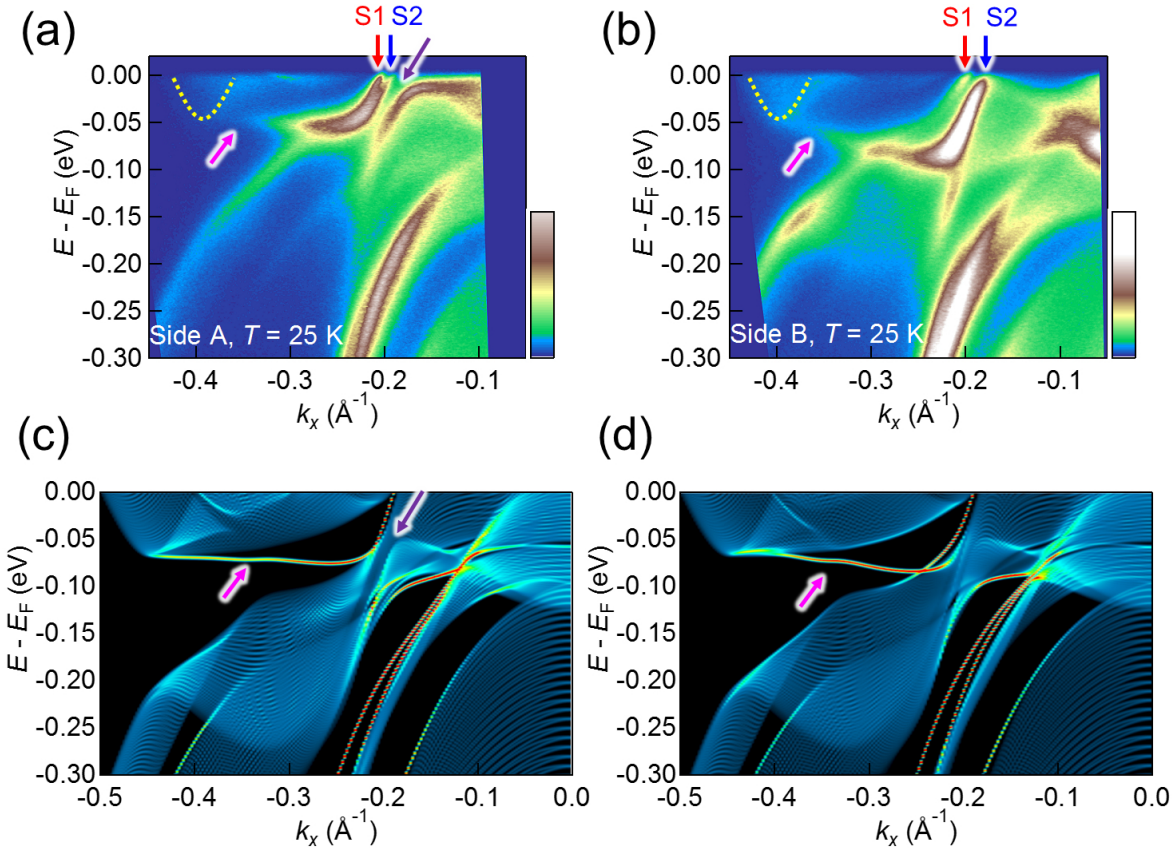

Figure 6.5: (a), (b) Laser ARPES images along the k_x direction on the side A and B. The yellow broken line indicates the electron pocket across E_{F}. S1 and S2 are surface states lying at the boundary between the electron pocket and the hole pocket. (c), (d) Surface electronic structure on side A (00-1) and side B (001) surfaces obtained by the slab calculation. Hatched areas correspond to the bulk band dispersions projected onto the $\bar{\Gamma}$-$\bar{\mathrm{X}}$ line.

observed in Fig. 6.5(a). To clarify the origin of the two different ARPES images, we calculate surface electronic structures on (00-1) and (001) surfaces as shown in Figs 6.5(c) and (d). The calculated results reproduce well the difference of the surface band dispersions (represented by pink arrows), and the repulsive behavior (represented by purple arrows) depending on the surface terminations. This suggests that the different surface-termination domains (larger than the laser spot size of ~ 0.1 mm) mix on a cleavage surface reflecting the bulk polar crystal structure.

Hereafter, we define the (00-1) surface as side A [Figs. 6.5(a),(c)] and the (001) surface as side B [Figs. 6.5(a),(c)]. Judging from the behavior of the surface state, the previous studies [200, 201] correspond to those on side B.

The calculation results on side B in Fig. 6.5(c) correspond to previous band-calculation results [200,201]. On side B, as suggested in the previous theoretical study [200,201], two surfaces states lying at the boundary between the hole and electron pockets are observed (denoted by S1 and S2) in Fig. 6.5(b), and the S2 surface state corresponds to the bulk merged surface states forming the Fermi arc off the k_x axis. Similar ARPES intensities as denoted by S1 and S2 are also observed on side A in Fig. 6.5(a), and the S2 surface state seems to be merged into the bulk band dispersions in the calculated result in Fig. 6.5(c) as well. We note that the observed energy difference of the surface states between sides A and B is larger than the calculated results. It likely depends on realistic surface conditions (e.g. atomic relaxations and/or surface reconstructions) omitted in calculation. Comparing between calculation and experimental results, the observed bulk electron pockets in both Figs. 6.5(a) and (b) are located at slightly lower energy (~ 0.02 eV) compared to calculated ones in Figs. 6.5(c) and (d) because of the non-stoichiometry.

6.5 Fermi arc like surface states

Now, we focus on constant-energy ARPES intensity mappings on respective surfaces to detect signatures of the Fermi arcs in Weyl semimetallic electronic structures. Figures 6.6(a) and (d) show the constant energy ARPES intensity mappings at the Fermi level ($E = E_{\mathrm{F}}$) on side A and B, respectively. At the Fermi level, the electron pocket [denoted by circle with yellow broken line in Fig. 6.6(a)] and a part of the hole pockets around the $\bar{\Gamma}$ point forming the semimetallic Fermi surfaces are clearly observed. The sharp intensities lying at the boundary of the electron and hole pockets represent the surface states S1 and S2 denoted by red and blue arrows, respectively. As discussed in the previous section, the S2 surface state on side B is merged into the bulk band dispersions on the k_x axis. Similarly, the observed contour of S2 at the Fermi level on side B in Fig. 6.6(d) shows a characteristic intensity contrast between on and off the k_x axis. This

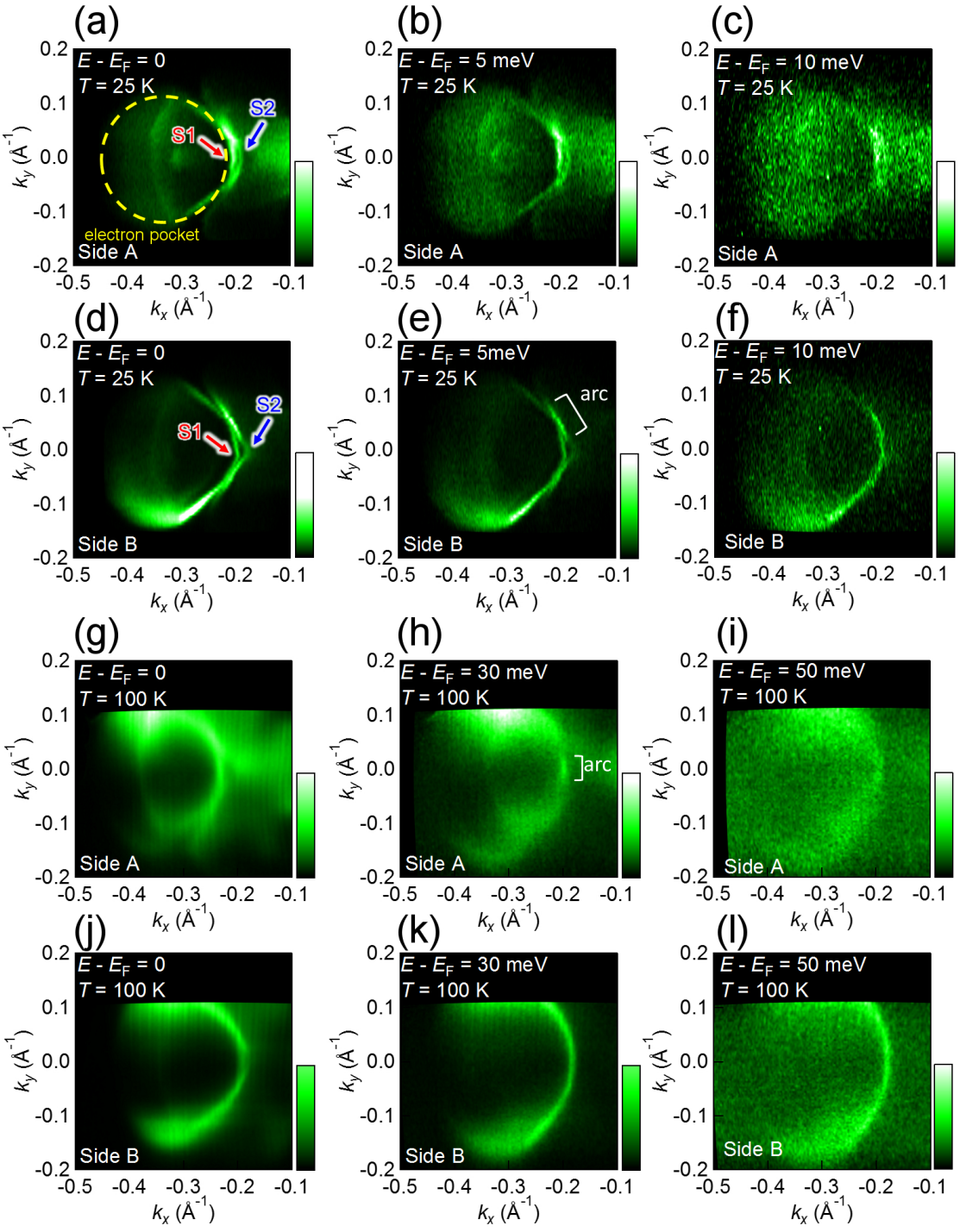

Figure 6.6: (a)-(c) Constant-energy ARPES intensity mapping on side A at $T = 25$ K for $E = E_F$, E_F+5, and E_F+10 meV. (d)-(f) That on side B at $T = 25$ K for $E = E_F$, E_F +5, and E_F+10 meV. (g)-(i) That on side A at $T = 100$ K for $E = E_F$, E_F +30, and E_F+50 meV. (j)-(l) That on side B at $T = 100$ K for $E = E_F$ and E_F +30, and E_F+50 meV.

intensity contrast becomes drastic at $E - E_F = 5$ meV in Fig. 6.6(e), and the ARPES intensity is almost invisible on the k_x axis, resulting in arc-like segments remaining off the k_x axis. This characteristic behavior is not seen at $E - E_F = 10$ meV in Fig. 6.6(f). These arc-type surface states agree well with the calculated topological Fermi arcs connecting W1 and W2 Weyl nodes in Fig. 6.4 [200].

In contrast to side B, such an intensity contrast is not seen in the intensity mapping on side A at $E - E_F = 0$ (Fermi level), 5, and 10 meV in Fig. 6.6(a)-(c); both the S1 and S2 surface states appear to be continuous even on the k_x axis. To search for the Fermi arc on side A, we performed laser ARPES measurement at $T = 100$ K, which enables us to obtain the ARPES intensity of unoccupied bands owing to the thermal excitation. Figures 6.6(g)-(i) show the ARPES intensity mappings at $E - E_F = 0$ (Fermi level), 5, and 10 meV on side A at $T = 100$ K with the independently defined color scale for respective images. Though those ARPES images are indistinct compared with those taken at $T = 25$ K, an arc-like segment of ARPES intensities on the k_x axis is certainly observed only at $E - E_F = 30$ meV. Such Fermi-arc-like segment is not observed on side B at $T = 100$ K, as shown in Figs. 6.6(j)-(k). The shape of the observed arc-like intensity segment in Fig. 6.5(h) appears to compensate for the intensity lacking observed in Fig. 6.5(e); that is, it seems to connect the W1 Weyl nodes across the $k_y = 0$ momentum cut.

To confirm the surface band dispersions forming the Fermi arcs on side A, we present ARPES images ($E - E_F$ vs. k_x) along momentum cuts ♯1 - ♯3 ($k_y = 0, 0.15$ and 0.30 Å^{-1}) [Figs. 6.7(b)-(d)], as indicated on the constant energy intensity mapping in Fig. 6.7(a). In order to observe the unoccupied electronic structure clearly, these ARPES images are divided by the Fermi-Dirac distribution function convolved by Gauss function with FWHM = 7 meV along the energy direction. As clearly shown in Figs. 6.7(a)-(c), the sharp intensity across $E = E_F$ +30 meV is suppressed at $k_y = 0.30$ Å $^{-1}$ (off the Fermi-arc) as represented by orange broken lines in Figs. 6.7(a)-(c), respectively. This represents the characteristic behavior of the topological surface states in the Weyl semimetal phase, connecting the W1 Weyl nodes across the k_x axis. As might be expected, contrasting behaviors are observed on side B. ARPES images in Figs. 6.7(f)-(h) are obtained in the same manner as side A in Figs. 6.7(b)-(d), except that a Gauss

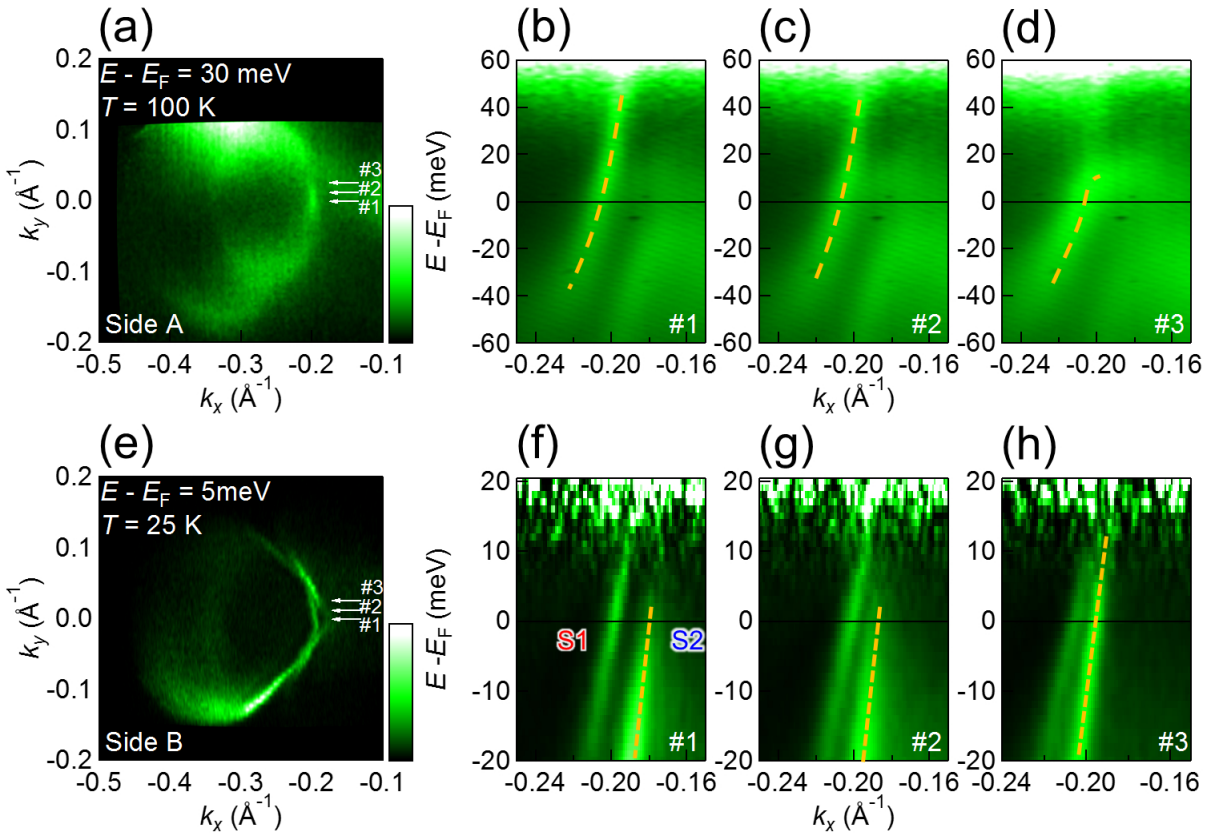

Figure 6.7: (a) The ARPES intensity mapping at $E = E_{\rm F}$ +30 meV on side A. (b)-(d) ARPES images divided by the Fermi-Dirac distribution function convolved by a Gauss function with FWHM = 7 meV along momentum cut ♯1 - ♯3 ($k_y = 0, 0.15$ and 0.30 Å^{-1}) as indicated in (a). (e) The ARPES intensity mapping at $E = E_{\rm F}$ +5 meV on side B. (b)-(d) ARPES images divided by the Fermi-Dirac distribution function convolved by a Gauss function with FWHM = 1 meV along momentum cut ♯1 - ♯3 ($k_y = 0, 0.15$ and 0.30 Å^{-1}), as indicated in (e). Off the Fermi arcs [(d) on side A, (f) and (g) on side B], the surface states are merged into bulk band dispersions as represented by orange broken lines in (a)-(h).

function with FWHM = 1 meV was used. Corresponding momentum cuts are denoted on the constant-energy intensity mapping in Fig. 6.7(e). The momentum cut ♯1 ($k_y = 0.30$ Å $^{-1}$) on the Fermi arc in Fig. 6.7(h) shows the sharp intensities of S1 and S2 lasting to the unoccupied side. Contrastingly, on cuts ♯1 and ♯2 in Figs. 6.7(f) and (g), the S2 intensities are suddenly suppressed above the Fermi-level. These intensities form the separated surface states across the

k_x axis connecting the W1 and W2 Weyl nodes.

6.6 Discussion: Fermi arcs on side A and B

Laser ARPES results show the signature of Fermi arcs both on side A and B, reflecting the type-II Weyl semimetal electronic structure in orthorhombic $MoTe_2$. Experimentally, the W1 Weyl nodes are located at different energies between side A ($E - E_F \sim 5$ meV) and side B ($E - E_F \sim 5$ meV). In addition, the connectivity of the Fermi arcs also depends on the surface terminations: W1-W1 on side A and W1-W2 on side B. In this section, we discuss the calculated Fermi arcs on side A and B and compare them with the experimental results.

In principle, the Weyl nodes should be located at the same energy on both side A and B because they reflect the accidental band degeneracy points in bulk band dispersions. The calculated results should accord with this principle taken for granted, unless different atomic configurations in bulk are used. Figures 6.8(a) and (b) [(c) and (d)] show calculated surface electronic structures around the boundary of the electron and hole pockets on side A and B at the constant energy $E = E_F$ +7 meV [$E = E_F$ +57 meV], where the W1 [W2] Weyl nodes represented by a blue (green) open circle are located. For side B, the obtained electronic structure hosting the W1 and W2 Weyl nodes is quantitatively similar to that of obtained with the previous study in ref. [200]. The accompanied Fermi arcs connecting W1 and W2 (represented by yellow arrows) and additional surface states (represented by light blue arrows) are clearly reproduced. On the other hand, a remarkably different surface electronic structure is obtained on side A in Fig. 6.8(a). We can find the Fermi arc connecting W1 Weyl nodes across the k_x axis on side A (represented by a yellow arrow), which are very similar to that experimentally observed in Fig. 6.6(h). On examining the calculated surface band dispersions along the k_y direction at $k_x = -0.186$ Å^{-1} in Figs. 6.8(e) and (f), where the W1 Weyl nodes are located, the different connectivities on the Fermi arcs (represented by yellow arrows) on side A (W1-W1) and B (W2-W2) are clearly comprehensible.

These calculated results strongly suggest that the experimentally observed connectivity changing of the Fermi arcs between side A and B in Figs. 6.6(h) and (e) are derived from

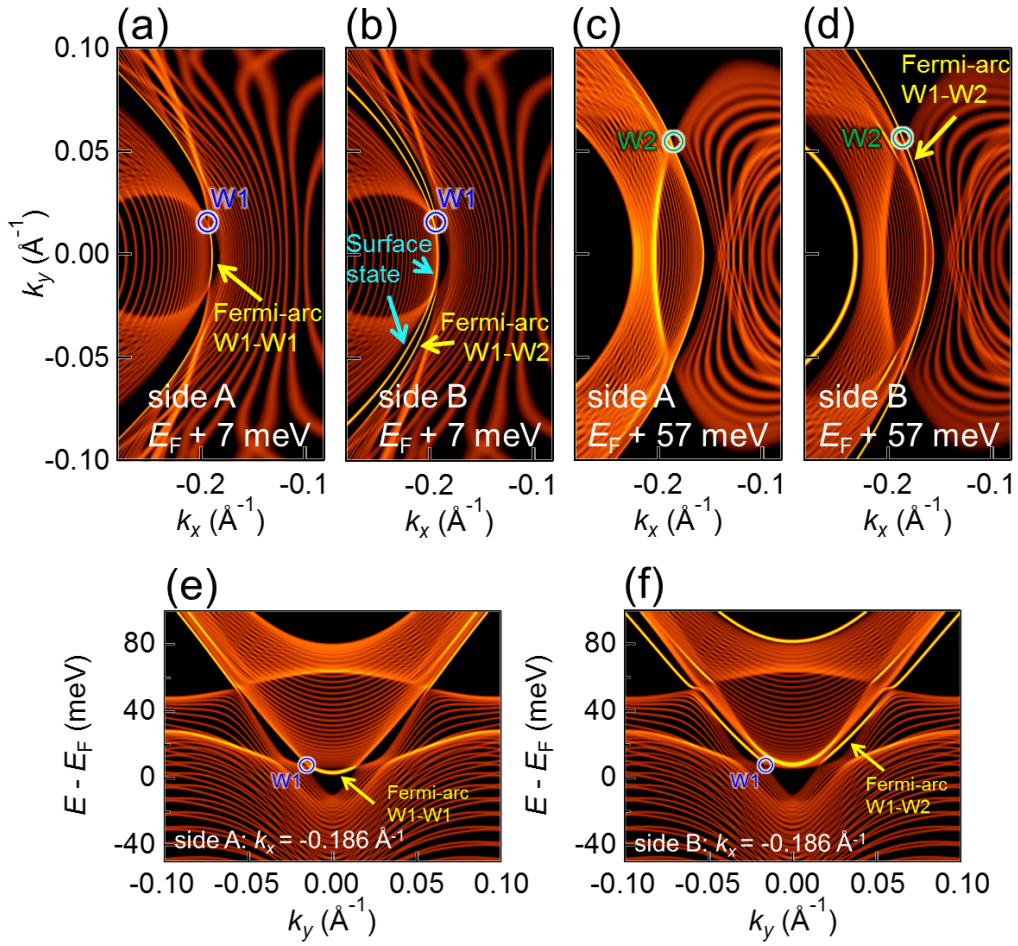

Figure 6.8: (a), (b) Calculated surface electronic structures on side A [(00-1) surface] and B [(001) surface] at the constant energy $E = E_{\mathrm{F}}$ +7 meV where the W1 Weyl nodes (one of them denoted by a blue open circle) are located. (c), (d) Calculated surface electronic structures on side A and B at the constant energy $E = E_{\mathrm{F}}$ +57 meV where the W2 Weyl nodes (one of them denoted by a blue open circle) are located. (e), (f) Calculated surface band dispersions on side A and B along the k_y direction at $k_x = -0.186$ Å^{-1}, where the W1 Weyl nodes are located.

the surface termination dependence, and also provide the clear evidence of the Weyl semimetal phase realized in orthorhombic $MoTe_2$. The experimentally obtained energy-level difference of the W1 Weyl nodes between side A and B possibly originates from the realistic atomic configuration near the surface (i.e. atomic relaxations and/or reconstructions). It is not unrelated to

the fact that the W1 Weyl nodes are very sensitive to the lattice parameter, as discussed in the band calculation studies [200, 201]. For the connectivity changing of the Fermi arcs depending on surface terminations, a similar behavior is observed in the calculated results for TaAs [211], which are not experimentally confirmed yet. In the case of $Mo_xW_{1-x}Te_2$, it is theoretically proposed that the connectivity depends on the surface potential energy [202]. In order for seides A and B to share the same topology of the electronic structure in orthorhombic $MoTe_2$, an additional Fermi arc is required (e.g. a Fermi arc connecting W2-W2 on side A). We note that the Fermi arcs in type II Weyl semimetal can be hidden within the projection of the bulk band dispersions [196]. To identify the whole band topology on both side A and B experimentally, further experimental investigations should be carried out on an electron-doped and/or alkali-atoms evaporated $MoTe_2$ to enable a precise ARPES measurement while maintaining a low temperature; the realistic atomic considerations near the surfaces should be carefully accounted for.

6.7 Summary

We have investigated the electronic structure of the polar semimetal orthorhombic $MoTe_2$, which is one of the candidates of the type-II Weyl semimetal, by using laser ARPES. At a cleavage surface, two types of ARPES images are obtained. Since the only surface states disperse differently from bulk band dispersions, these different ARPES images are supposed to be derived from the different surface terminations reflecting the polar crystal structure. These ARPES images are in good agreement with the surface electronic structures calculated on a different terminated surface. We classify the ARPES images as the electronic structures on the side A [00-1 surface] and B [001 surface], respectively, and the results for side B agree well with the previous first-principles calculation study [200, 201]. The ARPES intensity mapping on side B is also in agreement with the previous study, and the Fermi arcs connecting the Weyl nodes W1 and W2 are clearly observed at $E - E_F \sim 5$ meV. In contrast, the ARPES intensity mapping on side A taken at $T = 100$ K shows a Fermi arc connecting the W1 Weyl nodes across the k_x axis locating at $E - E_F \sim 30$ meV. The calculated results reproduce this connectivity

changing of the Fermi arcs in agreement with the experiment, though the energy difference of the W1 Weyl nodes on side A and B are not taken into account. Our study has revealed that the Weyl semimetallic electronic structure is realized in orthorhombic $MoTe_2$ through the direct observation of the Fermi arcs depending on the surface terminations.

Chapter 7

Discussion: The role of spin-orbit interaction

As we have seen in earlier chapters, spin-orbit interaction (SOI) can play an essential role in electronic structures and physical phenomena. In this chapter, we comprehensively discuss the effect of SOI on band dispersions in bulk.

7.1 Band dispersions with and without spin-orbit interaction

It is often said that the strong SOI of a heavy atom drastically modifies the band structure. This is partly correct. In Figs 7.1 (a) and (b), we present the bulk band structures of 3R-MoS_2 and β-$PdBi_2$ with (red) and without (blue) SOI along the high symmetry lines obtained by the first principles calculation. Corresponding Brillouin zones are shown in Figs. 7.1(c) and (d) with high symmetry points. For the 3R-MoS_2, in order to clearly describe the two dimensionality at Brillouin zone corners in 3R-MoS_2 as discussed in section 4.6, the reduced Brillouin zone is depicted by the black solid line. We can see drastic band modifications only in β-$PdBi_2$ due to the strong atomic SOI of Bi $6p$ orbitals compared with 3R-MoS_2. However, the bottoms of valence bands of β-$PdBi_2$ represented by the green rectangle which is mainly derived from the Bi $6p_z$ bonding sates are not changed in spite of the strong atomic SOI (~ 1 eV) of Bi atoms. In order to understand the role of SOI in band dispersions correctly, it is necessary to consider the symmetry of Bloch functions at each **k**-point for the band modification as suggested in Chapter 1.

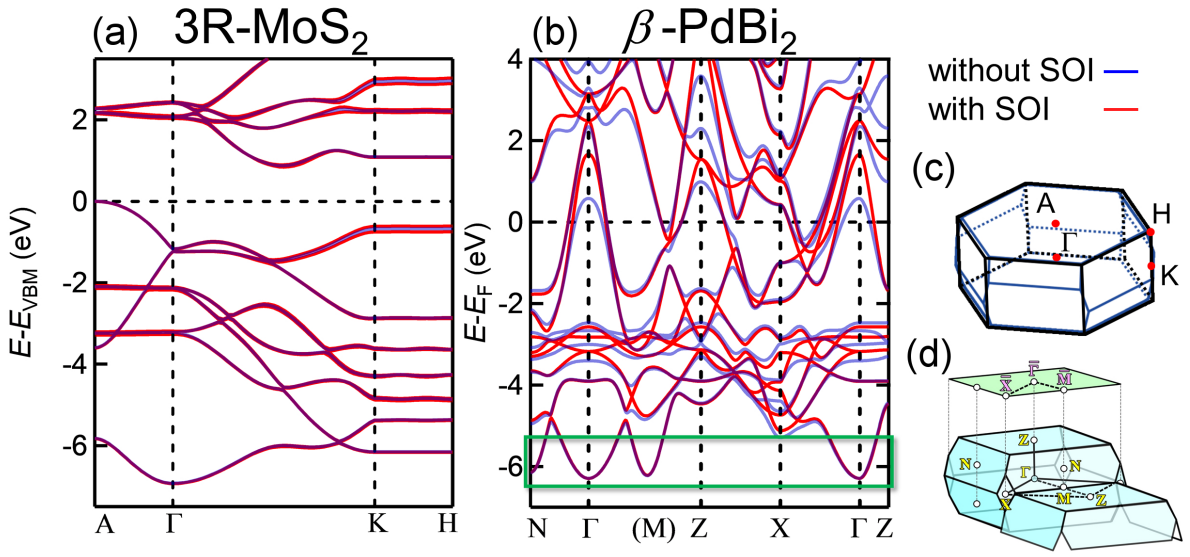

Figure 7.1: (a), (b) Calculated band dispersions with (red) and without (blue) spin-orbit interaction in bulk 3R-MoS_2 (a) and β-$PdBi_2$ (b). (c), (d) First Brillouin zones of 3R-MoS_2 (a) and β-$PdBi_2$ with the high symmetry points. Black (blue) solid lines represent the reduced (primitive) Brillouin zone of 3R-MoS_2 in (c).

To consider the effect of SOI in band dispersions qualitatively, it is useful to treat the SOI operator as

$$\lambda \boldsymbol{l} \cdot \boldsymbol{s} = \lambda[l_z s_z + \frac{1}{2}(l_+ s_- + l_- s_+)], \tag{7.1}$$

where λ represents the coupling constant, $\boldsymbol{l}$ is the orbital angular momentum, $\boldsymbol{s}$ is the spin angular momentum, l_z and s_z are z components of the orbital and spin angular momentum, and l_+, l_-, s_+ and s_- are the raising and lowering operators of the orbital momentum and spin angular momentum, respectively. The z-axis is as the main axis of the crystal structure. This formulation is suitable to describe the electron's orbital motion around the z-axis. Precise treatments of the $\mathbf{k} \cdot \mathbf{p}$ perturbation theory for band dispersions with SOI are given in ref. [6, 7]. Hereafter, we quantitatively discuss the role of eq.(7.1) in band dispersions along the characteristic $\mathbf{k}$-path of 3R-MoS_2, β-$PdBi_2$, and orthorhombic $MoTe_2$.

7.1.1 Band modification at Brillouin zone corner of 3R-MoS_2

Figure 7.2 shows band dispersions in 3R-MoS_2 near the Fermi level with (red solid line) and without (blue broken line) SOI along A-Γ-K-H. The vertical axis is the energy relative to the valence band maximum located at the A point. Except for the spin-valley coupled valence band (denoted as VB top) with spin-splitting $\sim$ 0.14 eV as discussed in Chap. 5, there is little difference between the band dispersions with and without SOI. For example, along the K-H line, the conduction band bottom (denoted as CB bottom) and the valence band lying at $E - E_{\mathrm{VBM}} \sim -3$ eV (denoted as VB 2nd) are not split in contrast to the VB top. To discuss their matrix elements, the orbital components of Mo and S atoms at the K point are listed in Table 7.1. It is not a bad approximation that the basis functions at the K point in 3R-MoS_2 are equal to those in monolayer MoS_2 [139, 140], because the interlayer hopping is suppressed as discussed in section 4.6. The dominant components are written in bold, and the subindices indicate the orbital magnetic momentum (magnetic quantum number). Since energy differences between the nearest neighbor bands ($\Delta E \simeq 2$ eV) for the VB top are greater than the SOI

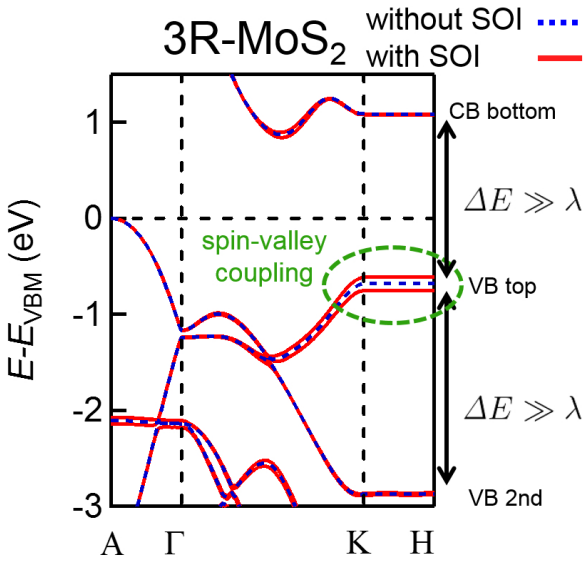

Figure 7.2: Band dispersions with (red solid line) and without (blue broken line) SOI along A-Γ-K-H line.

coupling constant (λ) of molybdenum (~ 0.1 eV) and sulfur (~ 0.05 eV) atoms [24–27] as shown in Fig. 7.2, these band dispersions at the K point near the Fermi level can be treated as the non-degenerate system.

Table 7.1: Orbital components of band dispersions near the Fermi level at the K point in 3R-MoS_2. The dominant components are written in bold. $d_{\pm 2} = \frac{1}{\sqrt{2}}(d_{x^2-y^2} \mp i d_{xy})$, $d_{\pm 1} = \frac{1}{\sqrt{2}}(d_{zx} \mp i d_{yz})$, $d_0 = d_{z^2}$, $p_{\pm 1} = \frac{1}{\sqrt{2}}(p_x \mp i p_y)$, $p_0 = p_z$.

Band index	Mo orbital	S orbital
CB bottom	$\boldsymbol{d_0}$	p_{+1}
VB top	$\boldsymbol{d_{-2}}$	p_{-1}
VB 2nd	d_{-1}	$\boldsymbol{p_0}$

In the non-degenerate system, the first (second) term on the right side of eq. 7.1 can be treated as the first (second) -order perturbation. The first term $l_z s_z$ gives the spin-splitting on bands having a non-zero z-component of the angular orbital momentum. It can explain that the SOI generates the band splitting with spin polarization of the VB top (d_{-2} is dominant, $l_z = -2$), in contrast to the CB bottom (d_0 is dominant, $l_z = 0$) and VB 2nd (p_0 is dominant, $l_z = 0$). We note that band dispersions in the noncentrosymmetric system can possess a non-zero angular momentum at each **k**-point. The second term ($l_+ s_- + l_- s_+$) can mix orbitals owing to l_+ and l_- operators with the suppression of spin polarization owing to s_+ and s_- operators. The mixing between the VB top and CB bottom is forbidden because the corresponding matrix element between d_0 and d_{-2} is zero. Though the mixing between the VB top and the VB 2nd is allowed, it is negligible because the orbital mixing roughly scales the energy ratio $\sim \frac{\lambda}{\Delta E}$ ($\lambda \sim 0.1$ eV, $\Delta E \sim 3$ eV). Thus, as a consequence of the non-zero magnetic quantum number and the suppression of second order perturbation, the spin-valley coupled valence band with 100% z-oriented spin polarization is realized at the Brillouin zone corners in 3R-MoS_2.

7.1.2 Energy levels at Γ and Z points in β-$PdBi_2$

Next, we discuss the bulk band structure on β-$PdBi_2$, especially focusing on the high symmetry line along Γ-Z. The band dispersions without (with) SOI along Γ-Z are shown in Fig. 7.3(a) and

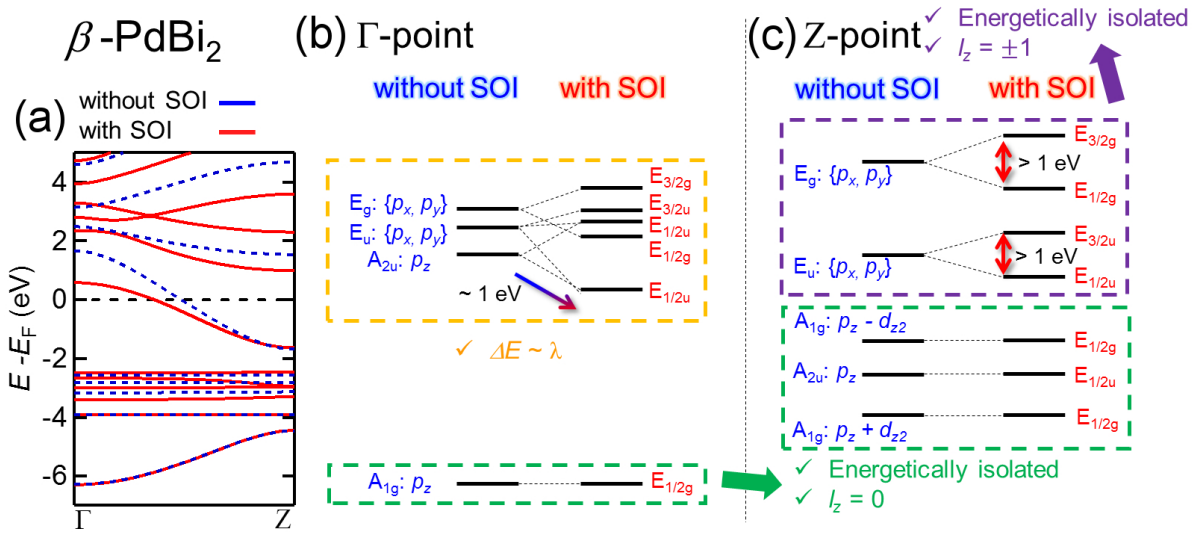

Figure 7.3: Band dispersions with (red solid curves) and without (blue broken curves) SOI in β-$PdBi_2$ along Γ-Z obtained by first-principles calculations. (b), (c) The energy levels at Γ and Z point mainly derived from bismuth $6p$ orbitals without (left) and with (right) SOI. The irreducible representations of point group D_{4h} are given for each level. Broken lines between the energy levels with and without SOI represent the orbital modifications due to SOI.

are represented by blue broken (red solid) curves. As discussed in Chap. 5, the Pd $4d$ orbitals are energetically localized around $E - E_F \sim -3$ eV, and the only $4d_{z^2}$ orbital at the Z-point mixes with the Bi $6p_z$ bonding state. The simple crystal structure and the high symmetry at Γ and Z points provide the one-to-one correspondence for the energy levels to the orbital character explicitly. To evaluate the effect of the strong SOI of the Bi atom ($\lambda > 1$ eV), the energy levels mainly derived from the Bi orbitals with and without SOI at the Γ and Z points are extracted in Figs. 7.3(b) and (c). At the Z point, the A_{1g} states are derived from the mixing between the Pd $4d_{z^2}$ orbital and the Bi $6p_z$ bonding state. Broken lines connecting the energy levels with and without SOI represent the band modifications obtained from eq. (7.1).

First, we focus on the bands nearly unchanged by the strong SOI ($\lambda > 1$ eV), as referred to at the beginning of this chapter. Their energy levels are denoted by green rectangles drawn with broken lines. In the same manner as for 3R-MoS_2 in section 7.1.1, it is explained by the

first and second term in the right side of eq. (7.1). That is, the orbital mixing derived from the second order perturbation in eq. (7.1) is sufficiently suppressed because those $l_z = 0$ orbitals are energetically isolated from the $l_z = \pm 1$ orbitals. In other words, electrons stretching straight toward neighbor atoms (*i.e.*, the wave functions with $l_z = 0$ on the Γ-Z line) hardly rotate around the nuclei so that those are not modified by spin-orbit coupling.

Next, we focus on the role of the second term of eq. (7.1) in the non-degenerate system. Similarly to the spin-valley coupled valence band top in 3R-MoS_2, energetically isolated bands at the Z point with the orbital magnetic moment $l_z = \pm 1$ along the z axis split into two pairs of bands, as denoted by the purple rectangle drawn with broken lines. We should note that the spin polarization at each **k**-point vanishes in the noncentrosymmetric system because of the equal contribution of $l_z = +1$ and $l_z = -1$. The energy of band-splitting > 1 eV reflects the strong atomic SOI of Bi $6p$ orbitals. Electrons in those bands with the transverse components of orbital angular momentum can be energetically stabilized or destabilized by rotating around the nuclei owing to the spin-orbit coupling.

Finally, we examine the orange rectangle drawn with broken lines in Fig. 7.3(b). Since the energy differences between energy levels at the Γ point are comparable to the energy of the atomic SOI of Bi $6p$ orbitals ($\lambda > 1$ eV), they should be treated as the nearly degenerate system with the strong SOI as necessary. Though both of the terms in eq. (7.1) can comparably contribute to modify the band dispersions, for convenience, we first consider the role of the first term ($l_z s_z$) in eq. (7.1). The anti-bonding states without SOI of Bi $\{6p_x, 6p_y\}$ represented by E_g can mix with the Bi $6p_z$ bonding state represented by A_{1g}, but they are energetically too far apart to mix with each other. Thus, the E_g states split into $E_{3/2g}$ and $E_{1/2g}$ states, as with those at the Z point. On the other hand, the bonding states without SOI of Bi $\{6p_x, 6p_y\}$ represented by E_u mix with the Bi $6p_z$ anti-bonding state represented by A_{2u}. Consequently, in addition to the band splitting due to the first term ($l_z s_z$) in eq. (7.1), the second term ($l_+ s_- + l_- s_+$) expresses two $E_{1/2u}$ states mixing with each other. The energy difference between the E_g and E_u states at the Γ point are smaller than the energy of atomic SOI, in contrast to that at the Z point. It triggers the parity inversion between the $E_{3/2u}$ and $E_{1/2g}$ states due to SOI. We note that the crossing of these band dispersions are protected by the C_{4v} rotational symmetry along

Γ-Z, in common with the Dirac semimetal Cd_3As_2 [73–75]. In the case of the parity inversion between the $E_{1/2u}$ and $E_{1/2g}$ states, the orbital mixing plays an important role to push the $E_{1/2u}$ state up above the $E_{1/2g}$ state.

7.1.3 Anti-symmetric spin-orbit coupling in orthorhombic $MoTe_2$

The Weyl semimetal phase with inversion symmetry breaking is necessarily accompanied by the spin-split band dispersions. Here, we discuss the effect of SOI for the spin-split band dispersions, which is called anti-symmetric spin-orbit coupling [26, 27, 212], in orthorhombic $MoTe_2$. In the case of 3R-MoS_2, the spin-splitting is understood by considering the magnetic orbital moment at each **k**-point in the band dispersions without SOI. This method is suitable only for a case

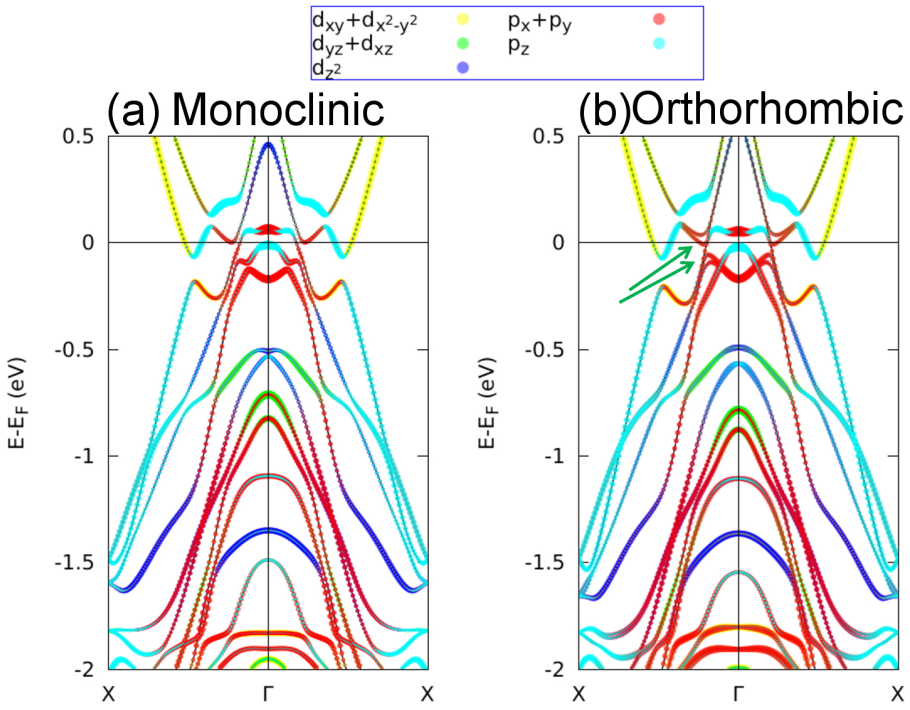

Figure 7.4: (a), (b) Calculated band dispersions along the Γ-X line in the monoclinic phase and the orthorhombic phase. The maximally localized Wannier functions are represented by different colors defined above. The spin-splitting derived from the polar crystal structure for the orthorhombic phase and the spin-orbit interaction are denoted by green arrows in (b).

in which the band dispersions are not significantly changed by SOI, except the corresponding spin-splitting, because the orbital components are usually mixed by SOI as per the second term in eq. (7.1), as seen in β-$PdBi_2$.

Band dispersions in the monoclinic and orthorhombic phase of $MoTe_2$ are shown in Figs. 7.4(a) and (b), respectively. Compared with 3R-MoS_2 and β-$PdBi_2$, significantly complicated band dispersions are obtained, reflecting the 12 atoms in a unit cell. Within the structural transition from the centrosymmetric monoclinic phase to the polar orthorhombic phase, the overall band structures are not significantly changed. This implies that the surface state (not contributing to the Fermi arcs) connecting the electron-like and hole-like bands observed in Figs. 6.5(a) and (b) survives still in the orthorhombic phase. Since this surface state lies in the boundary between the *d*-orbital electron-like and *p*-orbital hole-like band dispersions, it is probably topologically protected reflecting the *d*-*p* electron's band inversion. Small but remarkable differences in the spin-split band dispersions are observed near the Fermi level, as denoted by green arrows in Fig. 7.4(b). The origins of the Weyl nodes W1 and W2 are translated as the band inversions between an electron-like spin-split band above the Fermi level and two hole bands with slight spin-splitting [200]. The calculated results indicate that the spin-split band dispersions are mainly derived from the p_x and/or p_y orbitals. Since the non-zero orbital magnetic moment l_y consisting of the p_z and p_x orbitals are necessary to generate the spin-splitting along the k_x direction in the polar system (Rashba-type spin-splitting), the main Wannier function of the corresponding band dispersion is probably the p_x orbital. Harima and Yanase [26, 27] suggest that the microscopic origin of the anti-symmetric spin-orbit coupling is translated as the inter-site hopping with spin-flipping through the inter-site parity mixing in the tight binding model. For the orthorhombic $MoTe_2$, this implies that not only the *p*-orbitals but also *d*-orbitals play essential roles in the spin-splitting.

7.2 Parity inversion for topological insulator/metal

The parity-inverted band dispersions in the centrosymmetric topological insulators or metals are often accompanied by the band modification owing to the strong SOI. One of the exceptions

is realized in β-$PdBi_2$ in which the parity inversion exists in band dispersions without SOI as discussed in section 5.8.2. Here, we summarize typical parity inversions based on the knowledge obtained through our studies as follows.

Case 1: *Band modification owing to SOI*

Figure 7.5(a) shows the simplest case of the parity inversion owing to SOI. We assume that eigenstates derived from the p-orbital lie above (below) the band gap and an eigenstate having even parity (e.g. s, d orbital) lies below the band gap in band dispersions without SOI. Here, the eigenstates with odd parity are depicted in red. It is given that the p orbitals with odd parity have strong SOI, while the eigenstate with even parity does not. The strong SOI (e.g., bismuth $6p$ orbitals $\lambda > 1$ eV) energetically stabilizes the eigenstates mainly derived from the p_z orbital drastically, leading to the band inversion between the eigenstates with odd and even parity. Such situations are widely seen in realistic topological insulators (e.g., in Bi_2Se_3, the bonding state of Bi atoms and the anti-bonding state of Se atoms [62]). The even- and odd- parity states can also be created by the bonding and anti-bonding states derived from two same atoms in a unit cell. If the energy of SOI overcomes the energy difference between those states, the parity inversion is obtained as shown in Fig. 7.5(b). For example, in the crystals including more than two Bi atoms, such band inversions should be commonly realized as in β-$PdBi_2$. Actually, such a parity inversion seems to be realized in the unoccupied band dispersions in Bi_2Se_3 [213, 214]. We should note that the energy difference between the $\{p_x, p_y\}$ and p_z [$\{p_x, p_y\}$ anti-bonding and $\{p_x, p_y\}$ bonding] states in Fig. 7.5(a) [Fig. 7.5(b)] varies in momentum space. It offers a good condition for strong topological insulators or metals, e.g., corresponding bands are inverted at the Γ point but not at the Z point as seen in β-$PdBi_2$.

Case 2: *Chemical bonding*

The parity-inverted band structure can be obtained without spin-orbit interaction, as seen in β-$PdBi_2$. The simplest way is to utilize the difference of the parity of peripheral electrons such as in the case for the p-d electron system shown in Fig. 7.5(c). This condition depends on various parameters (such as chemical bondings in the provided crystal structure, bandwidth of

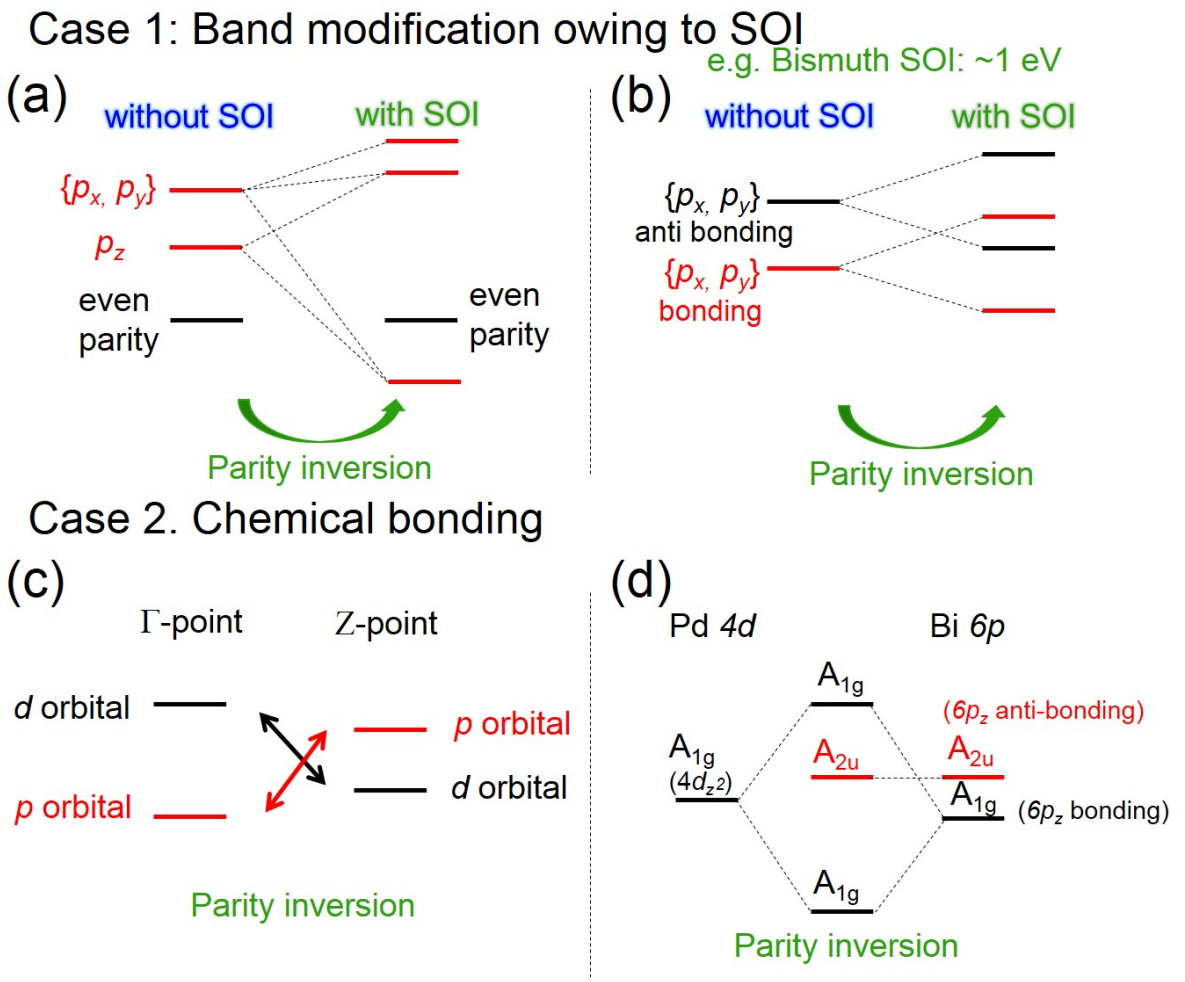

Figure 7.5: (a), (b) Schematics of energy levels related to the parity inversions derived from the band modifications due to SOI. (c) Parity inversion due to the chemical bonding in the case of β-$PdBi_2$. Eigenstates with odd parity are indicated in red.

corresponding orbitals, energy of peripheral electrons, etc.). Such a situation is likely realized in semimetal $MoTe_2$ consisting of the Mo d-orbital and Te p-orbital.

In order to find the parity-inverted band structure from a strategic perspective, it is a good strategy to focus on the bonding and anti-bonding states, similar to the case in Fig. 7.5(b). Basically, the anti-bonding state is located at an energy higher than (or equal to) the bonding

state over the entire Brillouin zone. As a conspicuous example, the bonding and anti-bonding states in the nonsymmorphic crystal structure stick at the Brillouin zone boundary [6]. By reducing the nonsymmorphic symmetry (i.e., ordinary conditions of two or more atoms in unit cell), this band sticking is lifted, resulting in the small energy gap between the bonding and anti-bonding states at the zone boundary. Such a small energy gap can trigger the parity-inverted band dispersions through mixing with another atom's orbital. The corresponding case in β-$PdBi_2$ is presented in Fig. 7.5(d). It suggests that the Bi $6p_z$ bonding state (represented by the A_{1g}) overcomes the Bi $6p_z$ anti-bonding state (A_{2u}) by mixing with the Pd $4d_{z^2}$ orbital (A_{1g}) (as precisely discussed in section. 6.7). Though it has not attracted attention yet, this type of parity inversion is considered to exist widely in the *s*-*p* or *p*-*d* electron systems such as transition metal dichalcogenides.

In summary, the good conditions for the parity-inverted band structure are listed as follows.
The crystal structure includes
· Atoms with strong spin-orbit interaction
· Different-parity atoms (*i.e.* *p*-*d*, *s*-*p* electron system)
· Two (or more) of the same atoms in a unit cell (even/odd parity by bonding/anti-bonding state)
The parity inversion occurs in a topological insulator / metal with space inversion symmetry. For the Weyl semimetal with space inversion symmetry breaking, its electronic structure can be understood by the intermediate state of the normal insulator and topological insulator because corresponding bands are inverted partly in momentum space. Even in such a system with broken space inversion symmetry, those conditions still play significant roles in the band inversion observed along a high-symmetry line in momentum space.

Chapter 8

Conclusion

In this thesis, we have experimentally investigated the role of spin-orbit interaction in the band structures of strongly spin-orbit coupled materials hosting the spin-momentum locked electronic structure by using the state-of-art angle-resolved photoemission spectroscopy (ARPES) measurement and spin-resolved ARPES measurement with the help of first-principles calculations. Both in the noncentrosymmetric materials and topological materials, which are the target materials in this thesis, we reveal that the spin-orbit interaction plays an essential role in the bulk electronic structures through the orbital degree of freedom on the band dispersions. We already summarized the main results at the end of each chapter. In the following, we present conclusions and future prospects from a general viewpoint.

Chapter 3. Development of laser ARPES system

We have developed the laser ARPES system using the Ti:sapphire laser with commercial nonlinear optical crystals. Advantages of using a laser light source (narrow line width, high intensity and small spot size) have enabled precise measurement with good momentum ($\Delta k < 0.002$ Å^{-1}) and energy resolution ($\Delta E < 0.9$ meV) for the polar semiconductor BiTeBr, iron superconductor FeSe and polar semimetal orthorhombic $MoTe_2$. Especially, the small spot size (~ 0.1 mm) was very useful to distinguish domains in the polar semimetal orthorhombic $MoTe_2$. The easily realized sub-mm scale spot size in a laboratory system comparable to a synchrotron light source has a profound significance. In this thesis, the orbital component of band dispersion is mainly determined with the help of first-principles calculation. To use circularly polarized

light, there is a possibility to detect the orbital magnetic moment contributing to the spin-orbit interaction experimentally, by taking account of the matrix elements in the photoexcitation process.

Chapter 4. Spin-valley coupling in 3R-polytype MoS_2

We have revealed the spin-valley coupled electronic structure in bulk 3R-MoS_2. The top of the valence bands at the inequivalent valleys are mainly derived from Mo $4d$ orbitals with $l_z = +2$ or -2, and they give rise to the spin-splitting ~ 0.17 eV with the out-of-plane full spin polarizations. Those spin-valley coupled band structures at the Brillouin zone corners are evaluated to be the same as those on monolayer MoS_2 because the nearest- and next-nearest-neighbor interlayer hopping in 3R-MoS_2 are symmetrically forbidden. It is worth noting that the two-dimensionally localized electronic structures are built in the three-dimensional bulk crystal and provides the novel functions. As well as the circular dichroic photoluminescence observed in 3R-MoS_2, the pump-probe ARPES measurement using the circularly polarized laser light source will reveal the spin and valley coupled relaxation process in photo-excited states.

Chapter 5. Topological surface states on superconductor β-$PdBi_2$

The topologically protected surface states in β-$PdBi_2$ lying at $E - E_F \sim 2.4$ eV and across the Fermi level have been directly observed. Those surface states are characterized by the Z_2 topological invariant in analogy to the centrosymmetric topological insulator. Their origins are revealed by considering the chemical bonding of two Bi atoms, which form the bonding and anti-bonding states with odd and even parity, in a body-centered unit cell. One of the parity inverted band dispersions in β-$PdBi_2$ is realized by Bi $6p$-Pd $4d$ mixing without the help of spin-orbit interaction. The other originates from the strong spin-orbit coupling of the Bi $\{6p_x, 6p_y\}$ ($l_z = \pm 1$) orbital (> 1 eV). Through this investigation, we have found three good conditions for the topological insulator / metal realized in solids as follows; (I) atoms with strong spin-orbit interaction, (II) different-parity atoms (*i.e.* *p-d*, *s-p* electron system), and (III) two (or more) of the same atoms in a unit cell (even/odd parity by bonding/anti-bonding state). Our findings will stimulate investigations on the topological surface states coexisting with other unconventional

electronic states (e.g., superconductivity, magnetism etc.) in metallic band dispersions.

Chapter 6. Topological surface states on polar semimetal $MoTe_2$

Weyl semimetallic electronic structure in polar semimetal orthorhombic $MoTe_2$ is experimentally confirmed through the direct observation on the Fermi-arcs. The electronic structure near the Fermi level in $MoTe_2$ consists of the Mo $4d$ orbitals and Te $5p$ orbitals, and those form the type-II Weyl semimetallic electronic structure accompanying the Fermi-arcs lying at the boundary of the electron and hole pockets. The shapes of Fermi-arcs depend on the surface termination [connecting W1-W1 Weyl nodes on (00-1) surface, and W1-W2 Weyl nodes on (001) surface], selectively observed by using the laser ARPES system with the small spot size ($\sim$ 0.1 mm). Even in the complicated band dispersions with the low crystal symmetry, considering the dominant orbital component in bands is helpful to understand the effect of spin-orbit interaction and topologically nontrivial electronic structure.

We have revealed the origins of band shift and band splitting due to the spin-orbit interaction in solids, through investigations on the noncentrosymmetric materials and topological materials by using ARPES and spin-resolved ARPES. Considering the band structure's energy levels (depending on the ligand field, kinetic energy, etc.) and orbital characters at each **k**-point, the role of spin-orbit interaction in the band dispersions can be understood. The ARPES measurement combined with computational band calculation is a powerful method because it can provide both the band dispersions and its orbital character. We believe that this study contributes to the basis for next generation electronics sustaining future society.

References

[1] 朝永振一郎、「新版　スピンはめぐる」　(みすず書房、2008)

[2] P. A. M. Dirac *The quantum theory of the electron*, Proc. R. Soc. A **117**, 610-624 (1928).

[3] L. L. Foldy and S. A. Wouthuysen *On the Dirac Theory of Spin 1/2 Particles and Its Non-Relativistic Limit*, Phys. Rev. **78**, 29-36 (1950).

[4] S. Tani, *Connection between Particle Models and Field Theories, I The Case Spin 1/2*, Prog. of Theor. Phys. **6**, 267-285 (1951).

[5] L. H. Thomas, *The motion of the spinning electron*, Nature (London) **117**, 514 (1926).

[6] M. S. Dresselhaus, G. Dresselhaus and A. Jorio, *Group Theory: Application to the Physics of Condensed Matter* (Springer, 2008).

[7] G. Dresselhaus, *Spin-Orbit Coupling Effects in Zinc Blende Structures*, Phys. Rev. **100**, 580-586 (1955).

[8] R. J. Elliott, *Theory of the Effect of Spin-Orbit Coupling on Magnetic Resonance in Some Semiconductors*, Phys. Rev. **96**, 266-279 (1954).

[9] R. J. Elliott, *Spin-Orbit Coupling in Band Theory Character Tables for Some Double Space Groups* , Phys. Rev. **96**, 280-287 (1954)

[10] E. I. Rashba *Simmetriya energeticheskikh zon v kristallakh tipa vyurtsita. I. Simmetriya zon bez ucheta spin-orbital' nogo vzaimodeistviya*, Fiz. Tverd. Tela **1**, 407-421 (1959). [E.

I. Rashba, *Symmetry of bands in wurzite-type crystals. 1. Symmetry of bands disregarding spin-orbit interaction*, Sov. Phys. Solid. State **1**, 368 (1959)]

[11] E. I. Rashba and V. I. Sheka, *immetriya energeticheskikh zon v kristallakh tipa vyurtsita. II. Simmetriya zon s uchyotom spinovykh vzaimodeistvii*, Fiz. Tverd. Tela **1**, 162-176 (1959).

[12] C. Herring, *A New Method for Calculating Wave Functions in Crystals*, Phys. Rev. **57**, 1169-1177 (1940).

[13] F. Herman, *Electronic Structure of the Diamond Crystal*, Phys. Rev. **88**, 1210-1211 (1952).

[14] F. Herman, Thesis, Columbia University, (1953). unpublished.

[15] F. Herman, *Calculation of the Energy Band Structures of the Diamond and Germanium Crystals by the Method of Orthogonalized Plane Waves*, Phys. Rev. **93**, 1214-1225 (1954).

[16] E. Zavoisky, *Relaxation of liquid solutions for perpendicular fields*, J. Phys. USSR **9** 211-216 (1945).

[17] G. Dresselhaus, A. F. Kip, and C. Kittel, *Cyclotron Resonance of Electrons and Holes in Silicon and Germanium Crystals*, Phys. Rev. **98**, 368-384 (1955).

[18] S. Hüfner, *Photoelectron spectroscopy : principles and applications*, (Springer-Verlag, 2003), 3rd edn.

[19] S. D. Kevan (ed.), *Angle -Resolved Photoemission*, (Elsevier, 1992).

[20] S. Hüfner , R. Claessen , F. Reinert , Th. Straub , V. N. Strocov and P. Steiner *Photoemission spectroscopy in metals: band structure-Fermi surfacespectral function*, J. Electron Spectrosc. Relat. Phenom. **100** 191-213 (1999).

[21] A. Damascelli, Z. Hussain and Z.-X. Shen, *Angle-resolved photoemission studies of the cuprate superconductors*, Rev. Mod. Phys. **75**, 473-541 (2003).

[22] P. Hohenberg and W. Kohn, *Inhomogeneous Electron Gas*, Phys. Rev. **136**, B864-871 (1964).

[23] W. Kohn and L. J. Sham, *Self-Consistent Equations Including Exchange and Correlation Effects*, Phys. Rev. **140**, A1133-1138 (1965).

[24] 小口多美夫, 獅子堂達也, 「表面 Rashba 効果–スピン軌道相互作用と対称性」, 固体物理 **44**, 79 (2009).

[25] 柳瀬陽一, 播磨尚朝, 「スピン軌道相互作用と結晶中の電子状態（その 1）孤立原子におけるスピン軌道相互作用の定量的評価」, 固体物理 **46**, 229 (2011).

[26] 柳瀬陽一, 播磨尚朝, 「スピン軌道相互作用と結晶中の電子状態（その 2）空間反転対称性が破れた系の反対称スピン軌道相互作用」, 固体物理 **46**, 283 (2011).

[27] 柳瀬陽一, 播磨尚朝, 「スピン軌道相互作用と結晶中の電子状態（その 3：最終回） 空間反転対称性が破れた系の反対称スピン軌道相互作用（応用編）」, 固体物理 **47**, 101 (2012).

[28] L. P. Bouckaert, R. Smoluchowski and E. Wigner, *Theory of Brillouin Zones and Symmetry Properties of Wave Functions in Crystals*, Phys. Rev. **93**, 58-67 (1936).

[29] R. C. Casella, *Symmetry of Wurtzite* Phys. Rev. **114**, 1514-1518 (1959).

[30] R. C. Casella, *Toroidal Energy Surfaces in Crystals with Wurtzite Symmetry* Phys. Rev. Lett **5**, 371-373 (1960).

[31] M. N. Baibich, J. M. Broto, A. Fert, F. Nguyen Van Dau, F. Petroff, P. Etienne, G. Creuzet, A. Friederich and J. Chazelas, *Giant Magnetoresistance of (001)Fe/(001)Cr Magnetic Superlattices*, Phys. Rev. Lett. **61**, 2472-2474 (1989).

[32] S. Datta and B. Das, *Electronic analog of the electro-optic modulator*, Appl. Phys. Lett. **56**, 665667 (1990)

[33] S. Murakami, N. Nagaosa and S.-C. Zhang, *Dissipationless Quantum Spin Current at Room Temperature*, Science **301**, 1348-1351 (2003).

[34] J. Sinova, D. Culcer, Q. Niu, N. A. Sinitsyn, T. Jungwirth and A. H. MacDonald, *Universal Intrinsic Spin Hall Effect*, Phys. Rev. Lett. **92**, 126603 (2004).

[35] Y. K. Kato, R. C. Myers, A. C. Gossard, D. D. Awschalom, *Observation of the spin Hall effect in semiconductors*, Science **306**, 1910-1913 (2004).

[36] I. M. Miron, K. Garello, G. Gaudin, P.-J. Zermatten, M. V. Costache, S. Auffret, S. Bandiera, B. Rodmacq, A. Schuhl and P. Gambardella, *Perpendicular switching of a single ferromagnetic layer induced by in-plane current injection*, Nature **476**, 189-193 (2010).

[37] I. M. Miron, G. Gaudin, S. Auffret, B. Rodmacq, A. Schuhl, S. Pizzini, J. Vogel and P. Gambardella, *Current-driven spin torque induced by the Rashba effect in a ferromagnetic metal layer*, Nat. Mater. 9, 230-234 (2010).

[38] L. Liu, C.-F. Pai, Y. Li, H. W. Tseng, D. C. Ralph and R. A. Buhrman, *Spin-Torque Switching with the Giant Spin Hall Effect of Tantalum*, Science **336**, 555-558 (2012).

[39] K. Ishizaka, M. S. Bahramy, H. Murakawa, M. Sakano, T. Shimojima, T. Sonobe, K. Koizumi, S. Shin, H. Miyahara, A. Kimura, K. Miyamoto, T. Okuda, H. Namatame, M. Taniguchi, R. Arita, N. Nagaosa, K. Kobayashi, Y. Murakami, R. Kumai, Y. Kaneko, Y. Onose and Y. Tokura, *Giant Rashba-type spin splitting in bulk BiTeI* Nature Mater. **10**, 521-526 (2011).

[40] A. Crepaldi, L. Moreschini, G. Autès, C. Tournier-Colletta, S. Moser, N. Virk, H. Berger, Ph. Bugnon, Y. J. Chang, K. Kern, A. Bostwick, E. Rotenberg, O. V. Yazyev, and M. Grioni, *Giant Ambipolar Rashba Effect in the Semiconductor BiTeI*, Phys. Rev. Lett. **109**, 096803 (2012).

[41] G. Landolt, S. V. Eremeev, Y. M. Koroteev, B. Slomski, S. Muff, T. Neupert, M. Kobayashi, V. N. Strocov, T. Schmitt, Z. S. Aliev, M. B. Babanly, I. R. Amiraslanov, E. V. Chulkov, J. Osterwalder and J. H. Dil, *Disentanglement of Surface and Bulk Rashba Spin Splittings in Noncentrosymmetric BiTeI*, Phys. Rev. Lett. **109**, 116403 (2012).

[42] M. Sakano, J. Miyawaki, A. Chainani, Y. Takata, T. Sonobe, T. Shimojima, M. Oura, S. Shin, M. S. Bahramy, R. Arita, N. Nagaosa, H. Murakawa, Y. Kaneko, Y. Tokura and K.

Ishizaka, *Three-dimensional bulk band dispersion in polar BiTeI with giant Rashba-type spin splitting*, Phys. Rev. B **86**, 085204 (2012).

[43] M. Sakano, M. S. Bahramy, A. Katayama, T. Shimojima, H. Murakawa, Y. Kaneko, W. Malaeb, S. Shin, K. Ono, H. Kumigashira, R. Arita, N. Nagaosa, H. Y. Hwang, Y. Tokura and K. Ishizaka, *Strongly Spin-Orbit Coupled Two-Dimensional Electron Gas Emerging near the Surface of Polar Semiconductors*, Phys. Rev. Lett. **110**, 107204 (2013).

[44] 坂野昌人, 「極性層状ビスマス化合物におけるバルクとサブ表面のスピン分裂バンド構造」, 東京大学大学院工学系研究科　物理工学専攻　修士論文,　(2013).

[45] Yu. A. Bychkov and E. I. Rashba, *Properties of a 2D electron gas with lifted spectral degeneracy*, JETP Lett. **39**, 78-81 (1984).

[46] S. LaShell, B. A. McDougall and E. Jensen, *Spin Splitting of an Au(111) Surface State Band Observed with Angle Resolved Photoelectron Spectroscopy*, Phys. Rev. Lett. **77**, 3419-3422 (1996).

[47] M. Hoesch, M. Muntwiler, V. N. Petrov, M. Hengsberger, L. Patthey, M. Shi, M. Falub, T. Greber and J. Osterwalder, *Spin structure of the Shockley surface state on Au(111)*, Phys. Rev. B **69**, 241401 (2004).

[48] Yu. M. Koroteev, G. Bihlmayer, J. E. Gayone, E. V. Chulkov, S. Blgel, P. M. Echenique and Ph. Hofmann, *Strong spinorbit splitting on Bi surfaces*, Phys. Rev. Lett. **93**, 046403 (2004).

[49] J. Nitta , T. Akazaki, H. Takayanagi and H. Enoki, *Gate Control of Spin-Orbit Interaction in an Inverted* $In_0.53Ga_0.47As/In0.52Al_0.48As$ *Heterostructure*, Phys. Rev. Lett. **78**, 1335-1338 (1997).

[50] C. R. Ast, J. Henk, A. Ernst, L. Moreschini, M. C. Falub, D. Pacilé, P. Bruno, K. Kern and M. Grioni, *Giant Spin Splitting through Surface Alloying*, Phys. Rev. Lett. **98**, 186807 (2007).

[51] M. S. Bahramy, R. Arita and N. Nagaosa, *Origin of giant bulk Rashba splitting: Application to BiTeI*, Phys. Rev. B **84**, 041202(R) (2011)

[52] K. Tsutsui and S. Murakami *Spin-torque efciency enhanced by Rashba spin splitting in three dimensions*, Phys. Rev. B **86**, 115201 (2012).

[53] C. L. Kane and E. J. Mele, *Quantum Spin Hall Effect in Graphene* Phys. Rev. Lett. **95**, 146802 (2005).

[54] C. L. Kane and E. J. Mele, Z_2 *Topological Order and the Quantum Spin Hall Effect*, Phys. Rev. Lett. **95**, 226801 (2005).

[55] B. A. Bernevig and S.-C. Zhang, *Quantum Spin Hall Effect*, Phys. Rev. Lett. **96**, 106802 (2006).

[56] L. Fu and C. L. Kane *Time reversal polarization and a* Z_2 *adiabatic spin pump*, Phys. Rev. B **74**, 195312 (2006).

[57] L. Fu, C. L. Kane and E. J. Mele, *Topological Insulators in Three Dimensions* Phys. Rev. Lett. **98**, 106803 (2007).

[58] J. E. Moore and L. Balents, *Topological invariants of time-reversal-invariant band structures*, Phys. Rev B **75**, 121306(R) (2007).

[59] M. König, S. Wiedmann, C Bröne, A. Roth, H. Buhmann, L. W. Molenkamp, X.-L. Qi and S.-C. Zhang *Quantum Spin Hall Insulator State in HgTe Quantum Wells*, Science **318** 766-770 (2007).

[60] D. Hsieh, D. Qian, L. Wray, Y. Xia, Y. S. Hor, R. J. Cava and M. Z. Hasan, *A topological Dirac insulator in a quantum spin Hall phase*, Nature **452**, 970-974 (2008).

[61] D. Hsieh, Y. Xia, L. Wray, D. Qian, A. Pal, J. H. Dil, J. Osterwalder, F. Meier, G. Bihlmayer, C. L. Kane, Y. S. Hor, R. J. Cava and M. Z. Hasan, *Observation of Unconventional Quantum Spin Textures in Topological Insulators*, Science **323**, 919-922 (2009).

[62] H. Zhang, C.-X. Liu, X.-L. Qi, X. Dai, Z. Fang and S.-C. Zhang, *Topological insulators in Bi_2Se_3, Bi_2Te_3 and Sb_2Te_3 with a single Dirac cone on the surface*, Nat. Phys. **5**, 438-442 (2009).

[63] D. Hsieh, Y. Xia, D. Qian, L. Wray, J. H. Dil, F. Meier, J. Osterwalder, L. Patthey, J. G. Checkelsky, N. P. Ong, A. V. Fedorov, H. Lin, A. Bansil, D. Grauer, Y. S. Hor, R. J. Cava and M. Z. Hasan, *A tunable topological insulator in the spin helical Dirac transport regime*, Nature **460**, 1101-1105 (2009).

[64] D. Hsieh, Y. Xia, D. Qian, L. Wray, F. Meier, J. H. Dil, J. Osterwalder, L. Patthey, A. V. Fedorov, H. Lin, A. Bansil, D. Grauer, Y. S. Hor, R. J. Cava and M. Z. Hasan, *Observation of Time-Reversal-Protected Single-Dirac-Cone Topological-Insulator States in Bi_2Te_3 and Sb_2Te_3*, Phys. Rev. Lett. **103**, 146401 (2009).

[65] Y. Xia, D. Qian, D. Hsieh, L. Wray, A. Pal, H. Lin, A. Bansil, D. Grauer, Y. S. Hor, R. J. Cava and M. Z. Hasan, *Observation of a large-gap topological-insulator class with a single Dirac cone on the surface*, Nat. Phys. **5**, 398-402 (2009).

[66] L. Fu *Topological Crystalline Insulators*, Phys. Rev. Lett. **106**, 106802 (2011).

[67] Y. Tanaka, Z. Ren, T. Sato, K. Nakayama, S. Souma, T. Takahashi, K. Segawa and Y. Ando, *Experimental realization of a topological crystalline insulator in SnTe* Nat. Phys. **8**, 800803 (2012).

[68] P. Dziawa, B. J. Kowalski, K. Dybko, R. Buczko, A. Szczerbakow, M. Szot, E. Łusakowska, T. Balasubramanian, B. M. Wojek, M. H. Berntsen, O. Tjernberg and T. Story, *Topological crystalline insulator states in $Pb_{1-x}Sn_xSe$*, Nat. Mater. **11**, 1023-1027 (2012).

[69] A. P. Schnyder, S. Ryu, A. Furusaki and A. W. W. Ludwig *Classification of topological insulators and superconductors in three spatial dimensions*, Phys. Rev. B **78**, 195125 (2008).

[70] Y. S. Hor, A. J. Williams, J. G. Checkelsky, P. Roushan, J. Seo, Q. Xu, H. W. Zandbergen, A. Yazdani, N. P. Ong and R. J. Cava, *Superconductivity in $Cu_xBi_2Se_3$ and its Implications for Pairing in the Undoped Topological Insulator*, Phys. Rev. Lett. **104**, 057001 (2010).

[71] M. Kriener, K. Segawa, Z. Ren, S. Sasaki and Y. Ando, *Bulk Superconducting Phase with a Full Energy Gap in the Doped Topological Insulator* $Cu_xBi_2Se_3$, Phys. Rev. Lett. **106**, 127004 (2011).

[72] L. Fu and E. Berg *Odd-Parity Topological Superconductors: Theory and Application to* $Cu_xBi_2Se_3$, Phys. Rev. Lett. **105**, 097001 (2010).

[73] M. Neupane, S.-Y. Xu, R. Sankar, N. Alidoust, G. Bian, C. Liu, I. Belopolski, T.-R. Chang, H.-T. Jeng, H. Lin, A. Bansil, F.C. Chou, and M.Z. Hasan, *Observation of a three-dimensional topological Dirac semimetal phase in high-mobility* Cd_3As_2, Nat. Commun. **5**, 3786 (2014).

[74] Z.K. Liu, J. Jiang, B. Zhou, Z.J. Wang, Y. Zhang, H.M. Weng, D. Prabhakaran, S.-K. Mo, H. Peng, P. Dudin, T. Kim, M. Hoesch, Z. Fang, X. Dai, Z.X. Shen, D.L. Feng, Z. Hussain and Y.L. Chen, *A Stable Three-Dimensional Topological Dirac Semimetal* Cd_3As_2, Nat. Mater. **13**, 677-681 (2014).

[75] S. Borisenko, Q. Gibson, D. Evtushinsky, V. Zabolotnyy, B. Bchner and R.J. Cava, *Experimental Realization of a Three-Dimensional Dirac Semimetal*, Phys. Rev. Lett. **113**, 027603 (2014).

[76] X. Wan, A. M. Turner, A. Vishwanath and S. Y. Savrasov *Topological semimetal and Fermi-arc surface states in the electronic structure of pyrochlore iridates*, Phys. Rev. B **83**, 205101 (2011).

[77] S. Murakami, *Phase transition between the quantum spin Hall and insulator phases in 3D: emergence of a topological gapless phase*, New J. Phys. **9**, 356 (2007).

[78] A. A. Burkov and L. Balents, *Weyl Semimetal in a Topological Insulator Multilayer*, Phys. Rev. Lett. **107**, 127205

[79] S. Borisenko, D. Evtushinsky, Q. Gibson, A. Yaresko, T. Kim, M. N. Ali, B. Buechner, M. Hoesch, R. J. Cava, *Time-reversal symmetry breaking Weyl state in* $YbMnBi_2$, arXiv:1507.04847 (2015).

[80] S.-Y. Xu, I. Belopolski, N. Alidoust, M. Neupane, G. Bian, C. Zhang, R. Sankar, G. Chang, Z. Yuan, C.-C. Lee, S.-M. Huang, H. Zheng, J. Ma, D. Sanchez, B. Wang, A. Bansil, F. Chou, P. Shibayev, H. Lin, S. Jia and M. Z. Hasan, *Discovery of a Weyl fermion semimetal and topological Fermi arcs*, Science **349**, 613-617 (2015).

[81] B.Q. Lv, H.M. Weng, B.B. Fu, X.P. Wang, H. Miao, J. Ma, P. Richard, X.C. Huang, L.X. Zhao, G.F. Chen, Z. Fang, X. Dai, T. Qian and H. Ding, *Experimental Discovery of Weyl Semimetal TaAs*, Phys. Rev. X **5**, 031013 (2015).

[82] L. X. Yang, Z. K. Liu, Y. Sun, H. Peng, H. F. Yang, T. Zhang, B. Zhou, Y. Zhang, Y. F. Guo, M. Rahn, D. Prabhakaran, Z. Hussain, S.-K. Mo, C. Felser, B. Yan, and Y. L. Chen, *Weyl semimetal phase in the non-centrosymmetric compound TaAs*, Nat. Phys. **11**, 728-732 (2015).

[83] B. Q. Lv, N. Xu, H. M. Weng, J. Z. Ma, P. Richard, X. C. Huang, L. X. Zhao, G. F. Chen, C. Matt, F. Bisti, V. Strokov, J. Mesot, Z. Fang, X. Dai, T Qian, M. Shi and H. Ding, *Observation of Weyl nodes in TaAs*, Nat. Phys. **11**, 724-727 (2015).

[84] S.-Y. Xu, N. Alidoust, I. Belopolski, Z. Yuan, G. Bian, T.-R. Chang, H. Zheng, V. N. Strocov, D. S. Sanchez, G. Chang, C. Zhang, D. Mou, Y. Wu, L. Huang, C.-C. Lee, S.-M. Huang, B. Wang, A. Bansil, H.-T. Jeng, T. Neupert, A. Kaminski, H. Lin, S. Jia and M. Z. Hasan, *Discovery of a Weyl fermion state with Fermi arcs in niobium arsenide*, Nat. Phys. **11**, 748-754 (2015).

[85] N. Xu, H. M. Weng, B. Q. Lv, C. Matt, J. Park, F. Bisti, V. N. Strocov, D. Gawryluk, E. Pomjakushina, K. Conder, N. C. Plumb, M. Radovic, G. Aut‘es, O. V. Yazyev, Z. Fang, X. Dai, G. Aeppli, T. Qian, J. Mesot, H. Ding and M. Shi, *Observation of Weyl nodes and Fermi arcs in TaP*, arXiv:1507.03983 (2015).

[86] H. Hertz, *Ueber einen Einfluss des ultravioletten Lichtes auf die electrische Entladung*, Annalen der Physik und Chemie **267**, 983-1000 (1887).

[87] A. Einstein, *Über einen die Erzeugung und Verwandlung des Lichtes betreffenden heuristischen Gesichtspunkt*, Ann. Phys. (Leipzig) **322**, 132-148 (1905).

[88] H. Y. Fan, *Theory of Photoelectric Emission from Metals*, Phys. Rev. **68**, 43-52 (1945).

[89] C. N. Berglund and W. E. Spicer, *Photoemission Studies of Copper and Silver: Theory*, Phys. Rev. **136**, A1030-1044 (1964).

[90] P. J. Feibelman and D. E. Eastman, *Photoemission spectroscopy—Correspondence between quantum theory and experimental phenomenology*, Phys. Rev. B **10**, 4932-4947 (1974).

[91] E. Kisker, R. Clauberg and W. Gudat, *Electron spectrometer for spin- polarized angle- and energy- resolved photoemission from ferromagnets*, Rev. Sci. Instrum. **53**, 1137-1144 (1982).

[92] M. Getzlaff, B. Heidemann, J. Bansmann, C. Westphal and G. Schönhensee, *A variable-angle electron spin polarization detection system*, Rev. Sci. Instrum. **69**, 3913-3923 (1998).

[93] G. C. Burnett, T. J. Monroe and F. B. Dunning, *High- efficiency retarding- potential Mott polarization analyzer*, Rev. Sci. Instrum. **65**, 1893-1896 (1994).

[94] S. Qiao, A. Kimura, A. Harasawa, M. Sawada, J.-G. Chung and A. Kakizaki, *A new compact electron spin polarimeter with a high efficiency*, Rev. Sci. Instrum. **68**, 4390-4395 (1997).

[95] G. Ghiringhelli, K. Larsson and N. B. Brookes, *High-efficiency spin-resolved and spin-integrated electron detection: Parallel mounting on a hemispherical analyzer*, Rev. Sci. Instrum. **70**, 4225-4230 (1999).

[96] M. Hoesch, T. Greber, V. N. Petrov, M. Muntwiler, M. Hengsberger, W. Auwrter and J. Osterwalder, *Spin-polarized Fermi surface mapping*, J. Electron Spectrosc. Relat. Phenom. **124**, 263-279 (2002).

[97] V. N. Petrov, V. V. Grebenshikov, B. D. Grachev and A. S. Kamochkin, *New compact classical 40 kV Mott polarimeter*, Rev. Sci. Instrum. **74**, 1278-1281 (2003).

[98] C. M. Cacho, S. Vlaic, M. Malvestuto, B. Ressel, E. A. Seddon and F. Parmigiani, *Absolute spin calibration of an electron spin polarimeter by spin-resolved photoemission from the Au(111) surface states*, Rev. Sci. Instrum. **80**, 043904 (2009).

[99] S. Souma, A. Takayama, K. Sugawara, T. Sato and T. Takahashi *Ultrahigh-resolution spin-resolved photoemission spectrometer with a mini Mott detector* Rev. Sci. Instrum. **81**, 095101 (2010).

[100] J. Kessler, *Polarized Electrons, 2nd ed*, (Springer, Berlin, 1985).

[101] R. Jungblut, C. Roth, F. U. Hillebrecht, and E. Kisker, *Spin-polarized electron spectroscopy as a combined chemical and magnetic probe*, Surf. Sci. **615**, 269270 (1992).

[102] R. Bertacco, M. Merano and F. Ciccacci, *Spin dependent electron absorption in Fe(001)-p(1×1)O: A new candidate for a stable and efficient electron polarization analyzer*, Appl. Phys. Lett. **72**, 2050-2052 (1998).

[103] T. Okuda, Y. Takeichi, Y. Maeda, A. Harasawa, I. Matsuda, T. Kinoshita and A. Kakizaki, *A new spin-polarized photoemission spectrometer with very high efficiency and energy resolution*, Rev. Sci. Instrum. **79**, 123117 (2008).

[104] A. Winkelmann, D. Hartung, H. Engelhard, C.-T. Chiang and J. Kirschner, *High efficiency electron spin polarization analyzer based on exchange scattering at FeW(001)*, Rev. Sci. Instrum. **79**, 083303 (2008).

[105] C. Jozwiak, J. Graf, G. Lebedev, N. Andresen, A. K. Schmid, A. V. Fedorov, F. El Gabaly, W. Wan, A. Lanzara and Z. Hussain *A high-efficiency spin-resolved photoemission spectrometer combining time-of-flight spectroscopy with exchange-scattering polarimetry*, Rev. Sci. Instrum. **81**, 053904 (2010).

[106] T. Okuda, K. Miyamoto, H. Miyahara, K. Kuroda, A. Kimura, H. Namatame and M. Taniguchi, *Efficient spin resolved spectroscopy observation machine at Hiroshima Synchrotron Radiation Center*, Rev. Sci. Instrum. **82**, 103302 (2011).

[107] T. Okuda, K. Miyamoto, A. Kimura, H. Namatame and M. Taniguchi, *A double VLEED spin detector for high-resolution three dimensional spin vectorial analysis of anisotropic Rashba spin splitting*, J. Electron Spectrosc. Relat. Phenomena **201**, 23-29 (2015).

[108] J. Kirschner *Polarized Electrons at Surface*, (Springer-Verlag, Berlin, 1985).

[109] D. Tillmann, R. Thiel and E. Kisker *Very-low-energy spin-polarized electron diffraction from Fe(001)*, Z. Phys. B **77**, 1-2 (1989).

[110] T. Kiss, F. Kanetaka, T. Yokoya, T. Shimojima, K. Kanai, S. Shin, Y. Onuki, T. Togashi, C. Zhang, C. T. Chen and S. Watanabe, *Photoemission Spectroscopic Evidence of Gap Anisotropy in an f-Electron Superconductor*, Phys. Rev. Lett. **94** 057001 (2005).

[111] J. D. Koralek, J. F. Douglas, N. C. Plumb, Z. Sun, A. V. Fedorov, M. M. Murnane, H. C. Kapteyn, S. T. Cundiff, Y. Aiura, K. Oka, H. Eisaki and D. S. Dessau, *Laser Based Angle-Resolved Photoemission, the Sudden Approximation, and Quasiparticle-Like Spectral Peaks in* $Bi_2Sr_2CaCu_2O_{8+\delta}$, Phys. Rev. Lett. **96**, 017005 (2006).

[112] G. Liu, G. Wang, Y. Zhu, H. Zhang, G. Zhang, X. Wang, Y. Zhou, W. Zhang, H. Liu, L. Zhao, J. Meng, X. Dong, C. Chen, Z. Xu and X. J. Zhou, *Development of a vacuum ultraviolet laser-based angle-resolved photoemission system with a superhigh energy resolution better than 1 meV*, Rev. Sci. Instrum. **79**, 023105 (2008).

[113] T. Kiss, T. Shimojima, K. Ishizaka, A. Chainani, T. Togashi, T. Kanai, X. Y. Wang, C. T. Chen, S. Watanabe and S. Shin, *A versatile system for ultrahigh resolution, low temperature, and polarization dependent Laser-angle-resolved photoemission spectroscopy*, Rev. Sci. Instrum. **79**, 023106 (2008).

[114] R. Jiang, D. Mou, Y. Wu, L. Huang, C. D. McMillen, J. Kolis, H. G. I. Giesber, J. J. Egan and A. Kaminski, *Tunable vacuum ultraviolet laser based spectrometer for angle resolved photoemission spectroscopy*, Rev. Sci. Instrum. **85**, 033902 (2014).

[115] K. Okazaki, Y. Ota, Y. Kotani, W. Malaeb, Y. Ishida, T. Shimojima, T. Kiss, S. Watanabe, C.-T. Chen, K. Kihou, C. H. Lee, A. Iyo, H. Eisaki, T. Saito, H. Fukazawa, Y. Kohori, K.

Hashimoto, T. Shibauchi, Y. Matsuda, H. Ikeda, H. Miyahara, R. Arita, A. Chainani and S. Shin, *Octet-Line Node Structure of Superconducting Order Parameter in KFe_2As_2*, Science **337**, 1314 (2012).

[116] T. Shimojima, K. Ishizaka, Y. Ishida, N. Katayama, K. Ohgushi, T. Kiss, M. Okawa, T. Togashi, X.-Y. Wang, C.-T. Chen, S. Watanabe, R. Kadota, T. Oguchi, A. Chainani and S. Shin, *Orbital-Dependent Modifications of Electronic Structure across the Magnetostructural Transition in $BaFe_2As_2$*, Phys. Rev. Lett. **104**, 057002 (2010).

[117] Y. Suzuki, T. Shimojima, T. Sonobe, A. Nakamura, M. Sakano, H. Tsuji, J. Omachi, K. Yoshioka, M. Kuwata-Gonokami, T. Watashige, R. Kobayashi, S. Kasahara, T. Shibauchi, Y. Matsuda, Y. Yamakawa, H. Kontani and K. Ishizaka, *Momentum-dependent sign inversion of orbital order in superconducting FeSe*, Phys. Rev. B **92**, 205117 (2015).

[118] C. T. Chen, Z. Y. Xu, D. Q. Deng, J. Zhang, G. K. L. Wong, B. C. Wu, N. Ye and D. Y. Tang, *The vacuum ultraviolet phase- matching characteristics of nonlinear optical $KBe_2BO_3F_2$ crystal*, Appl. Phys. Lett. **68**, 2930-2932 (1996).

[119] C. T. Chen, J. H. Lu, T. Togashi, T. Suganuma, T. Sekikawa, S. Watanabe, Z. Y. Xu and J. Y. Wang, *Second-harmonic generation from a $KBe_2BO_3F_2$ crystal in the deep ultraviolet*, Opt. Lett. **27**, 637-639 (2002).

[120] X. J. Zhou, B. Wannberg, W. L. Yanga, V. Broueta, Z. Sun, J. F. Douglas, D. Dessau, Z. Hussain and Z.-X. Shen, *Space charge effect and mirror charge effect in photoemission spectroscopy*, J. Electron Spectrosc. Relat. Phenom. **142**, 27-38 (2005).

[121] S. Hellmann, K. Rossnagel, M. Marczynski-Bühlow and L. Kipp, *Vacuum space-charge effects in solid-state photoemission*, Phys. Rev. B **79**, 035402 (2009).

[122] J. Omachi, K. Yoshioka and M. Kuwata-Gonokami, *High-power, narrow-band, high-repetition-rate, 5.9 eV coherent light source using passive optical cavity for laser-based angle-resolved photoelectron spectroscopy*, Optics Express **20**, 23542-23552 (2012).

[123] A. Fero, C. L. Smallwood, G. Affeldt and A. Lanzara, *Impact of Work Function Induced Electric Fields on Laser-based Angle-resolved Photoemission Spectroscopy* J. Electron Spectrosc. Relat. Phenom. **195**, 247-243 (2014)

[124] Y. Arashida, personal communication.

[125] A. E. Böhmer, F. Hardy, F. Eilers, D. Ernst, P. Adelmann, P. Schweiss, T. Wolf and C. Meingast, *Lack of coupling between superconductivity and orthorhombic distortion in stoichiometric single-crystalline FeSe* Phys. Rev. B **87**, 180505(R) (2013).

[126] T. Shimojima, Y. Suzuki, T. Sonobe, A. Nakamura, M. Sakano, J. Omachi, K. Yoshioka, M. Kuwata-Gonokami, K. Ono, H. Kumigashira, A. E. Böhmer, F. Hardy, T. Wolf, C. Meingast, H. v. Löhneysen, H. Ikeda and K. Ishizaka, *Lifting of xz/yz orbital degeneracy at the structural transition in detwinned FeSe*, Phys. Rev. B **90**, 121111(R) (2014).

[127] K. Nakayama, Y. Miyata, G. N. Phan, T. Sato, Y. Tanabe, T. Urata, K. Tanigaki and T. Takahashi *Reconstruction of Band Structure Induced by Electronic Nematicity in an FeSe Superconductor*, Phys. Rev. Lett. **113**, 237001 (2014).

[128] M. D. Watson, T. K. Kim, A. A. Haghighirad, N. R. Davies, A. McCollam, A. Narayanan, S. F. Blake, Y. L. Chen, S. Ghannadzadeh, A. J. Schoeld, M. Hoesch, C. Meingast, T. Wolf and A. I. Coldea, *Emergence of the nematic electronic state in FeSe*, Phys. Rev. B **91**, 155106 (2015).

[129] P. Zhang, T. Qian, P. Richard, X. P. Wang, H. Miao, B. Q. Lv, B. B. Fu, T. Wolf, C. Meingast, X. X. Wu, Z. Q. Wang, J. P. Hu and H. Ding, *Observation of two distinct d_{xz}/d_{yz} band splittings in FeSe*, Phys. Rev. B **91**, 214503 (2015).

[130] M. Uchida, K. Ishizaka, P. Hansmann, Y. Kaneko, Y. Ishida, X. Yang, R. Kumai, A. Toschi, Y. Onose, R. Arita, K. Held, O. K. Andersen, S. Shin and Y. Tokura, *Pseudogap of Metallic Layered Nickelate $R_2Sr_xNiO_4$ (R =Nd, Eu) Crystals Measured Using Angle-Resolved Photoemission Spectroscopy*, Phys. Rev. Lett. **106**, 027001 (2011).

[131] R. Suzuki, M. Sakano, Y. J. Zhang, R. Akashi, D. Morikawa, A. Harasawa, K. Yaji, K. Kuroda, K. Miyamoto, T. Okuda, K. Ishizaka, R. Arita and Y. Iwasa (equal contribution) *Valley-dependent spin polarization in bulk MoS_2 with broken inversion symmetry*, Nat. Nanotechnol **9**, 611-617 (2014).

[132] S. R. Park, C. H. Kim, J. Yu, J. H. Han and C. Kim, *Orbital-Angular-Momentum Based Origin of Rashba-Type Surface Band Splitting*, Phys. Rev. Lett. **107**, 156803 (2011).

[133] M. I. Dyakonov and V. I. Perel, *Spin relaxation of conduction electrons in noncentrosymetric semiconductors*, Sov. Phys. Sol. State **13**, 3023-3026 (1971).

[134] M. I. Dyakonov and V. I. Perel, *Optical orientation in a system of electrons and lattice nuclei in semiconductors Theory*, Sov. Phys. JETP **38**, 177-183 (1973).

[135] Y. Ohno, R. Terauchi, T. Adachi, F. Matsukura and H. Ohno, *Spin Relaxation in GaAs(110) Quantum Wells*, Phys. Rev. Let. **83**, 4196-4199 (1999).

[136] K. F. Mak, C. Lee, J. Hone, J. Shan and T. F. Heinz, *Atomically Thin MoS_2 : A New Direct-Gap Semiconductor*, Phys. Rev. Lett. 105, 136805 (2010).

[137] D. Xiao, M.-C. Chang, and Q. Niu. *Berry phase effects on electronic properties*, Rev. Mod. Phys. **82**, 1959-2007 (2010).

[138] Z. Y. Zhu, Y. C. Cheng and U. Schwingenschlögl, *Giant spin-orbit-induced spin splitting in two-dimensional transition-metal dichalcogenide semiconductors*, Phys. Rev. B **84**, 153402 (2011).

[139] D. Xiao, G.-B. Liu, W. Feng, X. Xu and W. Yao, *Coupled Spin and Valley Physics in Monolayers of MoS_2 and Other Group-VI Dichalcogenides*, Phys. Rev. Lett. **108**, 196802 (2012).

[140] G.-B. Liu, W.-Y. Shan, Y. Yao, W. Yao and D. Xiao, *Three-band tight-binding model for monolayers of group-VIB transition metal dichalcogenides*, Phys. Rev. B **88**, 085433 (2013).

[141] K. Takashina, Y. Ono, A. Fujiwara, Y. Takahashi and Y. Hirayama, *Valley polarization in Si(100) at zero magnetic field*, Phys. Rev. Lett. **96**, 236801 (2006).

[142] J. Isberg, M. Gabrysch, J. Hammersberg, S. Majdi, K. K. Kovi and D. J. Twitchen, *Generation, transport and detection of valley-polarized electrons in diamond*, Nature Mater. **12**, 760764 (2013).

[143] Y. P. Shkolnikov, E. P. De Poortere, E. Tutuc and M. Shayegan, *Valley splitting of AlAs two-dimensional electrons in a perpendicular magnetic field*, Phys. Rev. Lett. **89**, 226805 (2002).

[144] O. Gunawan, Y. P. Shkolnikov, K. Vakili, T. Gokmen, E. P. De Poortere and M. Shayegan, *Valley susceptibility of an interacting two-dimensional electron system*, Phys. Rev. Lett. **97**, 186404 (2006).

[145] O. Gunawan, T. Gokmen, K. Vakili, M. Padmanabhan, E. P. De Poortere and M. Shayegan, *Spin-valley phase diagram of the two-dimensional metalinsulator transition*, Nature Phys. **3**, 388391 (2007).

[146] Z. Zhu, A. Collaudin, B, Fauqué, W. Kang and K. Behnia, *Field-induced polarization of Dirac valleys in bismuth*, Nature Phys. **8**, 8994 (2012).

[147] D. Xiao, W. Yao and Q. Niu, *Valley-Contrasting Physics in Graphene*: *Magnetic Moment and Topological Transport*, Phys. Rev. Lett. **99**, 236809 (2007).

[148] A. Rycerz, J. Tworzydlo and C. W. J. Beenakker, *Valley filter and valley valve in graphene*, Nature Phys. **3**, 172175 (2007).

[149] W. Yao, D. Xiao and Q. Niu, *Valley-dependent optoelectronics from inversion symmetry breaking*, Phys. Rev. B **77**, 235406 (2008).

[150] D. Gunlycke and C. T. White, *Graphene valley lter using a line defect*, Phys. Rev. Lett. **106**, 136806 (2011).

[151] H. Zeng, J. Dai, W. Yao, Di Xiao and X. Cui, *Valley polarization in MoS2 monolayers by optical pumping*, Nat. Nanotechnol, **7** 490493 (2012).

[152] T. Cao, G. Wang, W. Han, H. Ye, C. Zhu, J. Shi, Q. Niu, P. Tan, E. Wang B. Liu and J. Feng, *Valley-selective circular dichroism of monolayer molybdenum disulphide*, Nat. Commun. **7**, 490- (2012).

[153] K. F. Mak, K. He, J. Shan, and T. F. Heinz, *Control of valley polarization in monolayer MoS_2 by optical helicity*, Nat. Nanotechnol **7**, 494498 (2012).

[154] K. F. Mak, K. L. McGill, J. Park and P. L. McEuen, *The valley Hall effect in MoS_2 transistors*, Science **344**, 1489-1492 (2014).

[155] W. Jin, P.-C. Yeh, N. Zaki, D. Zhang, J. T. Sadowski, A. Al-Mahboob, A. M. van der Zande, D. A. Chenet, J. I. Dadap, I. P. Herman, P. Sutter, J. Hone and R. M. Osgood, Jr., *Direct Measurement of the Thickness-Dependent Electronic Band Structure of MoS_2 Using Angle-Resolved Photoemission Spectroscopy*, Phys. Rev. Lett. **111**, 106801 (2013).

[156] Y. Zhang, T.-R. Chang, B. Zhou, Y.-T. Cui, H. Yan, Z. Liu, F. Schmitt, J. Lee, R. Moore, Y. L. Chen, H. Lin, H.-T. Jeng, S.-K. Mo, Z. Hussain, A. Bansil and Z.-X. Shen, *Direct observation of the transition from indirect to direct bandgap in atomically thin epitaxial $MoSe_2$*, Nat. Nanotechnol. **9**, 111-115 (2014).

[157] K. Sugawara, T. Sato, Y. Tanaka, S. Souma and T. Takahashi, *Spin- and valley-coupled electronic states in monolayer WSe_2 on bilayer graphene*, Appl. Phys. Lett. **107**, 071601 (2015).

[158] K. S. Novoselov, A. K. Geim, S. V. Morozov, D. Jiang, Y. Zhang, S. V. Dubonos, I. V. Grigorieva and A. A. Firsov, *Electric Field Effect in Atomically Thin Carbon Films*, Science **306**, 666-669 (2004).

[159] X. Zhang, Q. Liu, J.-W. Luo A. J. Freeman and A. Zunger, *Hidden spin polarization in inversion-symmetric bulk crystals*, Nat. Phys. **10**, 387393 (2014).

[160] J. M. Riley, F. Mazzola, M. Dendzik, M. Michiardi, T. Takayama, L. Bawden, C. Granerd, M. Leandersson, T. Balasubramanian, M. Hoesch, T. K. Kim, H. Takagi, W. Meevasana, Ph. Hofmann, M. S. Bahramy, J. W. Wells and P. D. C. King, *Direct observation of spin-polarized bulk bands in an inversion-symmetric semiconductor*, Nat. Phys. **10**, 835839 (2014).

[161] J. A. Wilson and A. D. Yoffe, *The transition metal dichalcogenides discussionand interpretation of the observed optical, electrical and structural properties*, Adv. Phys. **18**, 193334 (1969).

[162] J. C. Wildervanck, *Chalcogenides of Molybdenum, Tungsten, Technetium and Rhenium*, PhD thesis, Univ. of Groningen (1970).

[163] L. C. Towle, V. Oberbeck, B. E. Brown and R. E. Stajdohar, *Molybdenum diselenide: rhombohedral high pressure-high temperature polymorph*, Science **154**, 895896 (1966).

[164] 鈴木龍二, 「二次元原子膜における結晶多形を用いたスピン/バレー分極制御」, 東京大学大学院工学系研究科　物理工学専攻　修士論文, (2014).

[165] P. Blaha, K. Schwarz, P. Sorantin and S. Trickey, *B. Full-potential, linearized augmented plane wave programs for crystalline systems*, Comp. Phys. Commun. **59**, 399415 (1990).

[166] J. P. Perdew, K. Burke and M. Ernzerhof, *Generalized gradient approximation made simple*, Phys. Rev. Lett. **77**, 38653868 (1996).

[167] K. D. Bronsema, J. L. de Boer and F. Jellinek, *On the structure of molybdenum diselenide and disulfide*, Z. anorg. allg. Chem. **540**, 15-17 (1986).

[168] A. A. Golubichanaya, A. G. Duksina and V. L. Kalikhman, *Variation of the antifriction and electrical properties of a number of solid lubricants with the oxidation temperature*, Inorg. Mater. **15**, 1156-1158 (1979).

[169] R. Coehoorn, C. Haas and R. A. de Groot *Electronic structure of $MoSe_2$, MoS_2, and WSe2. II. The nature of the optical band gaps* Phys. Rev. B **35**, 6203-6206 (1987).

[170] R. Akashi, M. Ochi, S. Bordács, R. Suzuki, Y. Tokura, Y. Iwasa and R. Arita, *Two-Dimensional Valley Electrons and Excitons in Noncentrosymmetric 3R-MoS_2*, Phys. Rev. Appl. **4**, 014002 (2015).

[171] J. M. Riley, W. Meevasana, L. Bawden, M. Asakawa,T. Takayama, T. Eknapakul, T. K. Kim, M. Hoesch, S.-K. Mo, H. Takagi, T. Sasagawa, M. S. Bahramy and P. D. C. King, *Negative electronic compressibility and tunable spin splitting in WSe_2* Nat. Nanotechnol. **10**, 10431047 (2015).

[172] H. T. Yuan, M. S. Bahramy, K. Morimoto, S. F. Wu, K. Nomura, B. J. Yang, H. Shimotani, R. Suzuki, M. Toh, C. Kloc, X. D. Xu, R. Arita, N. Nagaosa and Y. Iwasa, *Zeeman-type spin splitting controlled by an electric field*, Nature Physics, **9**, 563-569 (2013).

[173] K. Sakamoto, T.-H. Kim, T. Kuzumaki, B. Mller, Y. Yamamoto, M. Ohtaka, J. R. Osiecki, K. Miyamoto, Y. Takeichi, A. Harasawa, S. D. Stolwijk, A. B. Schmidt, J. Fujii, R. I. G. Uhrberg, M. Donath, H. W. Yeom and T. Oda, *Valley spin polarization by using the extraordinary Rashba effect on silicon*, Nat. Commun. **4**, 2073 (2013).

[174] K. Wittel and R. Manne, *Atomic spinorbit interaction parameters from spectral data for 19 elements*, Theor. Chim. Acta **33**, 347349 (1974).

[175] N. N. Zhuravlev, *STRUCTURE OF SUPERCONDUCTORS. 10. THERMAL, MICROSCOPIC AND X-RAY INVESTIGATION OF THE BISMUTH-PALLADIUM SYSTEM*, Sov. Phys. JETP-USSR **5**, 1064-1072 (1957).

[176] Y. Imai, F. Nabeshima, T. Yoshinaka, K. Miyatani, R. Kondo, S. Komiya, I. Tsukada and A. Maeda, *Superconductivity at 5.4 K in β-Bi_2Pd* J. Phys. Soc. Jpn. **81**, 113708 (2012).

[177] H. J. Monkhorst and J. D. Pack, *Special points for Brillouin-zone integrations*, Phys. Rev. B **13**, 51885192 (1976).

[178] L. Fu, *Hexagonal Warping Effects in the Surface States of the Topological Insulator Bi_2Te_3*, Phys. Rev. Lett. **103**, 266801 (2009).

[179] L. Fu and C. L. Kane, *Topological insulators with inversion symmetry*, Phys. Rev. B **76**, 045302 (2007).

[180] R. Hoffmann, *How Chemistry and Physics Meet in the Solid State*, Angew. Chem. Int. Ed. Engl. **26**, 846-878 (1987).

[181] W. A. Harrison, *Electronic Structure and the Properties of Solids: The Physics of the Chemical Bond*, (Dover Books on Physics 1989).

[182] F. Wilczek, *Majorana returns*, Nat. Phys. **5**, 614618 (2009).

[183] J. Alicea, *New directions in the pursuit of Majorana fermions in solid state systems*, Rep. Prog. Phys. **75**, 075602 (2012).

[184] C. W. J. Beenakker, *Search for Majorana fermions in superconductors*, Annu. Rev. Condens. Matter Phys. **4**, 113116 (2013).

[185] L. Fu and C. L. Kane, *Superconducting proximity effect and majorana fermions at the surface of a topological insulator*, Phys. Rev. Lett. **100**, 096407 (2008).

[186] H. Weyl, *Elektron und Gravitation*, I. Z. Phys. **56**, 330352 (1929).

[187] M. V. Berry, *Quantal Phase Factors Accompanying Adiabatic Changes*, Proc. R. Soc. London, Ser. **A392**, 45-57. (1984).

[188] H. B. Nielsen and M. Ninomiya, *The Adler-Bell-Jackiw anomaly and Weyl fermions in a crystal*, Physics Letters B **130**, 389-396 (1983).

[189] G. E. Volovik, *Chiral anomaly and the law of conservation of momentum in 3He-A*, ETP Lett. **43**, 428-431 (1986).

[190] J. Xiong, S. K. Kushwaha, T. Liang, J. W. Krizan, W. Wang, R. Cava and N. Ong, *Signature of the chiral anomaly in a Dirac semimetal: a current plume steered by a magnetic field*, arXiv:1503.08179 (2015).

[191] C. Zhang, S.-Y. Xu, I. Belopolski, Z. Yuan, Z. Lin, B. Tong, N. Alidoust, C.-C. Lee, S.-M. Huang, H. Lin, M. Neupane, D. S. Sanchez, H. Zheng, G. Bian, J. Wang, C. Zhang, T. Neupert, M. Z. Hasan and S. Jia, *Observation of the Adler-Bell-Jackiw chiral anomaly in a Weyl semimetal*, arXiv:1503.02630 (2015).

[192] X. Huang, L. Zhao, Y. Long, P. Wang, D. Chen, Z. Yang, H. Liang, M. Xue, H. Weng, Z. Fang, X. Dai and G. Chen, *Observation of the Chiral-Anomaly-Induced Negative Magnetoresistance in 3D Weyl Semimetal TaAs*, Phys. Rev. X **5**, 031023 (2015).

[193] M. S. Bahramy, B.-J. Yang, R. Arita and N. Nagaosa, *Emergence of non-centrosymmetric topological insulating phase in BiTeI under pressure*, Nat. Commun **3**, 679 (2012).

[194] J. Liu and D. Vanderbilt, *Weyl semimetals from noncentrosymmetric topological insulators*, Phys. Rev. B **90**, 155316 (2014).

[195] R. Okugawa and S. Murakami, *Dispersion of Fermi arcs in Weyl semimetals and their evolutions to Dirac cones*, Phys. Rev. B **89**, 235315 (2014).

[196] A. A. Soluyanov, D. Gresch, Z. Wang, Q.-S. Wu, M. Troyer, X. Dai and B. A. Bernevig, *Type-II Weyl semimetals*, Nature **527**, 495498 (2015).

[197] M. N. Ali, J. Xiong, S. Flynn, J. Tao, Q. D. Gibson, L. M. Schoop, T. Liang, N. Haldolaarachchige, M. Hirschberger, N. P. Ong and R. J. Cava, *Large, non-saturating magnetoresistance in WTe_2*, Nature **514**, 205208 (2014).

[198] I. Pletikosić Mazhar N. Ali, A. V. Fedorov, R. J. Cava and T. Valla, *Electronic Structure Basis for the Extraordinary Magnetoresistance in WTe_2*, Phys. Rev. Lett. **113**, 216601 (2014).

[199] Y. Wu, N. H. Jo, M. Ochi, L. Huang, D. Mou, S. L. Bud'ko, P. C. Canfield, N. Trivedi, R. Arita and A. Kaminski, *Temperature-Induced Lifshitz Transition in WTe_2*, Phys. Rev. Lett **115**, 166602 (2015).

[200] Y. Sun, S. -C. Wu, M. N. Ali, C. Felser and B. Yan, *Prediction of Weyl semimetal in orthorhombic $MoTe_2$*, Phys. Rev. B **92**, 161107(R) (2015).

[201] Z. Wang, D. Gresch, A. A. Soluyanov, W. Xie, S. Kushwaha, X. Dai, M. Troyer, R. J. Cava and B. A. Bernevig, *MoTe2: Weyl and Line Node Topological Metal*, arXiv:1511.07440 (2015).

[202] T. -R. Chang, S.-Y. Xu, G. Chang, C.-C. Lee, S.-M. Huang, B. Wang, G. Bian, H. Zheng, D. S. Sanchez, I. Belopolski, N. Alidoust, M. Neupane, A. Bansil. H. -T. Jeng, H. Lin and M. Z. Hasan, *Arc-tunable Weyl Fermion metallic state in $Mo_x W_{1-x} Te_2$*, arXiv:1508.06723 (2015).

[203] I. Belopolski*, S.-Y. Xu*, Y. Ishida*, X. Pan*, P. Yu, D. S. Sanchez, M. Neupane, N. Alidoust, G. Chang, T.-R. Chang, Y. Wu, G. Bian, H. Zheng, S.-M. Huang, C.-C. Lee, D. Mou, L. Huang, Y. Song, B. Wang, G. Wang, Y.-W. Yeh, N. Yao, J. Rault, P. Lefevre, F. Bertran, H.-T, Jeng, T. Kondo, A. Kaminski, H. Lin, Z. Liu, F. Song, S. Shin and M. Z. Hasan, (*equally contributed) *Unoccupied electronic structure and signatures of topological Fermi arcs in the Weyl semimetal candidate $Mo_x W_{1-x} Te_2$*, arXiv:1512.09099 (2015).

[204] G. Kresse *et al.*, Vienna Ab initio Software Packages (VASP) version 5.3.3, http://cms.mpi.univie.ac.at/vasp/ (2012).

[205] A. A. Mostofi, J. R. Yates, Y. -S. Lee, D. Vanderbilt and N. Marzari, *Wannier90: a tool for obtaining maximally localized Wannier functions*, Comput. Phys. Commun. **178**, 685-699 (2008).

[206] B. E. Brown, *The crystal structures of WTe 2 and high-temperature $MoTe_2$*, Acta Crystallogr. **20**, 268 (1966).

[207] R. Clarke, E. Marseglia and H. P. Hughes, *A low-temperature structural phase transition in β-$MoTe_2$*, Philos. Mag. B **38**, 121-126 (1978).

[208] H. P. Hughes and R. H. Friend, *Electrical resistivity anomaly in β-$MoTe_2$ (metallic behavior)*, J. Phys. C: Solid State Phys. **11**, L103 (1978).

[209] Y. Qi, P. G. Naumov, M. N. Ali, C. R. Rajamathi, Y. Sun, C. Shekhar, S.-C. Wu, V. S$\ddot{u}\beta$, M. Schmidt, E. Pippel, P. Werner, R. Hillebrand, T. Forster, E. Kampertt, W. Schnelle, S. Parkin, R. J. Cava, C. Felser, B. Yan and S. A. Medvedev, *Superconductivity in the Weyl semimetal candidate $MoTe_2$*, arXiv:1508.03502 (2015).

[210] 辻　英憲 「角度分解光電子分光法を用いた層状半金属 β-$Mo_{1-x}Nb_xTe_2$」, 東京大学大学院工学系研究科　物理工学専攻　修士論文, (2015).

[211] S.-M. Huang, S.-Y. Xu, I. Belopolski, C.-C. Lee, G. Chang, B. Wang, N. Alidoust, G. Bian, M. Neupane, A. Bansil, H. Lin and M. Z. Hasan, *A Weyl Fermion semimetal with surface Fermi arcs in the transition metal monopnictide TaAs class*, Nat. Commun. **6**, 7373 (2015).

[212] E. Bauer and M. Sigrist (Eds.), *Non-Centrosymmetric Superconductors*, (Springer, 2012).

[213] J. A. Sobota, S.-L. Yang, A. F. Kemper, J. J. Lee, F. T. Schmitt, W. Li, R. G. Moore, J. G. Analytis, I. R. Fisher, P. S. Kirchmann, T. P. Devereaux, and Z.-X. Shen, *Direct Optical Coupling to an Unoccupied Dirac Surface State in the Topological Insulator Bi_2Se_3*, Phys. Rev. Lett. **111**, 136802 (2013).

[214] S. V. Eremeev, I. V. Silkin, T. V. Menshchikova, A. P. Protogenov and E. V. Chulkov, *New topological surface state in layered topological insulators*: *Unoccupied dirac cone*, JETP Lett. **96**, 780-784 (2013).

Publication list

1. Y. Suzuki, T. Shimojima, T. Sonobe, A. Nakamura, **M. Sakano**, H. Tsuji, J. Omachi, K. Yoshioka, M. Kuwata-Gonokami, T. Watashige, R. Kobayashi, S. Kasahara, T. Shibauchi, Y. Matsuda, Y. Yamakawa, H. Kontani and K. Ishizaka, *Momentum-dependent sign-inversion of orbital order in superconducting FeSe*, Phys. Rev. B **92**, 205117 (2015).

2. **M. Sakano**, K. Okawa, M. Kanou, H. Sanjo, T. Okuda, T. Sasagawa and K. Ishizaka, *Topologically protected surface states in a centrosymmetric superconductor β-$PdBi_2$*, Nat. Commun. **6**, 8595 (2015).

3. T. Shimojima, Y. Suzuki, T. Sonobe, A. Nakamura, **M. Sakano**, J. Omachi, K. Yoshioka, M. Kuwata-Gonokami, K. Ono, H. Kumigashira, A. E. Bhmer, F. Hardy, T. Wolf, C. Meingast, H. v. Lhneysen, H. Ikeda and K. Ishizaka, *Lifting of xz/yz orbital degeneracy at the structural transition in detwinned FeSe*, Phys. Rev. B **90**, 12111(R) (2014).

4. R. Suzuki*, **M. Sakano***, Y. J. Zhang, R. Akashi, D. Morikawa, A. Harasawa, K. Yaji, K. Kuroda, K. Miyamoto, T. Okuda, K. Ishizaka, R. Arita and Y. Iwasa (***equally contributed**), *Valley-dependent spin polarization in bulk MoS_2 with broken inversion symmetry*, Nat. Nanotechnol. **9**, 611-617 (2014).

5. **M. Sakano**, M. S. Bahramy, A. Katayama, T. Shimojima, H. Murakawa, Y. Kaneko, W. Malaeb, S. Shin, K. Ono, H. Kumigashira, R. Arita, N. Nagaosa, H. Y. Hwang, Y. Tokura and K. Ishizaka, *Strongly Spin-Orbit Coupled Two-Dimensional Electron Gas Emerging near the Surface of Polar Semiconductors*, Phys. Rev. Lett. **110**, 107204 (2013).

6. **M. Sakano**, J. Miyawaki, A. Chainani, Y. Takata, T. Sonobe, T. Shimojima, M. Oura, S. Shin, M. S. Bahramy, R. Arita, N. Nagaosa, H. Murakawa, Y. Kaneko, Y. Tokura and K. Ishizaka, *Three-dimensional bulk band dispersion in polar BiTeI with giant Rashba-type spin splitting*, Phys. Rev. B **86**, 085204 (2012).

7. M. Uchida, K. Ishizaka, P. Hansmann, X. Yang, **M. Sakano**, J. Miyawaki, R. Arita, Y. Kaneko, Y. Takata, M. Oura, A. Toschi, K. Held, A. Chainani, O. K. Andersen, S. Shin and Y. Tokura, *Orbital characters of three-dimensional Fermi surfaces in* $Eu_{2-x}Sr_xNiO_4$ *as probed by soft-x-ray angle-resolved photoemission spectroscopy*, Phys. Rev. B **84**, 241109(R) (2011).

8. K. Ishizaka, M. S. Bahramy, H. Murakawa, **M. Sakano**, T. Shimojima, T. Sonobe, K. Koizumi, S. Shin, H. Miyahara, A. Kimura, K. Miyamoto, T. Okuda, H. Namatame, M. Taniguchi, R. Arita, N. Nagaosa, K. Kobayashi, Y. Murakami, R. Kumai, Y. Kaneko, Y. Onose and Y. Tokura, *Giant Rashba-type spin splitting in bulk BiTeI*, Nat. Mater. **10**, 521-526 (2011).

Acknowledgement

First of all, I would like to express my deepest gratitude to Prof. Kyoko Ishizaka for her patient supervision, insightful suggestions and continual encouragement. I consider myself very lucky to have joined her group and spent precious time as her first student.

I acknowledge the valuable comments of Prof. Katsuyuki Fukutani, Prof. Taka-hisa Arima, Prof. Ryotaro Arita, Prof. Shintaro Ishiwata and Prof. Takeshi Kondo. I am grateful to the following research collaborators for this thesis:

Chapter 3: Dr. Junko Ohmachi, Dr. Daisuke Hirano, Dr. Takahiro Shimojima, Dr. Kosuke Yoshioka and Prof. Makoto Kuwata-Gonokami

Chapter 4: Mr. Ryuji Suzuki, Mr. Yijin Zhang, Dr. Ryosuke Akashi, Dr. Daisuke Morikawa, Dr. Koichiro Yaji, Dr. Ayumi Harasawa, Dr. Kenta Kuroda, Dr. Koji Miyamoto, Prof. Taichi Okuda, Prof. Ryotaro Arita and Prof. Yoshihiro Iwasa

Chapter 5: Mr. Kenjiro Okawa, Dr. Manabu Kano, Mr. Haruhiko Sanjo, Prof. Taichi Okuda and Prof. Takao Sasagawa

Chapter 6: Dr. Mohammad Saeed Bahramy, Mr. Koji Ikeura, Prof. Hideaki Sakai, Mr. Hidenori Tsuji, Mr. Itsuki Araya, Dr. Kenta Kuroda, Dr. Koichiro Yaji, Dr. Ayumi Harasawa, Prof. Shik Shin and Prof. Shintaro Ishiwata

I owe special thanks to Prof. Katsumi Midorikawa, Prof. Alessandra Lanzara and Lanzara group members in the Advenced Leading Graduate Course for Photon Science (ALPS). I am also grateful to Ishizaka Laboratory members. In particular, I have shared a great deal of time with Mr. Tatsuya Sonobe from the fourth year of the Bachelor's degree. His kind, patient and sincere attitude has always encouraged me. Finally, I would like to thank my parents and sisters for kind encouragements.